

NORTHWESTERN UNIVERSITY

Nanoscale Investigation of Platinum Nanoparticles on SrTiO<sub>3</sub> Grown via Physical Vapor  
Deposition and Atomic Layer Deposition

A DISSERTATION

SUBMITTED TO THE GRADUATE SCHOOL  
IN PARTIAL FULFILMENT OF THE REQUIREMENTS

for the degree

DOCTOR OF PHILOSOPHY

Field of Materials Science and Engineering

By

Steven Thomas Christensen

EVANSTON, ILLINOIS

December 2008

© Copyright by Steven Thomas Christensen 2008  
All Rights Reserved

## ABSTRACT

### Nanoscale Investigation of Platinum Nanoparticles on SrTiO<sub>3</sub> Grown via Physical Vapor Deposition and Atomic Layer Deposition

Steven Thomas Christensen

This dissertation examines growth of platinum nanoparticles from vapor deposition on SrTiO<sub>3</sub> using a characterization approach that combines imaging techniques and X-ray methods. The primary suite of characterization probes includes atomic force microscopy (AFM), grazing-incidence small-angle X-ray scattering (GISAXS), X-ray fluorescence (XRF), scanning electron microscopy (SEM), and X-ray absorption spectroscopy (XAS). The vapor deposition techniques include physical vapor deposition (PVD) by evaporation and atomic layer deposition (ALD). For the PVD platinum study, AFM/XRF showed ~10 nm nanoparticles separated by an average of 100 nm. The combination of AFM, GISAXS, and XRF indicated that the nanoparticles observed with AFM were actually comprised of closely spaced, smaller nanoparticles. These conclusions were supported by high-resolution SEM. The unusual behavior of platinum nanoparticles to aggregate without coalescence or sintering was observed previously by other researchers using transmission electron microscopy (TEM). Platinum nanoparticle growth was also investigated on SrTiO<sub>3</sub> (001) single crystals using ALD to nucleate nanoparticles that subsequently grew and coalesced into granular films as the ALD progresses. The expected growth rate for the early stages of ALD showed a two-fold increase which was attributed to the platinum deposition occurring faster on the bare substrate. Once the nanoparticles had coalesced into a film, steady state ALD growth proceeded. The formation of nanoparticles was attributed to the atomic diffusion of platinum atoms on the surface in addition

to direct growth from the ALD precursor gases. The platinum ALD nanoparticles were also studied on SrTiO<sub>3</sub> nanocube powders. The SrTiO<sub>3</sub> nanocubes average 60 nm on a side and the cube faces have a {001} orientation. The ALD proceeded in a similar fashion as on the single crystal substrates where the deposition rate was twice as fast as the steady state growth rate. The Pt nanoparticle size increased linearly starting at ~0.7 nm for 1 ALD cycle to ~3 nm for 5 ALD cycles. The platinum chemical state was also investigated using X-ray absorption spectroscopy. Platinum nanoparticles ~1 nm or smaller tended to be oxidized. For larger nanoparticles, the platinum state systematically approached that of bulk platinum metal as the size (number of ALD cycles) increased. The platinum loading was exceptionally low,  $\sim 10^{-3}$  mg cm<sup>-2</sup>.

Approved:

---

Professor Mark C. Hersam  
Department of Materials Science and Engineering  
Northwestern University  
Evanston, Illinois

---

Professor Michael J. Bedzyk  
Department of Materials Science and Engineering  
Northwestern University  
Evanston, Illinois

## ACKNOWLEDGEMENT

The counsel to “do something difficult for my posterity” was once given to me. This work would not have been possible without the help from many collaborators, friends, and loved ones. I will begin with honoring my wife, Carrie, for her help and support. Without her, I could not have achieved any of my academic goals and she makes it possible to continue to the next opportunity.

My advisors deserve many thanks for their support of this effort. First, I would like to thank Mark Hersam as my advisor and motivator. He sets a remarkable example and through his expectations I have been able to improve many aspects of my approach to research. I would like to thank Mike Bedzyk for sharing his exceptional talents as an experimentalist and critical thinker. Through working with both individuals, I feel prepared to take the next step into a research-oriented career.

I thank Peter Voorhees and Peter Stair for serving on my doctoral committee and for their helpful discussions. Additional faculty members that have offered helpful advice include Ken Poepelmeier and Laurence Marks.

As principal collaborators, I want to recognize Jeff Elam and Byeongdu Lee. They have provided many opportunities for me to conduct research and improve my work. Federico Rabuffetti also deserves recognition for the work on the STO nanocube project. I would also like to thank Brian Quesada for working on UHV and STO related problems. I am grateful to Ann Chiaramonti, Courtney Lainier, and Jared Smit for providing direction early in my time here. I am grateful to Gordana Ostojic for preparing nanotube solutions for beam line work.

As friends and advice givers, I would like to start off with thanking Dave Comstock who has provided many useful conversations on how to get things working. I want to thank Jeff Klug for his mind of physics, knowledge of other things, and love for Johnny Cash. I will thank Jon Emery for his cheerful demeanor and tireless devotion to the beautiful game. My UHV knowledge stems from Eddie Foley and Nathan Guisinger. I also will be laughing for many years to come by remembering Eddie wearing Nathan G.'s memorabilia baseball helmet in our intramural basketball game. My Matlab skills originate from Mark Greene and Nathan Yoder. I would like to thank Liam Pingree for his example, Mike Arnold for his style, Reagan Kinser for his kindness, Zhenxing Feng for his eagerness, Rajiv Basu for his culinary descriptiveness, Justice Alaboson for his positive attitude, Phillip Lin for his Dreamy Pillow folders and accessories, Josh Kellar for help with XPS, and Qing-Wa Wang for swapping so many group meetings. I also appreciate the association with Anthony Escudro, Duane Goodner, Norma Cortes, Mike Walsh, Vaibhav Kohli, Yuan-Chieh Tseng and all of the Hersam and Bedzyk group members. I would like to thank the Mat Sci intramural basketball team that left me unguarded to sink the playoff buzzer beater. Jerry Carsello is appreciated for conversation, fixing X-ray machines and lending tools. I also acknowledge the support and help from friends like James Van De Graaff, Jason Pugh, Ben Severson, David Dubbeldam, Isaac Lund, Sam Carpenter, Tony Hayek, and Duane Hilton. Beam line staff such as Denis Keane, Steve Weigand, Qing Ma, Soenke Seifert, and Zhan Zhang deserve many thanks. Lastly, I would like to thank my parents and in-laws: Tom and Lorraine Christensen; Paul and Alene Peterson.

## TABLE OF CONTENTS

Abstract .....	3
Acknowledgement .....	5
List of Figures.....	10
List of Tables.....	13
<b>1. Introduction</b>	
1.1 Thesis statement .....	14
1.2 Platinum nanoparticles.....	16
<b>2. Structure, properties, and preparation of Pt, SrTiO<sub>3</sub> and Pt/SrTiO<sub>3</sub></b>	
<b>2.1 Strontium titanate</b>	
2.1.1 SrTiO <sub>3</sub> in the bulk.....	18
2.1.2 SrTiO <sub>3</sub> (001) surface structures and their preparation.....	23
2.1.3 SrTiO <sub>3</sub> (001) surface morphology.....	26
2.1.4 Role of chemical termination in the SrTiO <sub>3</sub> (001) surface.....	28
2.2 Platinum structure and properties.....	29
<b>2.3 Pt / SrTiO<sub>3</sub> (001)</b>	
2.3.1 Pt/SrTiO <sub>3</sub> (001) structure and morphology .....	30
2.3.2 Catalytic properties of the Pt/SrTiO <sub>3</sub> system.....	33
2.4 Selection of the SrTiO <sub>3</sub> (001) surface preparation method.....	36
<b>3. Experimental characterization methods</b>	
3.1 Atomic force microscopy combined with X-ray techniques .....	31
3.2 AFM methods.....	31

3.3 X-ray Techniques	
3.3.1 Small-angle X-ray scattering.....	39
3.3.2 Grazing incidence small-angle X-ray scattering.....	47
3.3.3 X-ray fluorescence measurements .....	52
3.3.4 X-ray absorption spectroscopy .....	53
4. PVD platinum nanoparticle aggregation on SrTiO <sub>3</sub> (001)	
4.1 Platinum nanoparticles on SrTiO <sub>3</sub> (001) via physical vapor deposition.....	58
4.2 Platinum deposition and post-deposition annealing .....	59
4.3 Measurement of PVD platinum on SrTiO <sub>3</sub> (001).....	59
4.4 Platinum nanoparticle aggregation on SrTiO <sub>3</sub> .....	70
4.5 Conclusions for PVD Pt nanoparticles .....	77
5. Nanoscale structure and morphology of atomic layer deposition platinum on SrTiO <sub>3</sub> (001)	
5.1 Atomic layer deposition.....	79
5.2 Platinum atomic layer deposition.....	81
5.3 Measurements of Pt ALD on SrTiO <sub>3</sub> (001) .....	82
5.4 Model of Pt nanoparticle nucleation and growth via ALD.....	93
5.5 Summary of Pt ALD.....	96
6. Structure and morphology of platinum nanoparticles deposited via atomic layer deposition on strontium titanate nanocubes	
6.1 ALD platinum growth on SrTiO <sub>3</sub> nanocubes.....	98



6.2 Synthesis ALD Pt / SrTiO <sub>3</sub> nanocubes	
6.2.1 SrTiO <sub>3</sub> nanocube growth.....	98
6.2.2 Pt ALD on nanocubes.....	99
6.3 X-ray measurements of ALD Pt / SrTiO <sub>3</sub> nanocubes.....	99
6.4 Characterization results	
6.4.1 Mass and Microscopy.....	101
6.4.2 X-ray Scattering.....	103
6.4.3 X-ray absorption spectroscopy .....	106
6.5 Discussion of the Pt/nanocube results .....	114
6.6 Summary of ALD Pt / SrTiO <sub>3</sub> nanocubes.....	116
7. Concluding remarks	
7.1 Conclusion .....	118
7.2 Outlook .....	120
8. References .....	124
9. Appendix A: Surface structures of SrTiO <sub>3</sub> (001) prepared during this project.....	138
10. Appendix B: X-ray standing wave atomic density maps.....	145
11. Appendix C: X-ray reflectivity measurements of Pt/SrTiO <sub>3</sub> (001) .....	147
12. Appendix D: Plans of the X-ray reaction cell base.....	151
13. Appendix E: Experimental Facilities .....	154
14. Vita.....	156

## LIST OF FIGURES

Figure 2.1 SrTiO <sub>3</sub> and Pt crystal structures .....	19
Figure 2.2 High-resolution scan of the (002) SrTiO <sub>3</sub> Bragg reflection.....	22
Figure 2.3 AFM and LEED images of SrTiO <sub>3</sub> (001) sample preparation.....	25
Figure 2.4 AFM images of $\alpha$ -Fe <sub>2</sub> O <sub>3</sub> (001) before and after annealing .....	27
Figure 2.5 Atomic density maps for Pt/SrTiO <sub>3</sub> from XSW data .....	32
Figure 3.1 Simulated SAXS data for different size spheres .....	41
Figure 3.2 Simulated SAXS data for spheres with different size distributions .....	42
Figure 3.3 Guinier plot for simulated SAXS data of a sphere.....	44
Figure 3.4 Effect of interparticle interactions for simulated SAXS data .....	46
Figure 3.5 Schematic for the distorted wave Born approximation .....	48
Figure 3.6 Schematic for a GISAXS experiment.....	50
Figure 3.7 Simulated paracrystal interference function .....	51
Figure 3.8 Normalized X-ray absorption spectroscopy data for Pt compounds.....	55
Figure 3.9 Fourier transform of the X-ray absorption spectroscopy data of Pt.....	57
Figure 4.1 AFM images following PVD Pt deposition.....	60
Figure 4.2 XSW data for Pt / SrTiO <sub>3</sub> (001).....	64
Figure 4.3 GISAXS data of a blank SrTiO <sub>3</sub> substrate.....	66
Figure 4.4 GISAXS data after PVD Pt deposition.....	66
Figure 4.5 Guinier plot of the $q_{xy}$ data for PVD Pt / SrTiO <sub>3</sub> .....	68
Figure 4.6 Line cuts through the Figure 4.4 GISAXS data.....	69
Figure 4.7 Diagram of the nanoparticle spacing.....	72

Figure 4.8	TEM image of a platinum nanoparticle aggregate from Ref. [10].....	72
Figure 4.9	High-resolution SEM images of Pt nanoparticle aggregates.....	76
Figure 5.1	AFM images following Pt ALD.....	83
Figure 5.2	SEM images following Pt ALD.....	84
Figure 5.3	GISAXS data for a blank SrTiO <sub>3</sub> (001) substrate.....	85
Figure 5.4	GISAXS data after Pt ALD.....	85
Figure 5.5	GISAXS line cut data from Figure 5.4.....	87
Figure 5.6	XRF Pt coverage vs. ALD cycle.....	90
Figure 5.7	XPS spectra of the Pt 4f lines for 40 ALD cycles.....	91
Figure 5.8	Comparison of GISAXS data between PVD and ALD Pt.....	92
Figure 6.1	Platinum loading by mass gain.....	102
Figure 6.2	SEM images of SrTiO <sub>3</sub> nanocubes and after Pt ALD.....	102
Figure 6.3	SAXS data of ALD Pt /nanocubes.....	104
Figure 6.4	Platinum nanoparticle spacing as a function of ALD cycles.....	104
Figure 6.5	WAXS data for uncoated SrTiO <sub>3</sub> nanocubes.....	105
Figure 6.6	Pt nanoparticle (111) diffraction peak.....	107
Figure 6.7	Pt crystallite size vs. ALD cycles.....	107
Figure 6.8	Measured X-ray absorption spectra Pt ALD samples.....	108
Figure 6.9	Fourier transform of the Pt ALD EXAFS.....	112
Figure A.1	LEED and AFM images of SrTiO <sub>3</sub> (001) after BHF etch.....	139

Figure A.2 AFM and LEED SrTiO <sub>3</sub> (001) after different annealing conditions.....	140
Figure A.3 LEED patterns for different preparations of SrTiO <sub>3</sub> (001).....	142
Figure A.4 Diagram of the ( $\sqrt{13}\times\sqrt{13}$ )R33.7° surface structure.....	144
Figure C.1 XRR data and fits for ALD Pt on SrTiO <sub>3</sub> (001).....	149
Figure C.2 ALD Pt/SrTiO <sub>3</sub> density profiles from XRR fitting .....	150
Figure D.1 Conceptual drawing of the Be dome and reaction cell base .....	151
Figure D.2 Schematic drawing of the Be dome base.....	152
Figure D.3 Schematic drawing of the machinable ceramic base.....	153

**LIST OF TABLES**

Table 4.1	PVD Pt nanoparticle parameters from AFM / XRF .....	61
Table 4.2	PVD Pt nanoparticle parameters extracted from GISAXS analysis.....	61
Table 5.1	GISAXS fitting and analysis results for Pt ALD .....	88
Table 6.1	Pt L <sub>3</sub> edge shift for Pt ALD on SrTiO <sub>3</sub> nanocubes .....	102
Table 6.2	XANES linear combination fitting results for Pt ALD .....	111
Table 6.3	EXAFS fitting results for Pt ALD.....	113
Table B.1	XSW $f_H$ and $P_H$ for STO 012, 0.60 ML Pt / SrTiO <sub>3</sub> (001).....	146
Table B.2	XSW $f_H$ and $P_H$ for STO 013, 0.17 ML Pt / SrTiO <sub>3</sub> (001).....	146
Table C.1	Fitting results for XRR of ALD Pt/SrTiO <sub>3</sub> (001).....	149

## Chapter 1: Introduction

### 1.1 Thesis statement

Catalysis offers a unique solution to the production of energy through addressing the supply of energy by providing pathways to new fuel sources. Catalysis also reduces energy demand by improving the efficiency of a host of chemical processes and diminishing the pollution caused from the consumption of energy.<sup>1</sup> Many important energy-related catalytic processes occur with heterogeneous catalysts, where reactants and products operate in the gas phase and the catalyst exists as a solid. The most efficient heterogeneous catalysts will maximize the interface between gas and solid, which is achieved in one manner through the formation of nanoparticles where typical sizes range from a few atoms to ~5 nm in dimension.<sup>2</sup> The nanoparticle support material is also selected for its high surface area and typically consists of aerogels, nanopowders, or zeolites. Both size and morphology of the nanoparticles play intricate roles in catalytic processes.<sup>3-7</sup> The relationship between the support material and the nanoparticles also plays an important role in the chemical activity of the system. Thus, the nucleation and growth of nanoparticles on specific substrate materials is of great importance in recognizing and developing new opportunities in heterogeneous catalysis.

Catalysts are one of the most successful examples of nanotechnology and the next generation of catalysts can take advantage of technological advances in nanoscale deposition and characterization. This dissertation investigates the nucleation and growth of platinum nanoparticles supported on SrTiO<sub>3</sub> in terms of structure, morphology, and chemical state at the nanometer length scale. The approach combines atomic force microscopy (AFM) and X-ray

techniques to study the nanoparticles grown by both physical vapor deposition (PVD) and atomic layer deposition (ALD). Coalescence of nanoparticles into clusters or granular films comprises a major part of the data and analysis reported in this dissertation. The PVD grown nanoparticles exhibit a morphology consisting of aggregations of nanoparticles that appear similar to Pt nanoparticles demonstrated<sup>8-10</sup> to aggregate without coalescence or sintering. ALD offers a novel method to nucleate and grow nanoparticles that uniformly decorate complex surfaces such as aerogels<sup>11, 12</sup>, zeolites<sup>13</sup>, and other nanoparticles. ALD also constitutes a scaleable method to deliver economical loading of catalyst material<sup>11, 14</sup> while also being identified as having the potential to realize the rational design of catalysts from first principles calculations.<sup>15</sup> Through these results opportunities emerge to develop and study nanoscale solutions to the catalysis and related fields.

This project takes advantage of some of the significant advances in nanoscale structural, morphological, and chemical probes that have developed in the last twenty-five years. The advent of AFM<sup>16</sup> enabled the study of oxide-supported nanoparticles with nanometer resolution and without regard of the electrical conductivity of the sample. Grazing incidence small-angle X-ray scattering (GISAXS) was pioneered by Levine *et al.*<sup>17</sup> at Northwestern University and provides the ability to quantitatively characterize the morphology of supported nanoparticles. Another key aspect of the characterization approach is the measurement of the platinum loading via X-ray fluorescence or mass gain. Counting the platinum atoms allows for the determination of growth rate and the identification of where the platinum may be in terms of the nanoscale morphology. The chemical state of the platinum is probed using X-ray absorption spectroscopy (XAS). In particular, XAS allows for the oxidation state of the platinum to be systematically

investigated as a function of the nanoparticle size. This package of imaging, structural probes, and spectroscopy proves to be extremely useful in developing a detailed appreciation for the Pt/SrTiO<sub>3</sub> system.

## 1.2 Platinum nanoparticles

Traditional preparation of platinum catalysts typically involves wet impregnation and decomposition of a platinum-containing compound such as chloroplatinic acid (H<sub>2</sub>PtCl<sub>6</sub>).<sup>18</sup> This approach is extremely useful to load catalysts for large-scale industrial application such as catalytic converters, powder supports, and zeolites. The decomposition of H<sub>2</sub>PtCl<sub>6</sub> typically occurs through heating to some intermediate temperature (~500°C) well below the melting point of any of the materials. Opportunities to improve this process might include: improving platinum loading efficiency, reducing chlorine contamination, reducing the overall thermal budget, and providing more control of composition, morphology, and structure. Many of the opportunities may be addressed through vapor phase deposition of platinum, which includes both PVD and ALD. Of these two methods, ALD offers a more scalable technique as it easily coats complex support morphologies. However, studying both ALD and PVD methods will provide the knowledge to evaluate how nanotechnology can improve the catalysis field. Platinum nanoparticles synthesized in with vapor deposition or other vacuum techniques, have been reviewed by Henry<sup>19, 20</sup> where they are treated as model heterogeneous catalysts. PVD deposited nanoparticles may be described as model catalysts, as their deposition method does not lend itself to the geometries of industrial supports. ALD nanoparticles however show the potential of being incorporated into industrial applications because of the ability to nucleate on complex support morphologies.



The following chapter will discuss background information regarding the catalytic nature of the system and relevant issues surrounding the structure and morphology of Pt/SrTiO<sub>3</sub> (001). Chapter 3 discusses the specific background for conducting AFM and X-ray experiments on the system. Chapter 4 will discuss experimental results for the formation and behavior of nanoparticles from the evaporation of platinum metal. Chapter 5 will explain the results of a study aimed at the growth of ALD platinum from nanoparticles to granular films on SrTiO<sub>3</sub> (001). Chapter 6 will review the study of ALD deposited nanoparticles on SrTiO<sub>3</sub> nanocube powder. The final chapter will summarize the project and provide some thoughts as to the future of this particular field.

## **Chapter 2: Structure, properties, and preparation of Pt, SrTiO<sub>3</sub> and Pt/SrTiO<sub>3</sub>**

This chapter will provide the relevant information on the Pt/SrTiO<sub>3</sub> system including background on the structure, preparation, and application to heterogeneous chemical processes. The discussion will include a review of relevant literature and the experimental methods used during this project to demonstrate a method in preparing suitable Pt/SrTiO<sub>3</sub> for study at the nanometer length scale. The review will begin with the SrTiO<sub>3</sub> structure and in particular the (001) surface structure of the material and will also discuss important catalytic properties. Resulting experimental data on the (001) surface preparation will be integrated into the section. Relevant issues of platinum structure and properties will be discussed next. This section is followed by a review of important Pt/SrTiO<sub>3</sub> structural and catalytic studies. The discussion will include prior X-ray standing wave results of Pt/SrTiO<sub>3</sub> obtained in our research group, but not published thus far. The final section will discuss issues related to the course of action taken regarding the preparation of Pt/SrTiO<sub>3</sub> studied during this work.

### **2.1 Strontium titanate**

#### **2.1.1 SrTiO<sub>3</sub> in the bulk**

SrTiO<sub>3</sub> fits into the class of perovskite materials where the chemical stoichiometry is governed by the formula ABO<sub>3</sub>. The 'A' cation typically consists of metal ions from the first two columns of the periodic table and 'B' cations occupy the site with octahedral coordination. The <100> SrTiO<sub>3</sub> structure is comprised of alternating layers of SrO and TiO<sub>2</sub> as shown in Figure 2.1. The crystal structure is cubic with the  $Pm\bar{3}m$  space group (#221) and has a lattice parameter of 3.905Å.

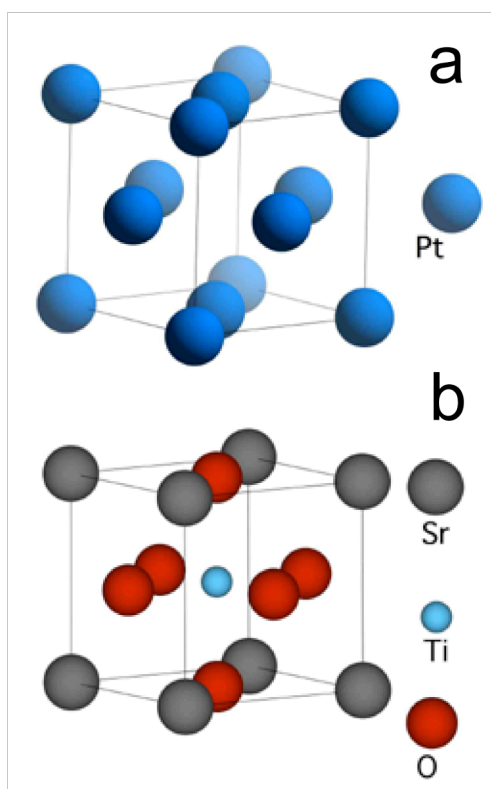


**Figure 2.1** Crystal structures for Pt (a) and SrTiO<sub>3</sub> (b). The respective lattice constants are 0.3922 nm and 0.3905 nm. The space group for Pt is  $Fm\bar{3}m$  (#225) and SrTiO<sub>3</sub> is  $Pm\bar{3}m$  (#221).

Literature studies employ both SrTiO<sub>3</sub> single crystals and powder as a catalyst support, although the latter is the only realistic industrial option for catalysts. This project employs both (001) single crystal substrates and powder. The single crystals are ultimately grown from SrTiO<sub>3</sub> powder as described below. SrTiO<sub>3</sub> powder may be synthesized from a variety of titanium and strontium compounds. Most synthetic processes produce powders of irregular shape, which have a size of a few hundred nanometers. In the last five years, novel synthesis methods have produced cube-shaped SrTiO<sub>3</sub> nanopowders.<sup>21, 22</sup> In collaboration with Northwestern researchers<sup>22</sup>, this project uses the SrTiO<sub>3</sub> nanocubes as a support for platinum nanoparticles. Ref. [22] reports nanocube powder to have cube faces with a {001} orientation, but the chemical termination of the face is not known. The {001} cube face orientation makes the measurements on the single crystal and powder complimentary.

Single crystal strontium titanate was not discovered in a natural setting until 1984.<sup>23</sup> However, bulk synthetic SrTiO<sub>3</sub> crystals have been available for scientific study since the early 1950's and SrTiO<sub>3</sub> powder was available even earlier. The most common way to grow large SrTiO<sub>3</sub> crystals is using a modified version<sup>24</sup> of the Verneuil method. The growth occurs by feeding SrTiO<sub>3</sub> powder through an oxygen-hydrogen combustion blow-pipe which melts the powder. The melted SrTiO<sub>3</sub> droplets descend onto a slowly rotating pedestal. Crystals of several inches in diameter can be grown by this method. Extensive testing of commercially available SrTiO<sub>3</sub> (001) conducted during this project has yet to find crystals with extremely high quality as measured by high-resolution X-ray diffraction. Three major substrate vendors were tested: MTI Corp. (Richmond, California), Crystal GmbH (Berlin), and CrysTec GmbH (Berlin) all had similar crystals that used the modified Verneuil method. The poor crystal quality is most

likely due to the crystal growing via a stream of molten oxide droplets that leads to a collection of crystallites forming single crystal of mosaic structures a few nanometers in dimension. Figure 2.2 is an example of a high-resolution  $\omega$ -scan through the SrTiO<sub>3</sub> (002) reflection with open 2 $\theta$  slits and the calculated reflectivity for a perfect crystal. The data were collected in the NU X-ray Diffraction Facility using the Blake 5-bounce diffractometer with Cu K $\alpha_1$  radiation. The width of the measured Bragg peak was FWHM  $\sim$  80  $\mu$ rad whereas the ideal width is 64  $\mu$ rad. The ideal reflectivity curve and width is based on the emittance from the + - /- + dispersive pair of Si(220) channel cut monochromators convoluted with the ideal SrTiO<sub>3</sub>(002) dynamical theory reflectivity curve. The broadening is due to the defect mosaic structure of the single crystal. Fig. 2.2 represents the best crystal measured during this project. Most peak widths were 1.5-2 times this width.

Aside from the catalytic use of SrTiO<sub>3</sub> discussed below, strontium titanate finds application in the microelectronics research field primarily due to its bulk lattice constant being similar to important thin film materials. During the 1990s, the material was identified as a substrate for high-temperature superconducting film materials. SrTiO<sub>3</sub> is also used as a substrate material for multiferroic films and devices. SrTiO<sub>3</sub> was considered for use as a gate material in MOSFET devices, but resonant tunneling can occur between silicon and SrTiO<sub>3</sub>, which precluded it from use in industry. Nevertheless, the result of these research efforts inspired a number of studies related to the surface structure and use of SrTiO<sub>3</sub> as a substrate material.

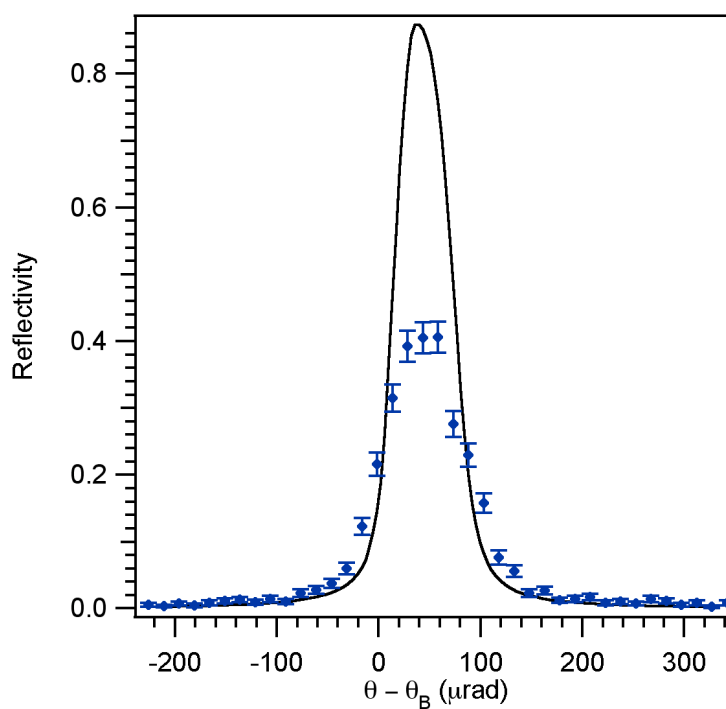


**Figure 2.2** SrTiO<sub>3</sub> (002) Bragg reflection and calculated reflectivity from dynamical X-ray diffraction theory at 8.04 keV. Both the data and the calculation include a convolution with a Si (220) monochromator. The peak width of the measured reflection is  $\sim 80$   $\mu\text{rad}$  whereas the calculated width is 64  $\mu\text{rad}$ . Defects related to the mosaic structure of the crystal broaden the diffraction peak. Data taken on the 5-bounce Blake diffractometer.

### 2.1.2 SrTiO<sub>3</sub> (001) surface structures and their preparation

To date there have been nine surface structures and reconstructions observed on SrTiO<sub>3</sub> (001) with either electron diffraction and/or STM. They include: (1x1), (2x1), (2x2), c(4x2), c(4x4), (6x2), c(6x2), ( $\sqrt{5}\times\sqrt{5}$ )R26.6°, and ( $\sqrt{13}\times\sqrt{13}$ )R33.7°. <sup>25-31</sup> The recipes to produce these structures are sometimes unreliable and indeed one of the major challenges in the surface structure of SrTiO<sub>3</sub> (001) is the lack of well-defined methods guaranteed to achieve a particular reconstruction. The structures produced during this project include the (1x1), two-domain (2x1), ( $\sqrt{2}\times\sqrt{2}$ )R45°, and the ( $\sqrt{13}\times\sqrt{13}$ )R33.7°.

Another important advance in the SrTiO<sub>3</sub> (001) surface preparation occurred in 1994 where a method to isolate the TiO<sub>2</sub> bulk termination was indentified. <sup>32</sup> Kawasaki *et al.* showed that using buffered hydrofluoric acid (BHF), the strontium-oxygen layer could be preferentially removed, leaving behind a pristine titanium-oxygen surface. Using ion scattering spectroscopy (ISS) and AFM, Kawasaki *et al.* determined the surface termination was greater than 99% titanium - oxygen with 0.4 nm tall atomic terraces, which is the height of one unit cell of SrTiO<sub>3</sub>. ISS has been used to confirm this result for a series of treatments with slight variations in buffer pH and other experimental parameters. <sup>33-36</sup> Prior to the BHF discovery most studies focused on spectroscopy of the surface using photoelectron and Auger electron probes. Following the Kawasaki paper, a series of structural studies cataloged a number of surface reconstructions observed with diffraction and/or scanning tunneling microscopy (STM). <sup>25-31, 35, 37-42</sup>

The following will discuss an example of SrTiO<sub>3</sub> (001) preparation for the most common reconstruction observed during this project, which is the ( $\sqrt{13}\times\sqrt{13}$ )R33.7°. This result was a byproduct of the efforts to prepare the (2x1) using an oxygen-annealing step. The reconstruction

is prepared by first etching with the BHF solution followed by annealing in flowing oxygen that can range from 900-1050°C and for five to twelve hours. The process produces clean atomic terraces which have a  $(\sqrt{13}\times\sqrt{13})R33.7^\circ$  reconstruction. Figure 2.3 (a) shows the AFM image for a substrate polished by the manufacturer giving an RMS roughness of 0.14 nm and the image of a substrate etched and annealed for 5 h at 1050°C in flowing oxygen to produce the atomic terrace structures in (b) which possess the  $(\sqrt{13}\times\sqrt{13})R33.7^\circ$  shown in 2.3 (c). This result is similar to the results reported in the literature where the  $(\sqrt{13}\times\sqrt{13})R33.7^\circ$  was observed using reflection high- energy electron diffraction (RHEED) after annealing in oxygen for 2 hours at 800°C.<sup>31</sup> The structure was tested for stability during this project by iteratively collecting the LEED pattern after exposing to air. The LEED pattern persisted for a little over an hour of total exposure time to ambient. The  $(\sqrt{13}\times\sqrt{13})R33.7^\circ$  pattern was also observed with TEM in collaboration with other Northwestern researchers (L.D. Marks group). Pre-thinned TEM samples were etched and annealed in the same manner as described above and then subsequently transferred to the TEM for imaging. The  $(\sqrt{13}\times\sqrt{13})R33.7^\circ$  was selected for platinum nanoparticle studies because of the clean terraces and the relative ease of preparation. Details of the preparation and results of the other reconstructions and LEED patterns observed during this project can be found in Appendix A.



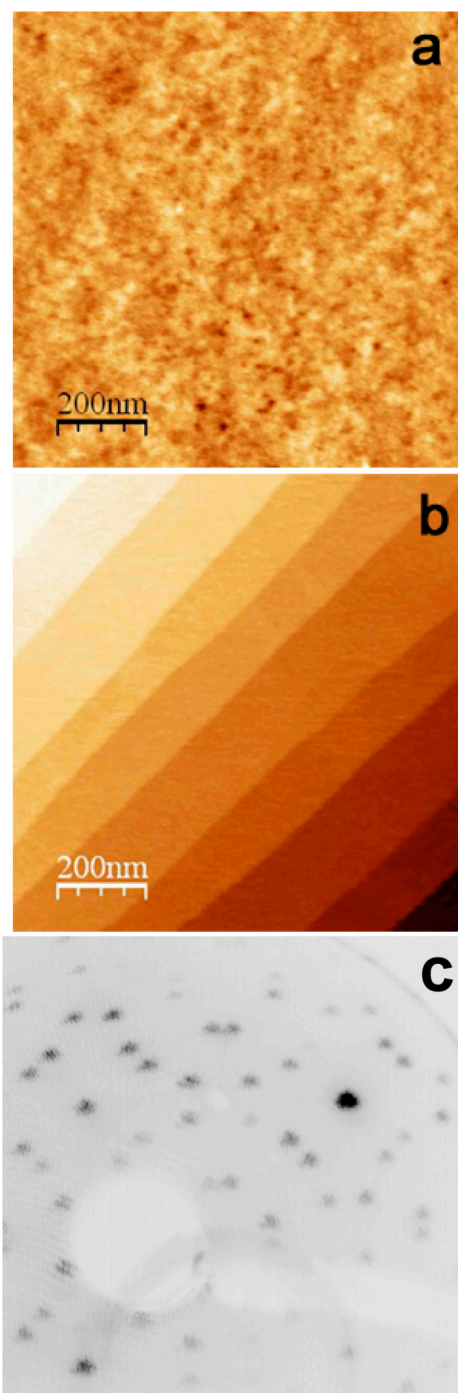


**Figure 2.3** SrTiO<sub>3</sub> sample preparation: a) AFM image of a substrate polished by the manufacturer with RMS roughness of 0.14 nm; b) AFM image of clean atomic steps after BHF etch and annealing in an oxygen atmosphere; c) ( $\sqrt{13} \times \sqrt{13}$ )R33.7° LEED pattern (inverted intensity) following the BHF etch and O<sub>2</sub> anneal. The LEED pattern was collected at 46.7 eV.

### 2.1.3 SrTiO<sub>3</sub> (001) surface morphology

At the nanometer length scale the morphology of the (001) surface shows a variety of structures associated with atomic terraces. Szot and Speier give the most detailed account of ‘oxidized’ and ‘reduced’ surfaces based on scanning probe microscopy of samples annealed for 24 h.<sup>43</sup> For oxygen annealing, they observe a solid state reaction where the topmost layers of SrTiO<sub>3</sub> transform to the Ruddlesdon-Popper (RP) phase, Sr<sub>2</sub>Ti<sub>4</sub>O<sub>7</sub>.<sup>44</sup> The growth of the RP phase coincides with a large change in the atomic terrace step height, from 0.4 to 1.2 nm, which correlates with SrO enrichment at the surface. Using lateral force microscopy (LFM) Fompeyrine *et al.* observed frictional contrast between atomic terraces 0.2 nm tall.<sup>45</sup> They concluded that both TiO<sub>2</sub> and SrO terminated steps were present and that the TiO<sub>2</sub> terminated steps have a lower frictional contrast. Thus, faceted steps correspond to the TiO<sub>2</sub> termination and that steps vertically offset 0.2 nm with curved edges correspond to the SrO terminated surface.

Another interesting feature found on the (001) surface is the formation of voids one unit cell deep and up to a few hundred nanometers across. Examples of this morphology produced during this project are reported in Appendix A. An example of the hole morphology in the literature is given by Koster and coworkers<sup>46</sup> where they note the appearance of holes after annealing in oxygen for 1 h at 950°C. From their observations, the holes are perfect circles and diffuse to the step edges in time. Szot and Speier also observe holes but under reducing conditions. Two-dimensional voids were observed on synthetic  $\alpha$ -Fe<sub>2</sub>O<sub>3</sub> (0001) by atomic force microscopy.<sup>47</sup> The voids in this case consisted of circles approximately 1  $\mu$ m in diameter and 0.23 nm deep as shown in Figure 2.4.

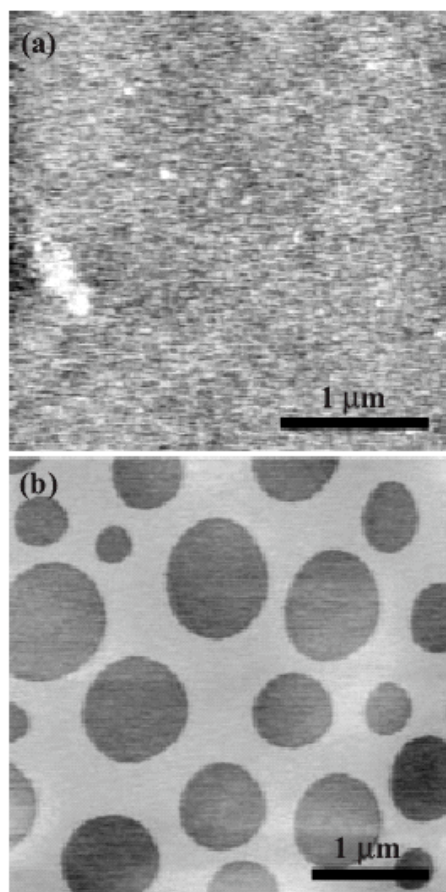


**Figure 2.4** AFM images of  $\alpha\text{-Fe}_2\text{O}_3$  (001) (a) before and (b) after annealing. The RMS roughness in (a) prior to annealing is 0.04 nm and the step height for the holes is  $0.22 \pm 0.02$  nm. The Fe – Fe height difference along the (001) axis of the unit cell is 0.23 nm. The formation of holes and voids similar to this has also been observed in the literature and during this study. Image taken from Ref. [47].

The formation of the voids occurred after annealing the crystal in an oxygen-rich environment at ambient pressure similar to the SrTiO<sub>3</sub>. The mechanism of void formation was attributed to a dipole interaction due to multiple concurrent reconstructions of the oxide surface.<sup>48, 49</sup> Additional experimental evidence of the phenomena is demonstrated for Si(111) and Pb/Cu(111).<sup>50-52</sup> The formation of voids in SrTiO<sub>3</sub> may also be related to the surface reconstruction in a similar fashion.

#### **2.1.4 Role of chemical termination in the SrTiO<sub>3</sub> (001) surface**

The TiO<sub>2</sub> termination forms the basis to describe prevailing sentiment of the different surface reconstructions observed by diffraction and STM. Erdman and Marks summarized many of these structures along with the preparation method.<sup>25</sup> The explanations for the surface reconstructions are generally attributed to the ordering of oxygen vacancies in the TiO<sub>2</sub> surface termination to produce a structure with long-range order. This model was developed from Tanaka *et al.* by correlating scanning tunneling microscopy/spectroscopy measurements to photo-emission spectroscopy studies related to oxygen vacancies.<sup>53, 54</sup> An alternate model based STM and theoretical calculations proposed that the ordering of Sr adatoms was behind many of the surface reconstructions.<sup>30</sup> In any case, it suffices to note that the (001) surface is extremely complex and that many of the surface structures remain an open question today, but that the TiO<sub>2</sub> layer probably plays an intricate role. This notion is supported by studies that elucidate the chemical activity of the SrTiO<sub>3</sub> (001) surface.<sup>25</sup>

Several studies have identified the chemical state of Ti in the SrTiO<sub>3</sub> (001) surface plane to play the principle role in chemical and photochemical processes. The Ti<sup>3+</sup> ion has been shown to play a role in dissociative adsorption of NO, CO, and CO<sub>2</sub>.<sup>55, 56</sup> The Ti species has also been

linked to the photoactivity of the surface in the photo-assisted reduction of  $\text{Ag}^+$  and oxidation of  $\text{Pb}^{2+}$  in solution on  $\text{SrTiO}_3$  (001), (110) and (111).<sup>57</sup> AFM measurements confirmed the formation of Ag and  $\text{PbO}_2$  precipitates on the (001) and (111) atomic terraces that were believed to have the  $\text{TiO}_2$  termination. Matsumoto and coworkers observed a surface termination effect when they deposited pentacene films on SrO and  $\text{TiO}_2$  terminated  $\text{SrTiO}_3$  (001).<sup>58, 59</sup> After UV illumination the film was observed by AFM to degrade on the  $\text{TiO}_2$  surface whereas the SrO surface produced no degradation. The mechanism for film degradation was attributed to photo-induced oxidation of the film via electron transfer to adsorbed  $\text{O}_2$  or  $\text{H}_2\text{O}$ . This mechanism would also be consistent with the photocatalytic mechanisms of bare  $\text{TiO}_2$  where the Ti ions and oxygen vacancies serve as reaction sites.<sup>60</sup>

## 2.2 Platinum structure and properties

Figure 2.1 shows the platinum structure is face-centered-cubic (FCC) which has the  $\text{Fm}\bar{3}\text{m}$  space group (#225). The lattice constant of Pt is 3.922 Å, which is very close to  $\text{SrTiO}_3$ . Because the unit cells are in the same family with the  $\text{m}\bar{3}\text{m}$  symmetry designation, the diffraction peaks will be very close to each other.  $\text{SrTiO}_3$  unit cell has no forbidden diffraction peaks whereas the FCC diffraction rules apply for platinum, meaning mixed  $hkl$  peaks are absent. This makes it difficult to study platinum diffraction apart from  $\text{SrTiO}_3$  substrate diffraction when the two materials are paired together. The platinum diffraction peaks will be at slightly smaller  $2\theta$  angles, however.

Platinum generally appears to be quite inert and refractory. It has a relatively high melting point (1780°C) and does not easily oxidize when heated in oxygen. Nevertheless, platinum will form a variety of stoichiometric oxides including PtO,  $\text{PtO}_2$ , and  $\text{Pt}_3\text{O}_4$ . Platinum

is one of the most important catalytic materials used in energy technologies despite its apparent chemical inertness. Catalytic converters utilize platinum catalysts to reduce CO and NO<sub>x</sub> emissions from automobiles. Furthermore, platinum based catalysts can be employed in reforming and isomerization reactions to produce fuels including gasoline. Fuel cells use platinum extensively to facilitate the conversion of hydrogen and oxygen in polymer membrane architectures and in the case of solid oxide fuel cells as a high-temperature electrode material. Platinum is also used extensively in the electrolysis and photochemistry as a cathode material; it does not degrade under reaction conditions and interacts favorably with hydrogen.

## **2.3 Pt / SrTiO<sub>3</sub> (001)**

### **2.3.1 Pt/SrTiO<sub>3</sub> (001) structure and morphology**

There have been a number of theoretical and experimental studies regarding Pt/SrTiO<sub>3</sub>. Density functional theory (DFT) studies of platinum on different orientations of SrTiO<sub>3</sub> show that the (001) orientation possesses the weakest interface when compared to the polar (110) and (111) surfaces.<sup>61, 62</sup> This was determined by calculating the work of separation for the Pt/SrTiO<sub>3</sub> interface. The (001) surface was differentiated further between the TiO<sub>2</sub> and SrO chemical terminations.<sup>61</sup> The DFT studies placed the platinum atoms directly over the lattice oxygen for either TiO<sub>2</sub> or SrO terminations. The calculations also indicated the Pt/TiO<sub>2</sub> interface to be stronger of the two.

The Pt/TiO<sub>2</sub> and Pt/SrO interfaces have also been investigated experimentally.<sup>63</sup> Polli *et al.* observed the epitaxy of Pt grains in a 20 nm film to depend on the chemical termination. Specifically, they observed a (001) cube-on-cube epitaxy of the platinum grains on both the TiO<sub>2</sub> termination and after 0.5 ML of SrO had been deposited onto a TiO<sub>2</sub> terminated surface. For 2

ML of SrO, both (001) and (111) oriented Pt grains were present. They attributed this to the Pt/SrO not having a strong enough interaction to overcome the entropy cost associated with multiple platinum orientations.

Another study found that platinum on SrTiO<sub>3</sub> (001) surfaces would exhibit (001) cube-on-cube epitaxy while the substrate was being held at 600°C whereas below this only (111) Pt epitaxy was observed.<sup>64</sup> This study, however, did not use the BHF etch nor did it show verification of the chemical termination of the SrTiO<sub>3</sub>. Additional experimental studies of Pt/SrTiO<sub>3</sub> have demonstrated granular films and nanoparticles to consist of a variety of different epitaxial grains.<sup>63-66</sup> These studies all focus on initial platinum film thicknesses of two nanometers or more. Chapter 4 focuses specifically on the behavior of Pt for the first few monolayers of growth on SrTiO<sub>3</sub>.

The complexity of the Pt/SrTiO<sub>3</sub> (001) surface requires extreme care to be taken in sample preparation. An unpublished example of this comes from a former Bedzyk group member,

A. Kazimirov, in an X-ray standing wave (XSW) study of Pt/SrTiO<sub>3</sub>. After depositing platinum on a (2x1) reconstructed SrTiO<sub>3</sub> (001) surface, the platinum atoms took up a structure similar to FCC with (001) cube-on-cube epitaxy with the SrTiO<sub>3</sub>. Figure 2.5 shows the platinum structure from XSW data for 0.2 ML Pt and 0.6 ML Pt. There is approximately a one-half unit cell vertical shift between the 0.2 monolayer (ML) and 0.6 ML cases. Efforts to reproduce and extend this study were conducted during this project without success. The major reason was due to the difficulty in preparing the proper surface conditions to achieve a strong epitaxial interface between the platinum and SrTiO<sub>3</sub>.

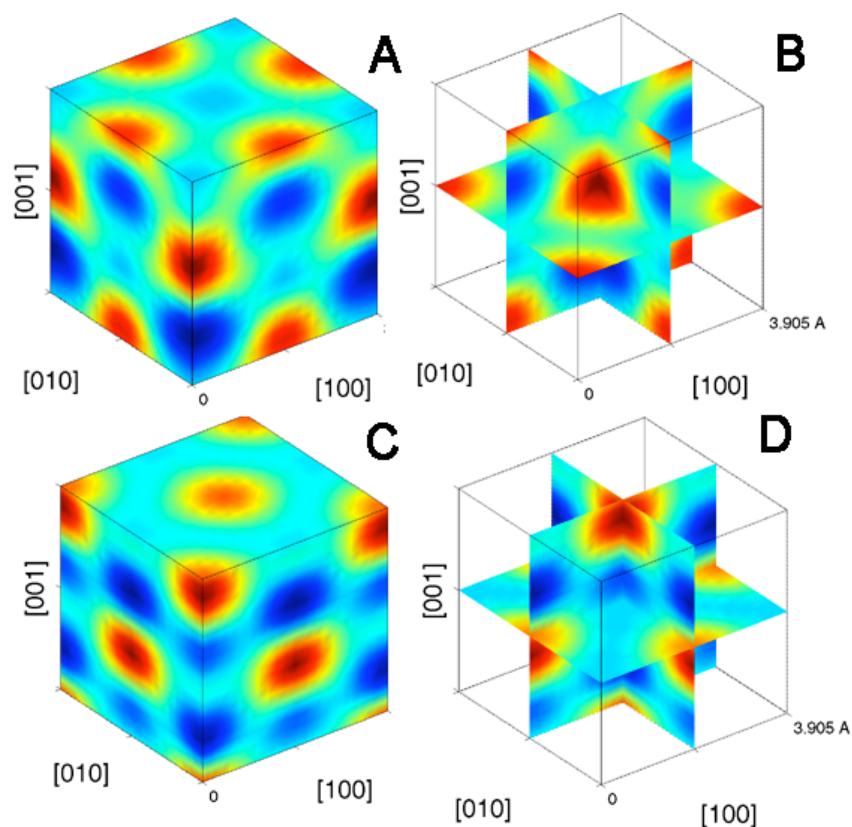


**Figure 2.5** Atomic density maps for Pt supported on SrTiO<sub>3</sub> (001) based on XSW data collected by A. Kazimirov at the APS 12ID-D station. (A) and (B) represent 0.6 ML Pt; (C) and (D) are for 0.2 ML Pt. For 0.60 ML Pt the structure assumes an FCC structure resting atop the SrTiO<sub>3</sub>. The 0.2 ML Pt case shows a similar FCC structure only that it is shifted along the [001] direction approximately one-half of unit cell when compared to the 0.60 ML Pt case.



The efforts produced platinum nanoparticles dispersed on the surface with no particular orientation relative to the support. Poor SrTiO<sub>3</sub> crystal quality was also a contributing factor as it made the XSW measurements more difficult. More information on the XSW results can be found in Appendix B.

### 2.3.2 Catalytic properties of the Pt/SrTiO<sub>3</sub> system

SrTiO<sub>3</sub> has been used in the photodecomposition of water and other small hydrocarbons to produce hydrogen for energy storage. The interest in hydrolysis began from a study aimed to offset the applied bias of -1.23 V required to split water by way of photoelectrolysis.<sup>67</sup> SrTiO<sub>3</sub> was found to exhibit excellent stability under reaction conditions and efficiently produce H<sub>2</sub> under no applied bias using UV light.<sup>68</sup>

Once SrTiO<sub>3</sub> was identified as a potential photocatalyst, a series of studies was launched to develop a viable route to hydrogen production from water.<sup>69-71</sup> The catalyst consisted of a thin Pt film on a SrTiO<sub>3</sub> (111) substrate. Reactions were conducted in aqueous solutions of NaOH<sup>69-71</sup> or with water vapor and NaOH films dried on the Pt/SrTiO<sub>3</sub> (111).<sup>72</sup> Using photoelectron spectroscopy, they linked the catalytic activity to Ti<sup>3+</sup> sites on the SrTiO<sub>3</sub> (111). Furthermore, they noted a relationship between the increase of hydrogen evolution with a decrease in Pt film thickness down to some optimal Pt ML thickness. This observation is part of the motivation behind this project as new techniques to study ultra-thin films have since emerged.

Domen and coworkers observed pure water splitting for both SrTiO<sub>3</sub> powder and NiO or CoO coated SrTiO<sub>3</sub> powder.<sup>73-76</sup> The NiO/SrTiO<sub>3</sub> catalysts were capable of producing ~0.05 mmol/h of hydrogen as compared to the approximate ~10<sup>-3</sup> mmol/h from the Pt/SrTiO<sub>3</sub> (111) reported in Ref. [72]. Recently, the Domen group has reported a ~0.5 mmol/h rate of hydrogen

evolution using visible light.<sup>77</sup> This material is based on a GaZnO solid solution with rhodium/chromium oxide nanoparticles.

In addition to decomposing water, SrTiO<sub>3</sub> and Pt/SrTiO<sub>3</sub> have shown promise in forming methanol from different mixtures containing water, CO<sub>2</sub>, and formaldehyde.<sup>78, 79</sup> Along with the potential of a fuel source, reactions such as these have a beneficial impact on the environment. Photo-assisted environmental catalysis has played a major role in decomposing heavy organic contaminants in water via mineral deposits of TiO<sub>2</sub>. SrTiO<sub>3</sub> does not necessarily provide a major role in environmental catalysis due to its rarity. Nevertheless, SrTiO<sub>3</sub> is similar in photocatalysis as it has a similar band gap.

Platinum nanoparticles supported on wide band gap semiconductors like TiO<sub>2</sub> and SrTiO<sub>3</sub> are said to short circuit the photoelectrochemical cell and create a photocatalyst. The following is a brief synopsis of the photocatalytic process based on a review by Linsebigler *et al.*<sup>60</sup> Heterogeneous photocatalysis operates under two major mechanistic regimes based on either the photoactivation occurring in the adsorbed reactant or the photoactivation occurring in the photocatalyst. The reaction is catalyzed by either electron transfer or energy transfer, which leads to the photodecomposition of the reactants to products. The mode at which Pt/SrTiO<sub>3</sub> operates is based on the photoactivation occurring within the catalyst particle where the electrons generated in the conduction band of SrTiO<sub>3</sub> diffuse to the surface to participate in the reaction. The ability of the SrTiO<sub>3</sub> to undergo photocatalytic electron transfer lies in the relationship between the redox potentials of the adsorbate (e.g. water) to its constituents. Thus the SrTiO<sub>3</sub> conduction band must lie above the relative potential of the acceptor (hydrogen) and the valence band must be below the donor species (oxygen). This requires the band gap to exceed the redox

potential of water (-1.23 V) which SrTiO<sub>3</sub> does indeed at 3.2 eV. A major challenge to the efficiency of photocatalysts is the recombination of carriers before they participate in a photoreaction. The addition of platinum nanoparticles is in part a solution to this problem as the metal/oxide interface creates a Schottky barrier whose rectifying nature traps the electrons within the metal nanoparticle. The electrons are then ideally localized to participate in the photoreaction. The metal also facilitates reactant adsorption to the catalyst particle.

In addition, SrTiO<sub>3</sub> may serve as an oxidative catalyst support effective at preventing carbonaceous build-up termed *coking*.<sup>80-83</sup> Inefficient catalysis leads to coking as the reaction rate exceeds the ability of the catalyst to process the products. The result is carbonaceous deposits on the surface, which requires a costly regeneration step of heating in oxygen to burn off the carbon. SrTiO<sub>3</sub> as an anticoking support compared favorably to other supports in a fundamental study of partial oxidation of methane by nickel catalysts.<sup>83</sup> SrTiO<sub>3</sub> had the smallest catalyst particle size which were also well-dispersed. The build up of carbon was sequestered through the reaction of lattice oxygen from the perovskite to form CO in the gas phase. This of course leads to oxygen defects in the SrTiO<sub>3</sub>, but it prolonged the time necessary for catalyst regeneration. Ni and Co catalysts on SrTiO<sub>3</sub> show promise in the steam reforming of ethanol to produce hydrogen.<sup>82</sup> Since platinum is well known to be an effective combustion catalyst, the combination of Pt and SrTiO<sub>3</sub> would be useful due to their complimentary catalytic properties.

#### **2.4 Selection of the SrTiO<sub>3</sub> (001) surface preparation method**

For single crystal SrTiO<sub>3</sub>, this project ultimately focused on the procedure that produces the clean atomic terraces with the ( $\sqrt{13}\times\sqrt{13}$ )R33.7° LEED pattern by BHF etching and oxygen annealing. This procedure was selected on the merit that the clean/flat atomic terraces were the

ideal backdrop to study nanoparticle formation using AFM. The typical recipe included degreasing by sonication with organic solvents followed by sonication in deionized water for 15 minutes. The BHF etching was performed for 45-60 s using a commercially available solution (Riddel-de Haen, part. No 40207) with a pH  $\sim$  5. The oxygen annealing occurred in a tube furnace with a  $\sim$ 100 sccm flow of high-purity oxygen at temperatures ranging from 1025-1050°C for 5 h. This method also had the advantage for batch processing of substrates and annealing in oxygen is relevant to treatments that are performed in industrial settings. Furthermore, the etching and annealing are believed to produce a predominantly TiO<sub>2</sub> chemical termination. Based on the literature review above, this termination appears to be the most chemically active. Hence, this preparation method was selected for single crystal studies.

The SrTiO<sub>3</sub> nanocubes were provided by Federico Rabuffetti of the Stair and Poeppelmeier groups. Details of the nanocube growth are given in [22]. No additional treatments were performed prior to the ALD process. The work on the nanocubes is reported on in Chapter 6.

## Chapter 3: Experimental Characterization Methods

This chapter provides the motivation for combining atomic force microscopy with X-ray techniques to study metal nanoparticles supported on insulating substrates. The first section reviews selected examples of the combination of X-ray and AFM. The following section covers the general experimental details regarding AFM experiments conducted during this project. The final sections provide the theoretical basis for the X-ray techniques primarily employed during this project including SAXS/GISAXS, X-ray fluorescence (XRF), and X-ray absorption spectroscopy.

### 3.1 Atomic force microscopy combined with X-ray techniques

The combination of AFM and X-ray techniques provides a powerful set of tools in studying materials at the nanometer length scale. The method has been exploited in the characterization of self-assembled monolayers<sup>81, 82, 84, 85</sup>, quantum dots<sup>83, 86</sup>, and oxide systems<sup>84, 85, 87, 88</sup> to name a few relevant examples. In addition to the aid AFM images give in the interpretation of the X-ray data, the combination of AFM and X-ray has improved the throughput for sophisticated synchrotron experiments by serving as a screening tool for potential samples to be used at the beam line.<sup>81, 82, 85, 84, 85, 88</sup> The screening is based on successful X-ray results correlating with AFM images that show the atomic terrace morphology is not significantly altered through the sample processing and measurement.

### 3.2 AFM methods

Both contact mode and tapping mode were used in this project with the majority of the work being done in tapping mode in air. Tapping mode offers better lateral resolution as it is not susceptible to mechanical vibrations from the environment and has less tip/sample interaction as

opposed to contact mode. In addition to the topography studies, lateral force microscopy (LFM) and phase imaging were tested to hopefully provide chemical contrast between the platinum nanoparticles and the substrate. However, this became unrealistic because of the convolution between the topography signal and LFM/phase signal. The three-dimensional nature of the nanoparticles makes scan parameters (gain and scan speed) difficult to optimize for LFM such that the feedback responds appropriately to the nanoparticle. Scan conditions are optimized by scanning a region successively while varying the gain and scan speed until the differences in the height profile for the left to right and right to left traces is negligible.

The lateral resolution of the AFM is dictated by the sharpness and cleanliness of the tip. The most common tip materials are silicon and silicon nitride and the nominal radius of curvature for standard AFM tips is about 10 nm. Various schemes have been designed to improve the resolution, but beating a 1 nm radius of curvature is difficult. This project utilized the NSC tip series from  $\mu$ Mach, which featured 10 nm silicon tips. The typical resonant frequencies were  $\sim 75$  kHz, although other NSC cantilevers with higher resonant frequencies were also used. In some cases, ultra-sharp tips ( $\sim 1$ nm) were employed but did not yield superior data.

Calibration of the AFM height was performed using the atomic terraces of  $\text{SrTiO}_3$  (001) and  $\alpha$ - $\text{TiO}_2$  (110) single crystals. The nominal terrace step for  $\text{SrTiO}_3$  and  $\text{TiO}_2$  are 0.39 nm and 0.32 nm, respectively. These crystals were selected because of the ease in which to prepare extremely clean atomic terraces. For the nanoparticle samples, care was taken to capture atomic steps concurrently with the nanoparticles. Atomic steps within the field of view of nanoparticles provide each image with a vertical calibration scale.

### 3.3 X-ray Techniques

#### 3.3.1 Small-angle X-ray scattering

The intensity measured in small-angle X-ray scattering is a function of the fluctuations of electron density and contrast of the system on a length-scale greater than  $\sim 1$  nm. The scattered intensity is described as a function of the scattering vector,  $\mathbf{q}$ , which is the momentum transfer of the incident ( $\mathbf{k}_i$ ) and scattered ( $\mathbf{k}_f$ ) wave vectors where:  $\mathbf{q} = \mathbf{k}_f - \mathbf{k}_i$ . The amplitude of scattered intensity for a single particle or structure is given by:

$$F(\mathbf{q}) = \int \rho(\mathbf{r}) s(\mathbf{r}) e^{-i\mathbf{q}\cdot\mathbf{r}} d\mathbf{r} \quad (3.1)$$

$$I(\mathbf{q}) = |F(\mathbf{q})|^2 \quad (3.2)$$

where  $\rho(\mathbf{r})$  is the electron density and  $s(\mathbf{r})$  is a function defining the shape of an individual scattering body (e.g. sphere, cylinder, ...).<sup>86-89</sup> Some authors define  $\rho(\mathbf{r})$  to include the nanoparticle shape and thus they replace  $s(\mathbf{r})$  and  $\rho(\mathbf{r})$  with just  $\rho(\mathbf{r})$ , as will be the case for the remainder of this dissertation.  $|F(\mathbf{q})|^2$  is known as the form factor and is represented hereunder with the kinematical or Born approximation. The application of the Born approximation in this context for SAXS is based on the assumption that the scattered  $e$ -field intensity is small compared to the incident  $e$ -field intensity. This is the case for typical systems studied by SAXS such as nanoparticles, biological structures, polymers etc. The kinematical approximation implies that X-rays are scattered once and that there are no refraction effects.

The scattered intensity for a sphere of uniform density,  $\rho_0$ , radius,  $R$ , and volume,  $V$ , is obtained from eq 3.1 and eq 3.2 as:

$$I(q) \propto |F(q)|^2 = \rho_0^2 V^2 \frac{9[\sin(qR) - qR \cos(qR)]^2}{(qR)^6} \quad (3.3)$$

The calculated intensity is plotted for a set of spheres of different  $R$  in Figure 3.1 along with the  $q^{-4}$  slope, which is the asymptotic behavior for scattering bodies with hard interfaces. The oscillations are due to the coherent scattering from an extremely narrow size distribution, which is a delta function in this case. The inverse relationship between real space and the momentum transfer is evident as the intensity decays more slowly for small spheres and the oscillation period is larger for smaller spheres. For randomly oriented particles without spherical symmetry, the scattered intensity will be a geometric average of the particle shape in all directions.

For polydisperse systems with non-interacting particles, the scattered intensity represents the average form factor  $\langle |F(\mathbf{q})|^2 \rangle$ . Figure 3.2 shows a series of calculated intensity curves of the scattering from a collection of spheres. The size distribution of spheres is taken as a Gaussian centered on  $R_0 = 5$  nm with varying width,  $\sigma$ . As the distribution width increases, the oscillations are smoothed and the intensity decays more slowly as a function of  $q$ . The relationship between scattered intensity and the number distribution,  $D_n(R)$ , and particle size,  $R$ , is given by<sup>90</sup>:

$$I(q) = \int D_n(R) |F(qR)|^2 R^6 dR. \quad (3.4)$$

Eq 3.4 provides a basis for modeling SAXS data to extract a size distribution for a system so long as there is a well-defined form factor.

Another tool more rudimentary for determining the size of scatters is the Guinier approximation.<sup>89</sup> The approximation is based on the Taylor series expansion of eq 3.1 and is derived in almost all SAXS texts. The result is quoted here:

$$I(q) \propto (\rho_0 V)^2 \exp\left(-\frac{1}{3} q^2 R_g^2\right), \quad qR_g < \frac{\pi}{2}. \quad (3.5)$$



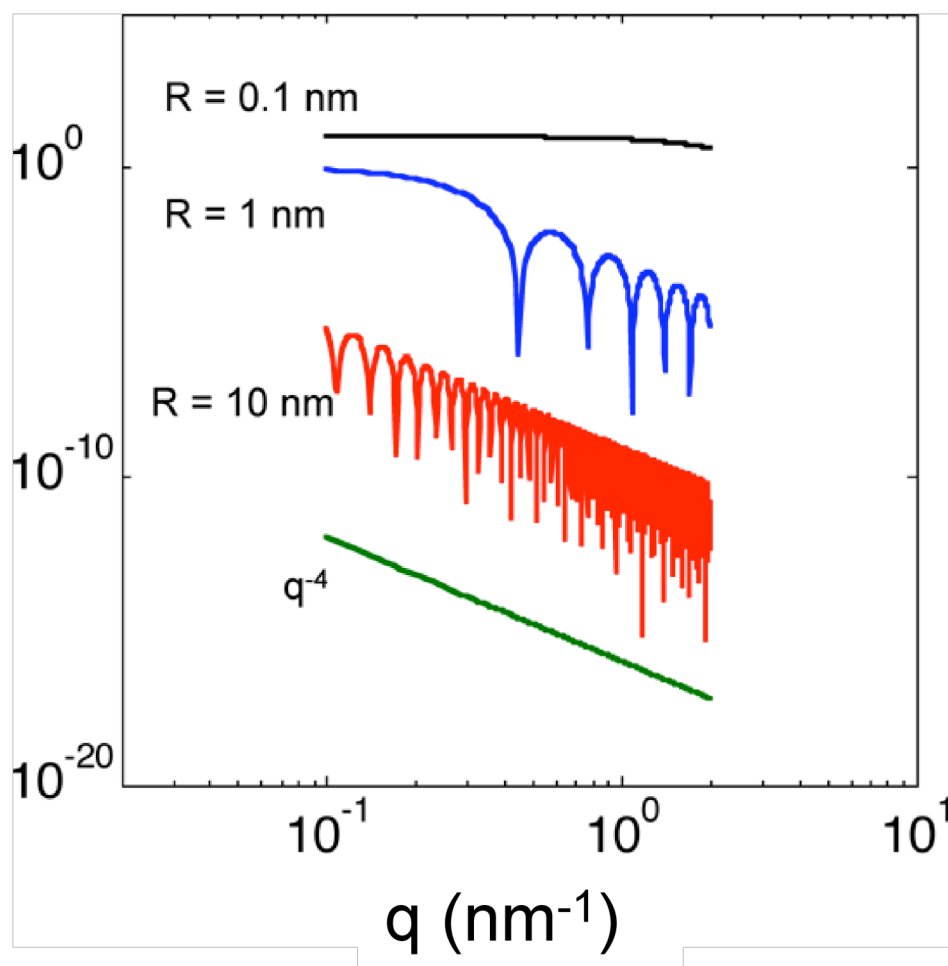


**Figure 3.1** Calculated SAXS intensity for a series of spheres of different radii. The oscillations are a result of the coherent interference from an extremely narrow size distribution where the period is related to the particle size. The  $q^{-4}$  slope gives the asymptotic scattering behavior for systems with hard interfaces.

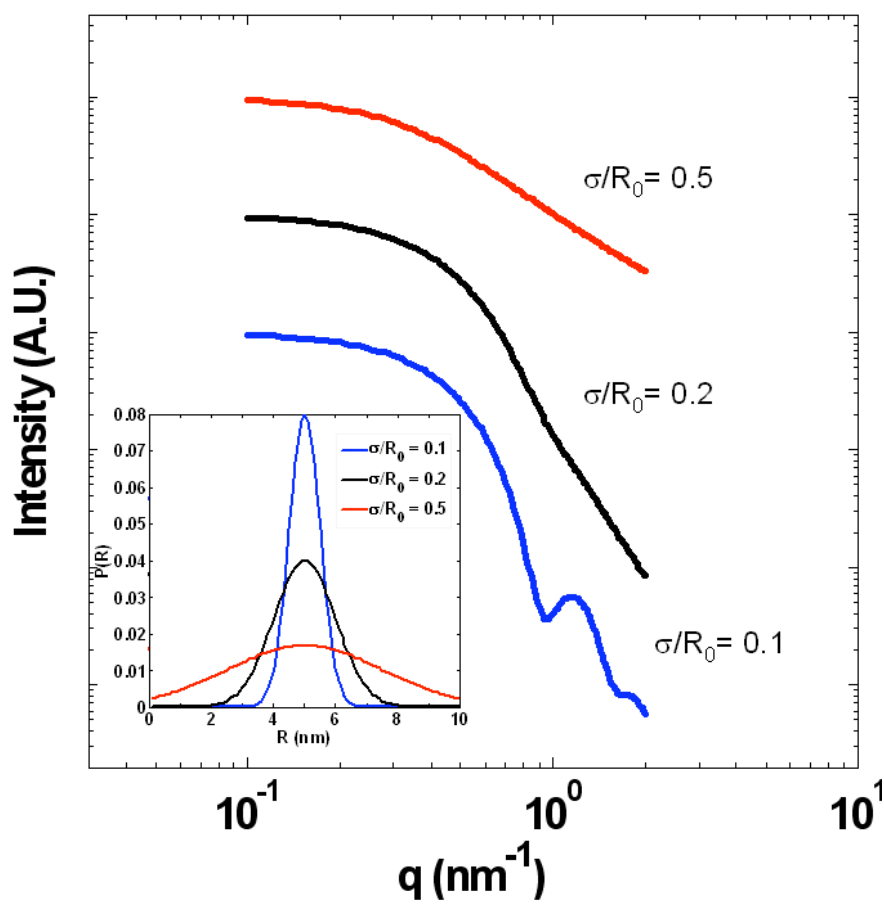


**Figure 3.2** Calculated SAXS for polydisperse spheres with Gaussian size distributions centered on  $R_0 = 5$  nm and width,  $\sigma$ . As the  $\sigma$  increases, the oscillations are damped and the scattered intensity decays more slowly.

The quantity  $R_g$  is known as the radius of gyration for the electron density and may be calculated using:

$$R_g^2 = \frac{\int r^2 \rho(\mathbf{r}) d\mathbf{r}}{\int \rho(\mathbf{r}) d\mathbf{r}}. \quad (3.6)$$

For a sphere of uniform density,  $\rho_0$ , with radius  $R$ , the radius of gyration is given by  $R_g = (3/5)^{1/2}R$  from eq 3.6. The Guinier approximation makes for a convenient method of data analysis as the  $R_g$  may be determined by plotting the natural logarithm of intensity versus  $q^2$ . Figure 3.3 shows an example of the application of the approximation for the calculated intensity of spheres with a width ratio  $\sigma/R_0 = 0.2$  and  $R_0 = 5$  nm. The calculated  $R_g$  based on eq 3.6 is 3.873 nm whereas the slope of the fit from Figure 3.3 yields 3.871 nm.

The discussion up to this point has focused on hard, non-interacting objects that are widely separated. When the objects are closely spaced and/or have some interparticle attractive force, the intensity will need to account for the interactions. The scattering intensity,  $I(\mathbf{q})$ , for a collection of  $N$  particles is given by<sup>89, 91</sup>:

$$I(\mathbf{q}) = \sum_i^N \sum_j^N F_i^*(\mathbf{q}) F_j(\mathbf{q}) \exp[-i\mathbf{q} \cdot (\mathbf{x}_i - \mathbf{x}_j)], \quad (3.7)$$

where  $\mathbf{x}_i$  locates the position of the  $i^{\text{th}}$  nanoparticle and  $F_i(\mathbf{q})$  is the scattering amplitude of the  $i^{\text{th}}$  nanoparticle. In some cases, eq 3.7 may be simplified by using the average form factor and an interference function,  $S(\mathbf{q})$  to have a general form of:

$$I(\mathbf{q}) = \langle F(\mathbf{q})^2 \rangle \otimes S(\mathbf{q}) \quad (3.8),$$

where  $\otimes$  denotes a convolution. The  $S(\mathbf{q})$  can be modeled as a thermodynamic potential that governs the forces of attraction and repulsion within the system.

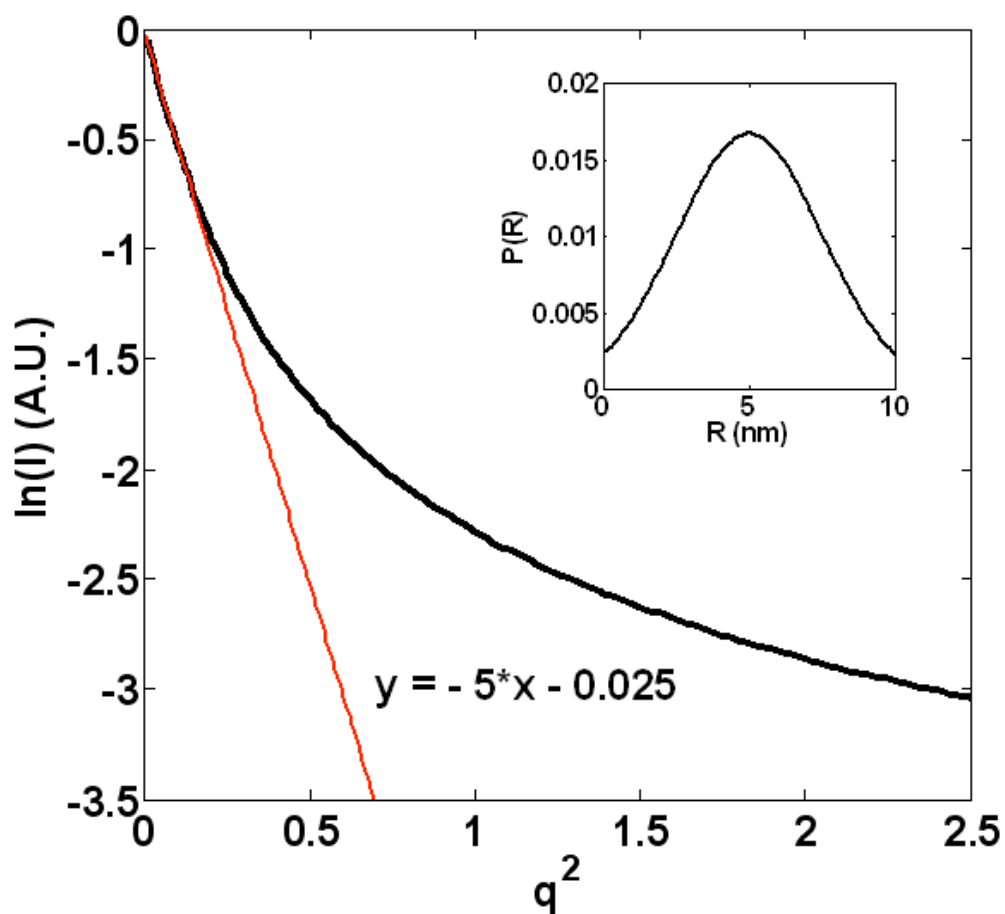


**Figure 3.3** Guinier plot for calculated polydisperse spheres. The Guinier approximation applies to the regions where the scattering decays by an exponential law as a function of  $q^2$ . By fitting a line to this region, the radius of gyration,  $R_g$ , is extracted which is the average size dimension for the scattering bodies. The calculated intensity for polydisperse spheres with an average radius of 5 nm is plotted against  $q^2$ . The slope of the fit (straight line) for the Guinier region gives  $R_g = 3.871$  nm whereas the exact value from eq 3.6 is 3.873 nm.

This is particularly useful when the sample conditions are conducive to achieving a thermodynamic equilibrium such as colloids in solution. When equilibrium is not realistic,  $S(q)$  is modeled as a regular diffraction peak. In some cases where the interparticle interference scattering lies at higher values of  $q$ ,  $\langle |F(q)|^2 \rangle$  takes on a power law asymptotic behavior:  $q^{-4}$ . An example of this is employed in Chapter 6 to measure the interparticle spacing for Pt nanoparticles on SrTiO<sub>3</sub> nanocube powder. Another treatment of the contribution of interparticle scattering in SAXS describes the spacing in terms of the volume fraction of scattering bodies,  $\nu$ .<sup>92</sup> Figure 3.4 shows an example where the interference function is calculated for a closely packed system with different volume fractions. When  $\nu = 0$ , the scattering is from a single particle. As  $\nu$  increases, the coherent scattering between the particles creates a peak at  $q = q_p$ .

The peak at  $q_p$  provides important information of the system as it is related to the autocorrelation of the particles and can provide the particle spacing. The peak position can be inferred in a rough approximation as the average center-to-center spacing of the nanoparticles,  $D$ , by the relation,  $D = 2\pi/q_p$ . For exact values of  $D$ , modeling the autocorrelation function should be included in the analysis.

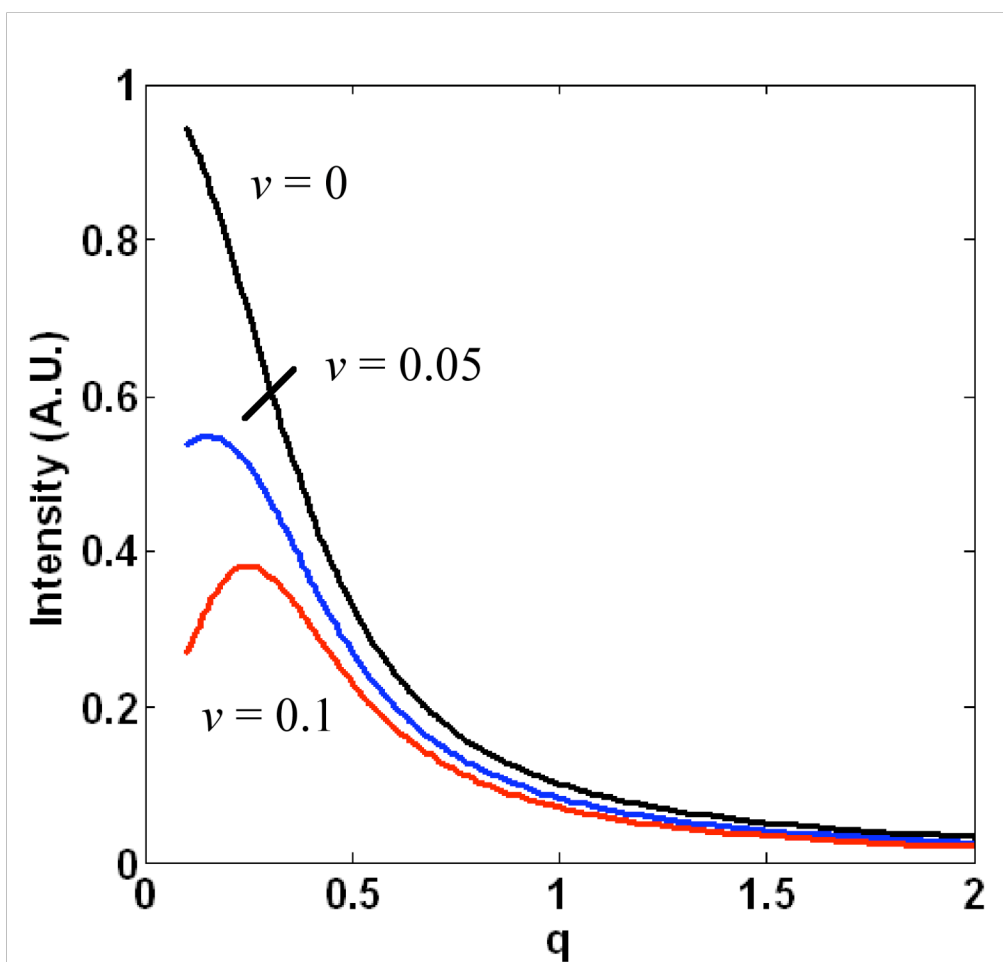


**Figure 3.4** Calculated SAXS for with interparticle interactions. As  $v$  (particle volume fraction) increases, the coherent scattering between the particles creates a peak at  $q = q_p$ . This peak can be inferred in a rough approximation as the average center-to-center spacing of the nanoparticles,  $D$ , by the relation,  $D = 2 \pi / q_p$ .

### 3.3.2 Grazing incidence small-angle X-ray scattering

The development of GISAXS began in the Materials Science & Engineering Department at Northwestern in the late 1980s where Levine *et al.* were responsible for building, operating, and reporting on the first GISAXS setup and experiments.<sup>17</sup> Since that time, the technique has grown significantly within the field and a number of quality theory papers have been written to account for the major differences between SAXS and GISAXS. The major reason for this is that the Born approximation no longer holds for the  $e$ -field intensity because the scattered  $e$ -field intensity from the surface is no longer small when compared to the incident field. This is due to working in grazing incidence geometry. In this geometry, the total external reflection effect leads to multiple scattering events and refraction effects. The amplitude of the form factor is rewritten to account for the four possible scattering events that could occur for a supported nanoparticle illuminated near or below the critical angle of the substrate. A schematic of the scattering events is given in Figure 3.5 originally from Lazzari.<sup>91</sup> This new description of the form factor originates with the distorted-wave Born approximation (DWBA) and the application to GISAXS has been developed by Rauscher *et al.* and Lazzari.<sup>93, 94</sup> The DWBA form factor is written:

$$\begin{aligned}
 F(\mathbf{q}_{\parallel}, k_z^i, k_z^f) &= F(\mathbf{q}_{\parallel}, k_z^f - k_z^i) + R_F(\alpha_i)F(\mathbf{q}_{\parallel}, k_z^f + k_z^i) + R_F(\alpha_f) \\
 &+ F(\mathbf{q}_{\parallel}, -k_z^f - k_z^i) + R_F(\alpha_i)R_F(\alpha_f)F(\mathbf{q}_{\parallel}, -k_z^f + k_z^i)
 \end{aligned} \tag{3.9}$$

where  $R_F$  is the reflectivity, the  $\mathbf{k}_z$  terms are the incident and scattered wave vectors normal to the surface, the  $\alpha$  terms are the incident and scattered angles normal to surface, and  $\mathbf{q}_{\parallel}$  is the in-plane scattering momentum transfer. The DWBA form factor may then be used in eq. 3.7 to calculate the GISAXS pattern directly where  $\mathbf{x}_i$  now locates the particle on the surface.

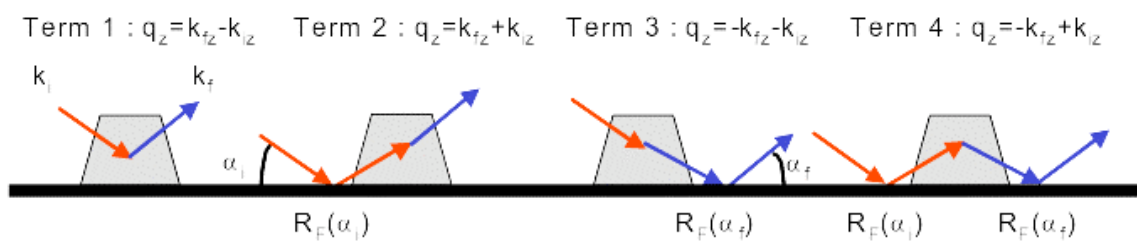


**Figure 3.5** Schematic of the distorted-wave Born approximation (DWBA). The DWBA modifies the GISAXS form factor to account for the dynamical effects related to grazing incidence including substrate reflectivity, refraction, and multiple scattering. Image taken from Ref. [91].



Eq 3.9 also shows that the momentum transfer vector needs to be broken into Cartesian components, which are depicted in Figure 3.6. The momentum transfer is written as:

$$\begin{aligned}
 q_x &= k_0[\cos(2\theta_f)\cos(\alpha_f) - \cos(\alpha_i)], \\
 q_y &= k_0 \sin(2\theta_f)\cos(\alpha_f), \\
 q_z &= k_0[\sin(\alpha_f) + \sin(\alpha_i)] \\
 q_{xy} &= q_{\parallel} = \sqrt{q_x^2 + q_y^2}
 \end{aligned} \tag{3.10}$$

GISAXS often exhibits the presence of densely packed particles that can be described with the interference function  $S(q)$ . However, nanoparticles supported on a surface rarely lend themselves to thermodynamic equilibrium and thus the interference function is modeled after some type of diffraction. The conventional approach is to represent  $S(q)$  with the use of the paracrystal model.<sup>91, 95</sup> The paracrystal model intrinsically incorporates spatial disorder of the system by smearing lattice point position as a function of distance from the origin. The one-dimensional paracrystal model is given by<sup>91</sup>:

$$S(q_{\parallel}) = \frac{1 - \phi^2}{1 + \phi^2 - 2 \cos(q_{\parallel}D)}, \text{ where } \phi = \exp\left(-\frac{q_{\parallel}^2 \omega^2}{2}\right). \tag{3.11}$$

The  $\omega/D$  ratio determines the disorder of the particle positions. Figure 3.7 shows a plot of the 1D paracrystal for a number of  $\omega/D$  ratios.

The treatment of the interference function of eq 3.11 is based on the local monodisperse approximation,<sup>96</sup> (LMA) which is equivalent to eq 3.8 except that the DWBA form factor is used. Under the LMA the nanoparticle size varies slowly across the surface such that the particles are evenly distributed with a uniform interparticle spacing. The LMA provides the best fit to most GISAXS data and is primarily employed in this project.

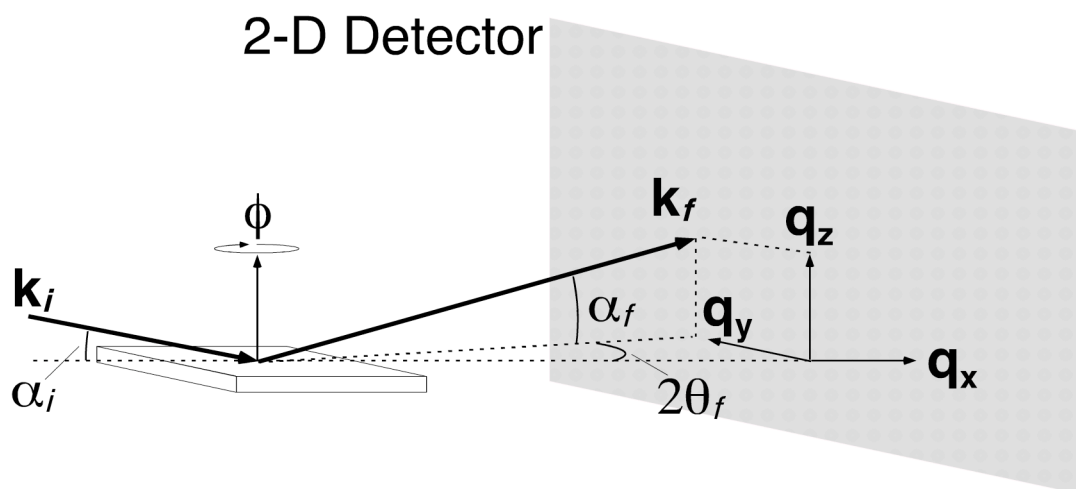


**Figure 3.6** Schematic of GISAXS geometry. The Cartesian components of the momentum transfer,  $\mathbf{q} = \mathbf{k}_f - \mathbf{k}_i$ , are determined by the various scattering angles:  $\alpha_i$ ,  $\alpha_f$  and  $2\theta_f$  using eq 3.10.

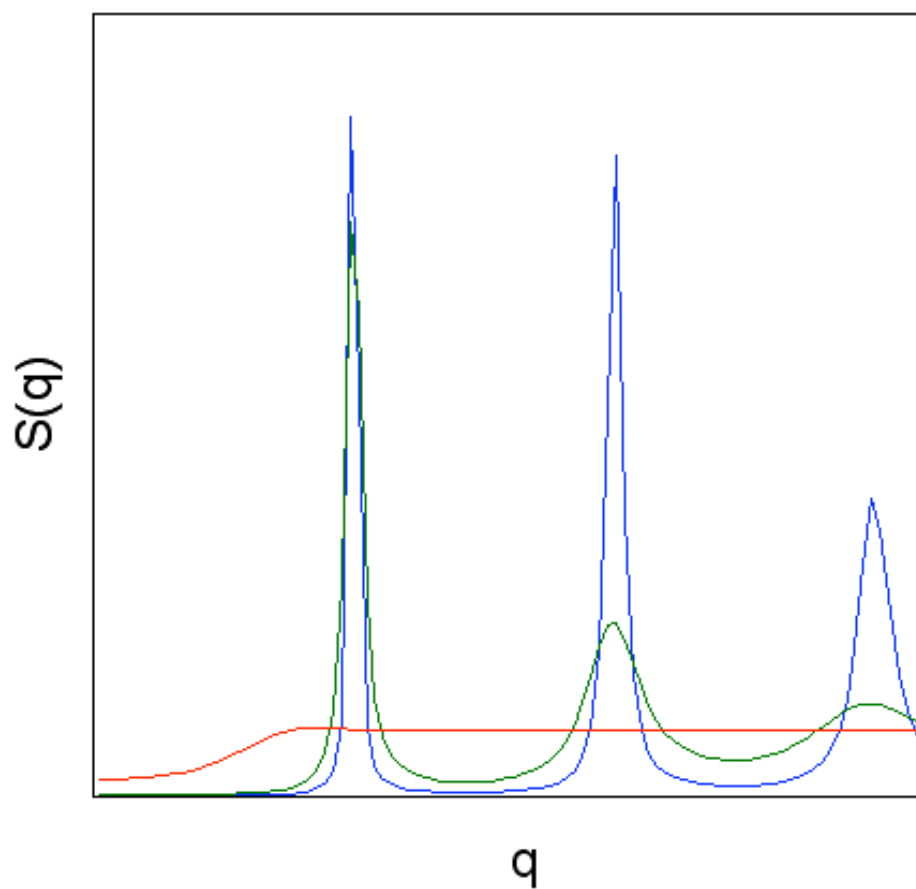


**Figure 3.7** The one-dimensional paracrystal interference function. The disorder in the lattice point is given by the  $\omega/D$  parameter where  $\omega/D = 0.01$  (blue),  $\omega/D = 0.1$  (green),  $\omega/D = 0.5$  (red).

Other treatments of interparticle spacing include the decoupling approximation<sup>91</sup> and size-spacing correlation approximation.<sup>93, 97</sup> The decoupling approximation<sup>89</sup> states that there is no correlation between the size of the scatter and the interparticle spacing. The interference function can then be based on the paracrystal model or some other function adequately calculating the effect of interparticle interactions. The size-spacing correlation approximation links the local area of nanoparticles to the size, such as a large nanoparticle surrounded by small nanoparticles resulting from nanoparticle coarsening. Both of these approximations were tested but did not exceed the fitting quality from the LMA.

### **3.3.3 X-ray fluorescence measurements**

XRF has featured prominently in this project as a means of determining the concentration of platinum atoms at the surface after deposition. The technique involves comparing the ratio of XRF yield for the adsorbate atom and the yield for a calibrated standard.

The concentration or coverage,  $\Theta$ , is calculated with:

$$\Theta = \frac{Y_{sample}}{Y_{standard}} \Theta_{standard} \quad (3.12)$$

If the standard and specimen are different materials and/or a different fluorescence line is selected, then a correction factor must be applied to eq 3.12 to account for the fluorescent cross-section and possibly transmission. The coverage may be reported in monolayers (ML) where one monolayer is equivalent to  $6.56 \times 10^{-14} \text{ cm}^{-2}$ , which is defined as the surface concentration of Sr or Ti ions for bulk SrTiO<sub>3</sub> (001). The fluorescence standards were calibrated using Rutherford backscattering spectroscopy performed by an analytical services laboratory.

### 3.3.4 X-ray absorption spectroscopy

X-ray absorption spectroscopy (XAS) provides a means to study the local chemical environment of the platinum nanoparticles including the oxidation state, coordination, and nearest neighbor bond lengths. In an XAS process, an incident photon with energy near the target element absorption edge creates a photoelectron from a core-level. The core-hole is filled by an X-ray fluorescence or an Auger electron process. The propagating photoelectron wave function is backscattered by the neighboring atoms. The backscattered wave functions interfere with subsequent photoelectron wave functions, which leads to oscillations in the measured absorbance cross section. The measured absorption spectra can be divided into the near edge and extended edge regions giving the X-ray absorption near edge structure (XANES) and extended edge X-ray absorption fine structure (EXAFS). The spectra are often plotted as the normalized absorption cross-section,  $\chi$ :

$$\chi(q(\epsilon)) = \frac{\mu_x(\epsilon) - \mu_0(\epsilon)}{\mu_0(\epsilon)}, \quad (3.13)$$

where  $\mu_0$  is the absorption coefficient of the isolated-free atom and  $\mu_x$  is the absorption coefficient for the atom of interest. The normalized cross-sections are plotted for the platinum  $L_3$  edge for platinum metal, platinum (II) oxide, and platinum (IV) oxide in Figure 3.8. The peak observed in the spectra is related to the absorption edge and is often referred to as the white line intensity. The absorption edge,  $E_0$ , is taken as the zero crossing of the second derivative of this peak region. The peak height of the absorption edge is related to the electron density of states for the orbital participating in the particular transition. Filling the orbitals with electrons leads to suppression of the peak as shown in Figure 3.8 between Pt metal and Pt oxide(s). The position of the absorption edge will be related to the chemical shift of the target atom. The XANES ‘region’ corresponds to the energy range about  $E_0 - 100$  eV to  $E_0 + 40$  eV, whereas the EXAFS region corresponds to the energy range at  $E_0 + 40$  eV to  $E_0 + 1500$  eV.

The lower energy XANES signal results from multiple scattering events from the target element’s nearest neighbors. Consequently, XANES provides information of the oxidation state and chemical coordination for the material. The XANES region includes the region just before the absorption edge (pre-edge transitions), the edge position and height, and the structure just after the white line peak. The analysis is typically performed empirically using comparison to standards, as there is no discrete mathematical relationship available for simple modeling. The near edge region is often fit with a linear combination of standards to determine the fraction of a given chemical state in the specimen of interest.

The EXAFS is measured in the region marked in Figure 3.8 and results from single scattering events from the outgoing and backscattered photoelectron wave functions. The Fourier transform of eq 3.13 enables the extraction of the pair distribution of the atomic species

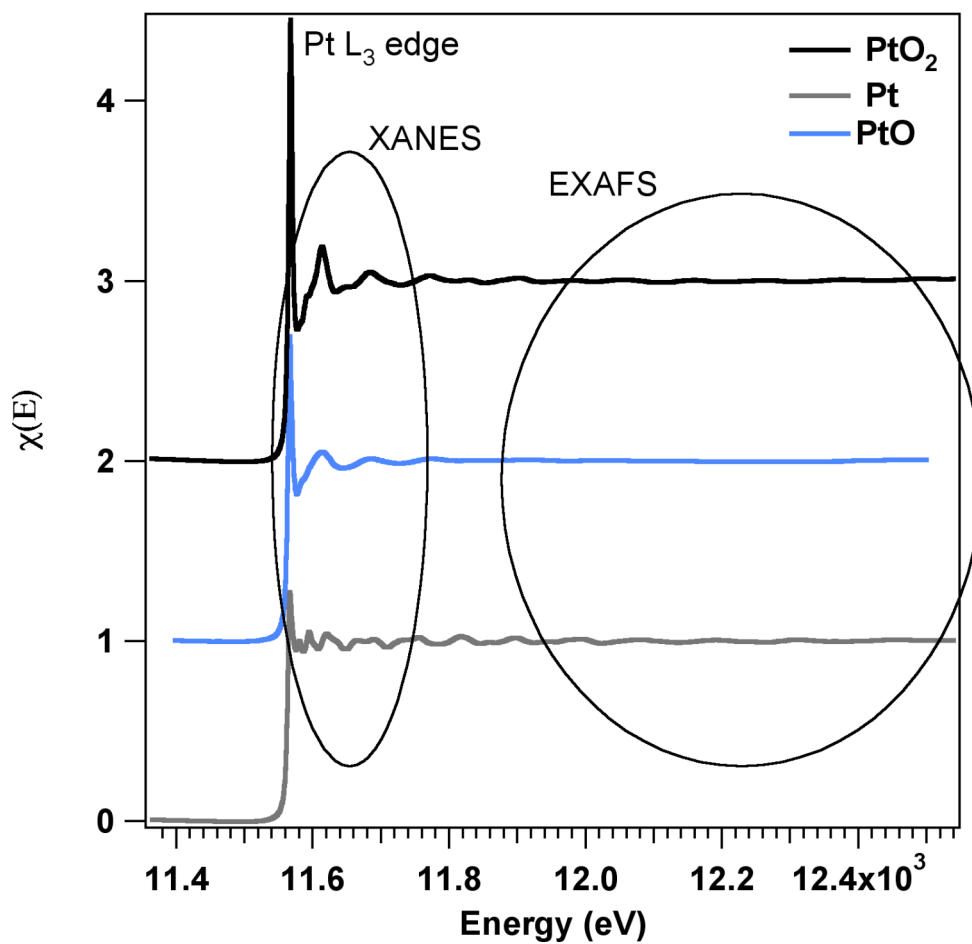


**Figure 3.8** X-ray absorption cross-section,  $\chi(E)$ . The spectra measured near the Pt L<sub>3</sub> edge for Pt metal, PtO, and PtO<sub>2</sub>. The near edge region is the basis for XANES that gives oxidation state and chemical coordination. The EXAFS region provides information on the pair distribution for the atomic species within the system. These spectra were collected at DND-CAT 5BM-D.

in the system. The Fourier transform may be modeled using the following equation:

$$\chi(R) = \sum_j \frac{N_j S_0^2 f(k) \exp(-2k^2 \sigma_j^2)}{k R_j^2} \sin[2k R_j + \delta_j(k)], \quad (3.14)$$

where  $R$  is the nearest neighbor distance,  $k$  is the wave vector,  $j$  denotes the coordination shell,  $N$  is the coordination number,  $S_0^2$  is the amplitude reduction factor,  $f(k)$  is the amplitude function,  $\sigma$  is the Debye-Waller factor, and  $\delta(k)$  is the phase function. Figure 3.9 gives the Fourier transform for the EXAFS data from Fig. 3.8. The Pt – O bond is 1.6 Å whereas the Pt – Pt bond is 2.5 Å. The EXAFS can also be calculated with a quantum mechanical treatment of the X-ray transitions<sup>98</sup> and a number of free software programs exist that employ this to model the data. The details of these calculations are beyond the scope of this dissertation and not covered here.



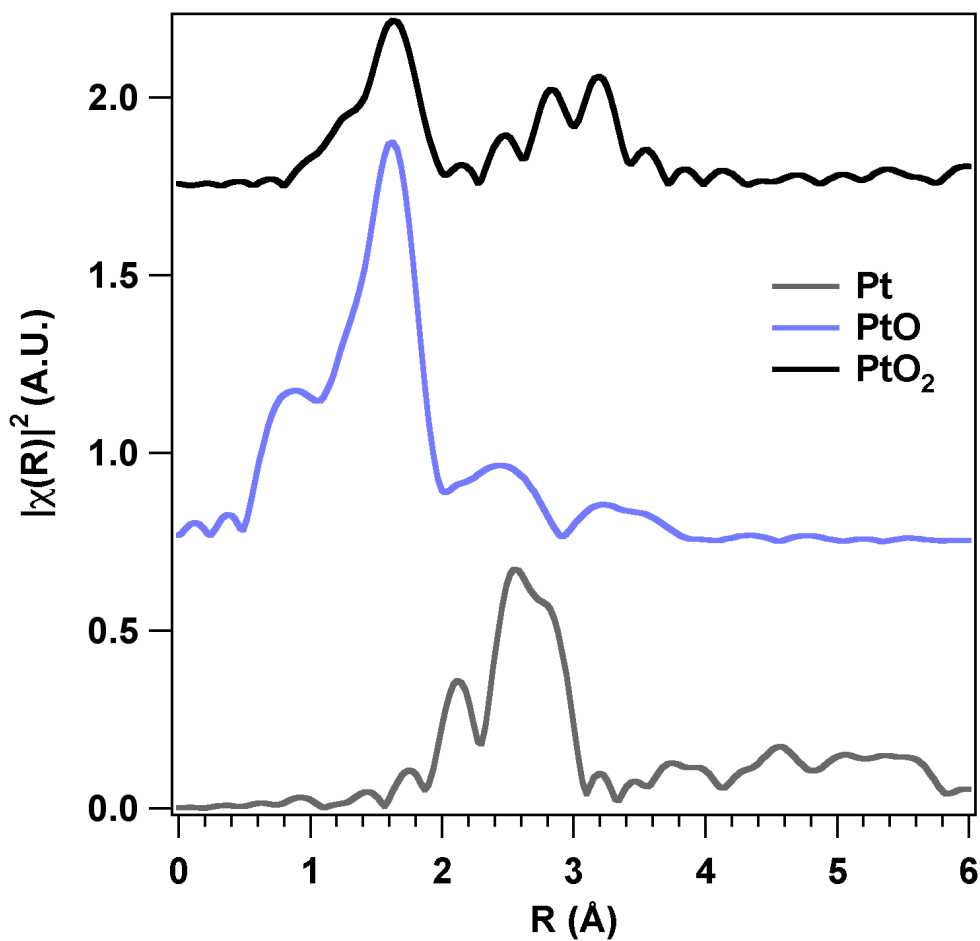


**Figure 3.9** Fourier transforms of the EXAFS data from Figure 3.8 (offset for clarity). The peaks provide the average distances for the coordination shells for a given element, which are a measure of the bond distance. The peak near 1.6 Å corresponds to the Pt – O bond where the nearest neighbor Pt – Pt bond is 2.5 Å.

## Chapter 4: PVD platinum nanoparticle aggregation on SrTiO<sub>3</sub> (001)

### 4.1 Platinum nanoparticles on SrTiO<sub>3</sub> (001) via physical vapor deposition

This chapter discusses the formation of platinum nanoparticles on SrTiO<sub>3</sub> (001) within an ultra-high vacuum chamber after evaporating  $\sim 1$  monolayer (ML) of platinum onto room temperature substrates. The substrates then receive one of three different post-deposition annealing treatments. This chapter combines AFM to directly image platinum nanoparticles deposited onto SrTiO<sub>3</sub> (001) and a suite of X-ray techniques to determine additional structural information of the system. The combination of AFM and GISAXS was motivated in part after the samples were studied with the X-ray standing wave (XSW) technique<sup>88, 99, 100</sup> in an effort to investigate the early stages of epitaxial ordering through heat treatment, which was in line with previous studies focused on the epitaxy of relatively thick ( $\sim 20$  nm) Pt films on SrTiO<sub>3</sub> (001).<sup>63, 64, 66</sup> GISAXS is employed to potentially identify such structures in the early stages of growth. In addition to supporting the AFM results, the GISAXS gives additional information at smaller length scales, beyond the lateral resolution of the AFM conducted in this study. The resolution gained from GISAXS provides the ability to determine if the nanoparticles detected at longer-length scales are some type of aggregate of smaller nanoparticles such as those observed for the case of cluster deposited platinum nanoparticles<sup>8-10</sup> or the highly dendritic aggregates observed from a variety of vapor deposition conditions<sup>101-103</sup>. This chapter demonstrates the need for combining scanning probe and X-ray characterization when studying nanoparticle aggregation in the early stages of thin film growth.

## 4.2 Platinum deposition and post deposition annealing

SrTiO<sub>3</sub> (001) substrates (10x10x1 mm) were obtained from MTI Corp. (Richmond, California). After preparing the substrates with a BHF etch and oxygen anneal as described in Chapter 2, they were immediately mounted on a tantalum sample plate using spot-welded tantalum wire and loaded into an ultra-high vacuum (UHV) chamber. The UHV chamber was maintained at a pressure of 10<sup>-9</sup> to 10<sup>-10</sup> Torr and equipped with LEED (Omicron), Auger electron spectroscopy (Physical Electronics), and an electron beam effusion source (Omicron). Prior to platinum deposition, the substrates were annealed at 925°C for 30 minutes in the UHV chamber using an indirect tungsten wire heater placed behind the sample. During annealing, the substrate temperature was monitored with an optical pyrometer. After UHV annealing, LEED measurements indicated the continued presence of the  $\sqrt{13} \times \sqrt{13} R33.7^\circ$  surface reconstruction and Auger electron spectroscopy revealed a reduction of the carbon peak to an undetectable limit. Platinum electron-beam deposition of a 1.5 mm diameter Pt rod occurred in a side chamber pumped by a turbomolecular pump where the pressure did not exceed 10<sup>-9</sup> Torr. The platinum source to sample distance was 80 mm and the platinum temperature at deposition was measured to be ~1750°C. Based on these parameters, the average evaporant flux is calculated<sup>104</sup> to be  $1.4 \times 10^{13} \text{ cm}^{-2} \text{ s}^{-1}$ . Platinum was deposited for 10 minutes on each sample. Following Pt deposition, samples were annealed for 10 minutes at either 600°C or 900°C in the main UHV chamber. One sample treatment included no annealing.

## 4.3 Measurement of the PVD platinum on SrTiO<sub>3</sub> (001)

AFM images in Figure 4.1 show that nanoparticles exist for all the cases of post-deposition annealing.

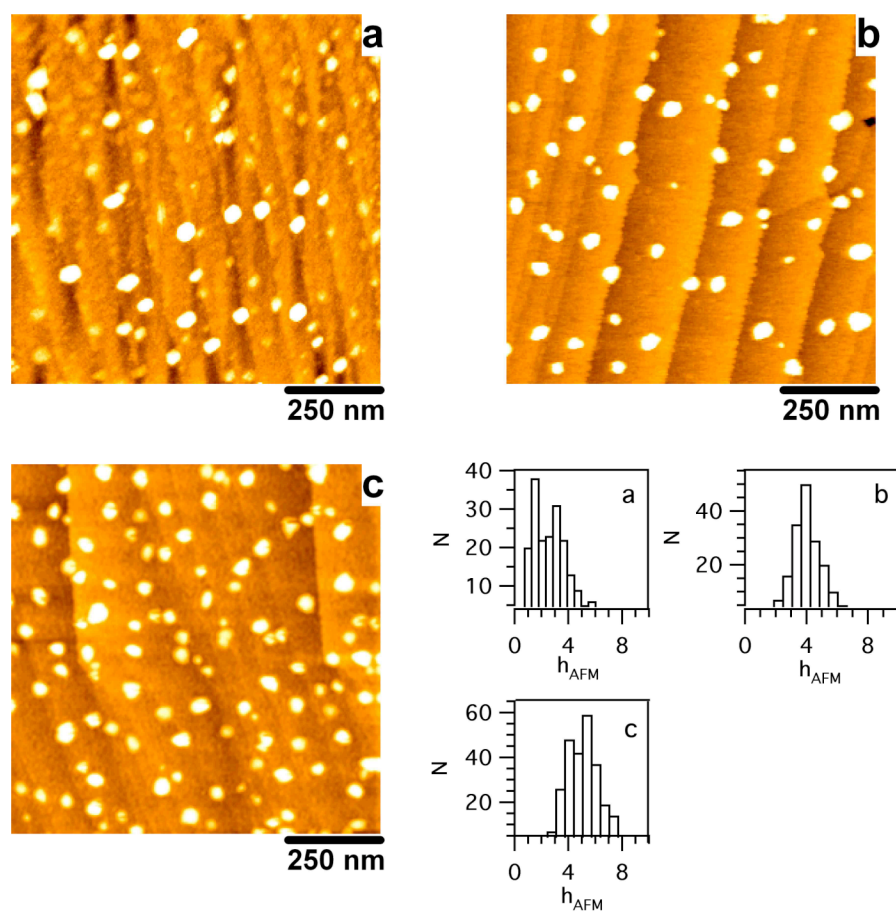


**Figure 4.1** AFM images following Pt deposition and the associated histograms of the height measurements. (a) 1.7 ML Pt/SrTiO<sub>3</sub> unannealed. (b) 1.0 ML Pt/SrTiO<sub>3</sub> annealed at 600°C. (c) 1.5 ML Pt/SrTiO<sub>3</sub> annealed at 900°C.

Sample	$h_A$ (nm)	$\sigma_h$ (nm)	$D_A$ (nm)	$R_A$ (nm)
1.5 ML / 900°C	4.6	1.1	86	8.0
1.0 ML / 600°C	3.7	1.0	140	12
1.7 ML / none	2.4	1.2	110	15

**Table 4.1** Measured Pt parameters from combined AFM and XRF analysis. The Pt coverage was determined by measuring the Pt  $L\alpha$  XRF yield and is reported here in units of monolayers (ML). The UHV annealing treatment per sample is also included. The average height,  $h_A$ , and interparticle distance,  $D_A$ , were measured directly with AFM. The standard deviation of the height is given by  $\sigma_h$ . The average lateral dimension,  $R_A$ , is calculated from the AFM and XRF data using eq 4.1.

Sample	$R_g$ (nm)	$h_X$ (nm)	$R_X$ (nm)	$\sigma_R$ (nm)	$D_X$ (nm)
1.5 ML / 900°C	18	1.9	1.8	0.14	4.2
1.0 ML / 600°C	21	1.7	1.0	0.17	3.2
1.7 ML / none	14	1.5	0.9	0.03	2.8

**Table 4.2** Nanoparticle parameters extracted from GISAXS analysis. The Guinier analysis in the  $q_{xy}$  data shown in Figure 4.5 gave the radius of gyration,  $R_g$ . The data from Figure 4.6 were fit with a distorted-wave Born approximation form factor under the local monodisperse approximation (LMA). In particular, the nanoparticle shape was assumed to be a cylinder with radius,  $R_X$ , and height,  $h_X$ . The height distribution is coupled to the radius distribution, which is given by  $\sigma_R$ . The interparticle spacing,  $D_X$ , is defined as the center-to-center distance of the nanoparticles.

Table 4.1 presents the extracted mean nanoparticle height ( $h_A$ ), the standard deviation of the height measurements ( $\sigma_h$ ) and average center-to-center interparticle spacing ( $D_A$ ) from the AFM data. These data originate from a statistically significant number of AFM images at several different points across the entire sample surface. The images in Figure 4.1 give the best representation for the various imaging conditions. No specific correlation between nanoparticle location and the morphology of the substrate (step edges) occurs and scanning the AFM tip showed no effect of nanoparticle manipulation or perturbation. The heights of the nanoparticles range from 2.4 nm to 4.6 nm and follow a trend where larger nanoparticles develop as the annealing temperature increases. The average interparticle spacing varies between 85 nm and 140 nm. Fast Fourier transforms of the AFM images indicated there was no substantial ordering of the nanoparticles. The AFM images also show clear atomic steps with no indication of a film or significant roughening. Another interesting feature from the AFM data is that the annealing treatments do not lead to a significant change in particle morphology and size.

The XRF yield of Pt after deposition was performed at the APS 12ID-D beam line at a photon energy of 15 keV. The surface coverage will be discussed in units of monolayers (ML), where 1 ML is  $6.56 \times 10^{14} \text{ cm}^{-2}$  and is equivalent to the Sr or Ti ion areal density in a bulk  $\text{SrTiO}_3$  (001) atomic plane. The surface coverage of Pt ranges from 1.0 to 1.7 ML and is reported in Table 4.1. The sticking coefficient of platinum calculated to be 0.1 and is the ratio of the average measured coverage ( $1.4 \text{ ML} = 9.2 \times 10^{14} \text{ cm}^{-2}$ ) to the deposition flux and time ( $1.4 \times 10^{13} \text{ cm}^{-2} \text{ s}^{-1}$ ; 600 s).

Although the lateral dimensions of the nanoparticles cannot be directly measured from AFM data due to tip convolution effects, combining the XRF surface coverage measurement

with the AFM height and interparticle spacing measurements can provide an estimation of the lateral dimensions of the Pt nanoclusters. Assuming a cylindrical nanoparticle geometry, the following equation calculates the average nanoparticle radius ( $R_A$ ):

$$R_A = \left( \frac{\Theta}{\pi N_b N_a h_A} \right)^{1/2}, \quad (4.1)$$

where  $N_b = 4a^{-3}$  is the bulk atomic density of Pt,  $a$  is the Pt lattice constant,  $N_a = (D_A)^{-2}$  is the number of particles per area measured with AFM, and  $\Theta$  is the average number of Pt atoms per area from the XRF surface coverage. Table 4.1 shows the calculated results with the nanoparticle radius ranging from 8 to 15 nm.

X-ray standing wave measurements were conducted at the Advanced Photon Source (APS) 5ID-C beam line. The incident photons with  $E_\gamma = 15.00$  keV were selected with the beam line Si (111) monochromator and then further conditioned with a two-bounce Si (220) channel-cut post monochromator to nondispersively match the SrTiO<sub>3</sub> (002) substrate Bragg condition. The 5ID-C setup is described in detail elsewhere.<sup>105</sup> The Pt L $\alpha$  fluorescence yield was monitored with an energy dispersive, solid-state X-ray detector while scanning in incident angle  $\theta$  through the SrTiO<sub>3</sub> (002) Bragg reflection. The (002) XSW results for all three samples showed a coherent fraction of  $f_{002} \sim 0$ . This is consistent with a platinum distribution that is uncorrelated (i.e., nonepitaxial) to the SrTiO<sub>3</sub> lattice. The XSW results do not imply that the Pt itself was disordered. Figure 4.2 shows the typical XSW data for Pt/SrTiO<sub>3</sub> (001) with a coherent fraction of  $\sim 0$ .

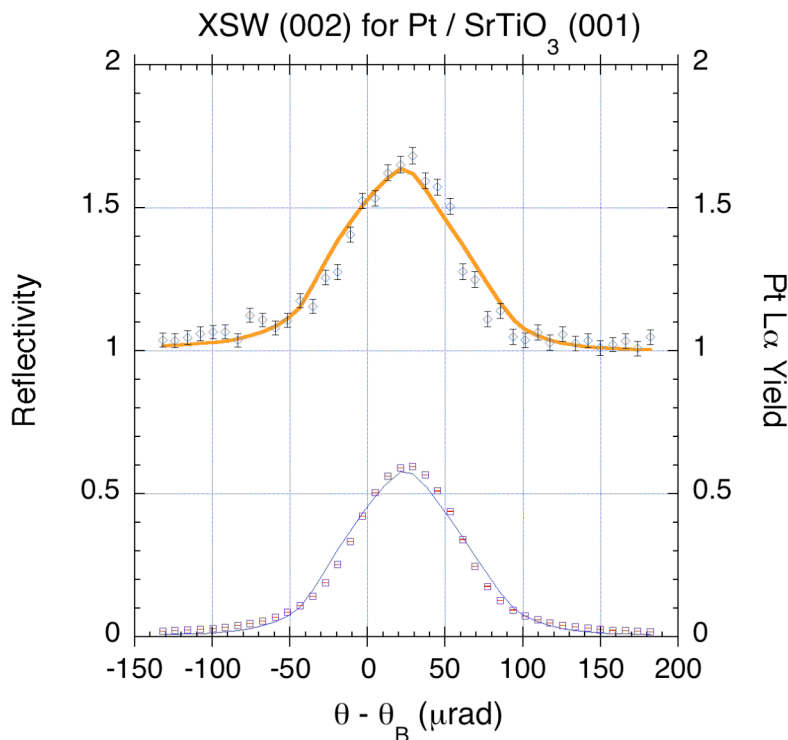


**Figure 4.2** XSW data for Pt / SrTiO<sub>3</sub> (001). The reflectivity of the SrTiO<sub>3</sub> (002) Bragg reflection is shown in blue on the bottom. The normalized Pt L $\alpha$  X-ray fluorescence yield and fit is shown in black and orange on the top. The fitted coherent fraction is  $\sim 0$ , which indicates the platinum distribution is uncorrelated with the SrTiO<sub>3</sub> lattice. This result may be appreciated qualitatively in that the L $\alpha$  fluorescence yield line shape is nearly identical to the reflectivity with an offset of 1. The XSW data was collected at the APS 5ID-C station using a Si(220) channel cut post-monochromator and at an incident photon energy of 15.00 keV.



GISAXS measurements were performed at the APS using the 12ID-C beam line. The scattering was conducted with incident photon energies of 11.50 keV and 8.00 keV using a MAR 165 CCD detector. The GISAXS instrumental setup available for this experiment could not accommodate a scattering range to capture all the scattering features from the nanoparticles observed with AFM. Scattered X-rays were collected after passing through an evacuated flight path with a detector-to-sample distance of 2 m and 1 m for  $E_\gamma=11.5$  keV and 2.1 m for  $E_\gamma= 8$  keV. For the setup at 11.5 keV, the horizontal  $q$  range was  $0.025 - 0.50 \text{ \AA}^{-1}$  and the vertical  $q$  limit was  $0.56 \text{ \AA}^{-1}$ . For 8.00 keV, the horizontal  $q$  range was  $0.004 - 0.17 \text{ \AA}^{-1}$  and the vertical  $q$  limit was  $0.17 \text{ \AA}^{-1}$ . However, the GISAXS setup did enable the resolution to exceed the nominal 10 nm limit of AFM to a resolution of  $\sim 1$  nm. Figure 4.3 contains the scattering data from a blank SrTiO<sub>3</sub> substrate that was chemically etched and oxygen annealed. Figure 4.4 shows the measured GISAXS data for the different sample cases. In the horizontal direction, the intensity lobe is offset from the origin where the lobe center forms a peak at  $q_{xy} = q_p$ . This feature in the scattering is related to the Fourier transform of the autocorrelation function for the interparticle spacing of the nanoparticles and indicates a discrete nanoparticle correlation as opposed to dendritic structures that show fractal behavior.<sup>101</sup> The  $q_p$  value gives the approximate<sup>91, 106</sup> interparticle spacing,  $D_X$ , by  $D_X = 2\pi/q_p$ . Line cuts of intensity along  $q_z$  and  $q_{xy}$  were extracted for fitting from these CCD images. GISAXS data collected at several different values of the substrate azimuthal angle  $\phi$  showed no changes in the intensity lobes; thus, the in-plane autocorrelation function had no particular orientational dependence with respect to the substrate. Any faceting of the nanoparticles correlated to the substrate is thus not detected with this GISAXS data.

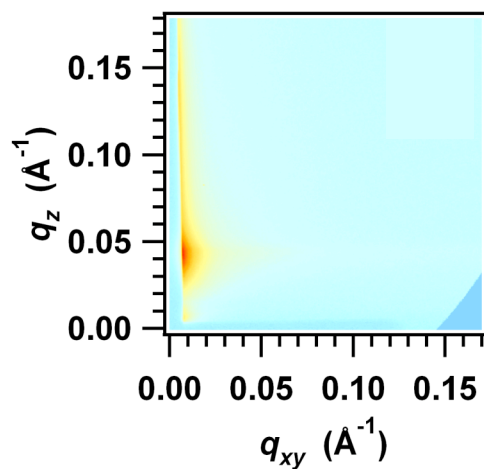


**Figure 4.3** GISAXS measurement for a blank SrTiO<sub>3</sub> substrate after etching and annealing at  $E_\gamma = 11.5$  keV and the sample to detector distance is 2 m. Data collected at the APS, 12ID-C.

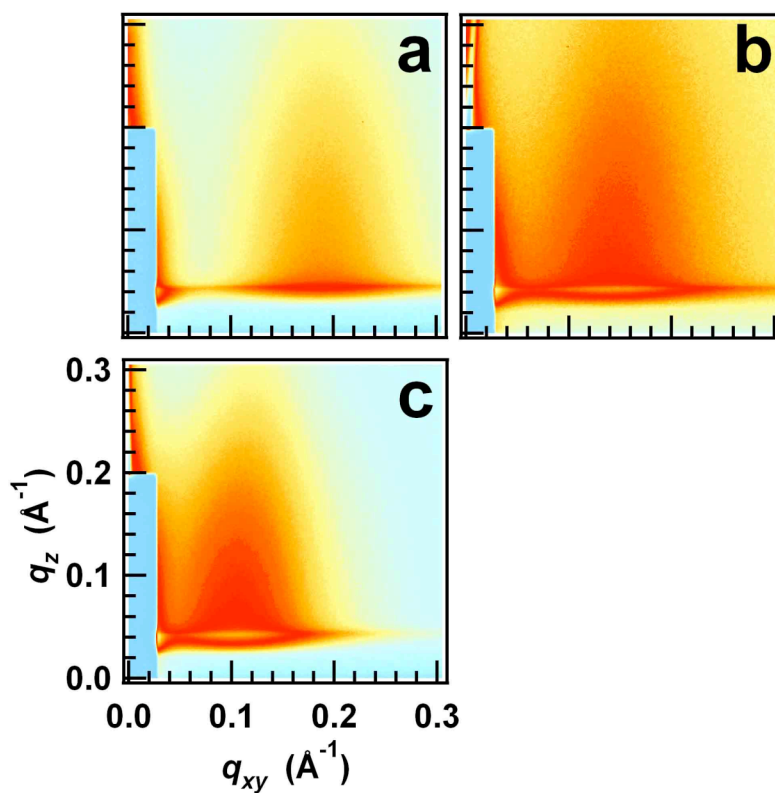


**Figure 4.4** Experimental 2D GISAXS intensity for (a) 1.7 ML Pt/SrTiO<sub>3</sub> unannealed, (b) 1.0 ML Pt/SrTiO<sub>3</sub> annealed at 600°C, and (c) 1.5 ML Pt/SrTiO<sub>3</sub> annealed at 900°C. Data collected at the APS, 12ID-C.

The intensity from the blank substrate is significantly lower than the Pt coated substrates and shows no intensity lobes at higher  $q_{xy}$  values. Therefore the intensity lobes are not due to Pt decorating the step edges or Pt particles lining up along step-edges. The lack of the GISAXS dependence on the  $\phi$  results are consistent with Figure 4.1 AFM images that show nanoclusters laterally uncorrelated with step edges.

The GISAXS analysis begins with applying the Guinier approximation<sup>89</sup> to the smallest- $q_{xy}$  region to determine the lateral radius of gyration,  $R_g$ . The respective  $R_g$  values for the unannealed, 600°C anneal and 900°C anneal were 14 nm, 21 nm, and 18 nm. These values are included in Table 4.2 and are reasonable in terms of the order of magnitude when compared with the  $R_A$  values in Table 4.1. Figure 4.5 shows the line cuts ( $q_z \sim 0.04 \text{ \AA}^{-1}$ ) used to determine the Guinier results. The  $R_g$  value determined for a blank SrTiO<sub>3</sub> substrate was 41 nm, which is related to the average terrace width. Substrate scattering in the vertical direction prevented a similar application of the Guinier analysis to measure the vertical dimension, however this parameter was extracted from the GISAXS fitting of the higher  $q$  data.

The GISAXS fitting over the extended range of the pattern was performed using the IsGISAXS<sup>91</sup> program with a theory framework including the distorted-wave Born approximation<sup>91, 94, 107-109</sup> (DWBA) for a cylinder form factor and the local monodisperse approximation<sup>96</sup> (LMA) with 1-D paracrystal model<sup>91, 95</sup> for an interference function representing the interparticle spacing distribution. Figure 4.6 shows the fitting results (solid line) for  $q_z$  and  $q_{xy}$  line cuts, where the cuts were taken along the Yoneda wing ( $q_z \sim 0.04 \text{ \AA}^{-1}$ ) for  $q_{xy}$ , and the  $q_z$  cuts were taken along  $q_{xy} = 0.11 \text{ \AA}^{-1}$  (1.5 ML),  $0.15 \text{ \AA}^{-1}$  (1.0 ML), and  $0.19 \text{ \AA}^{-1}$  (1.7 ML).

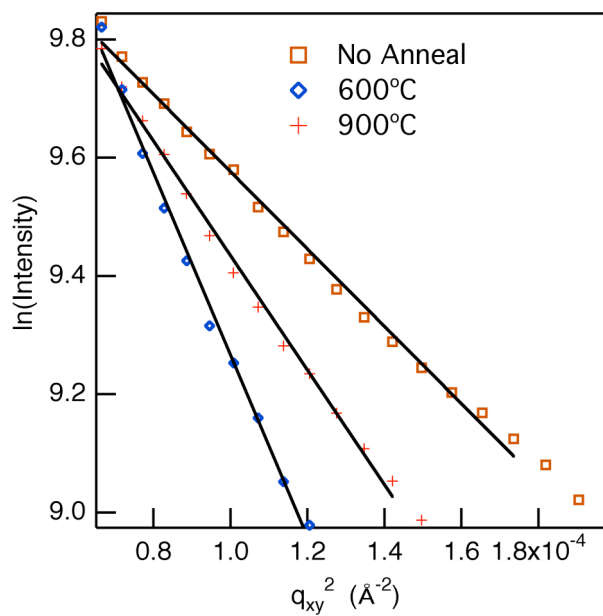


**Figure 4.5** Line cuts in a Guinier plot of the  $q_{xy}$  data for the smallest  $q$  range. The curves are offset for clarity. Guinier analysis was performed on these data to extract the lateral  $R_g$  value. Line cuts taken from 2D patterns at the Yoneda wing ( $q_z \sim 0.04 \text{\AA}^{-1}$ ).

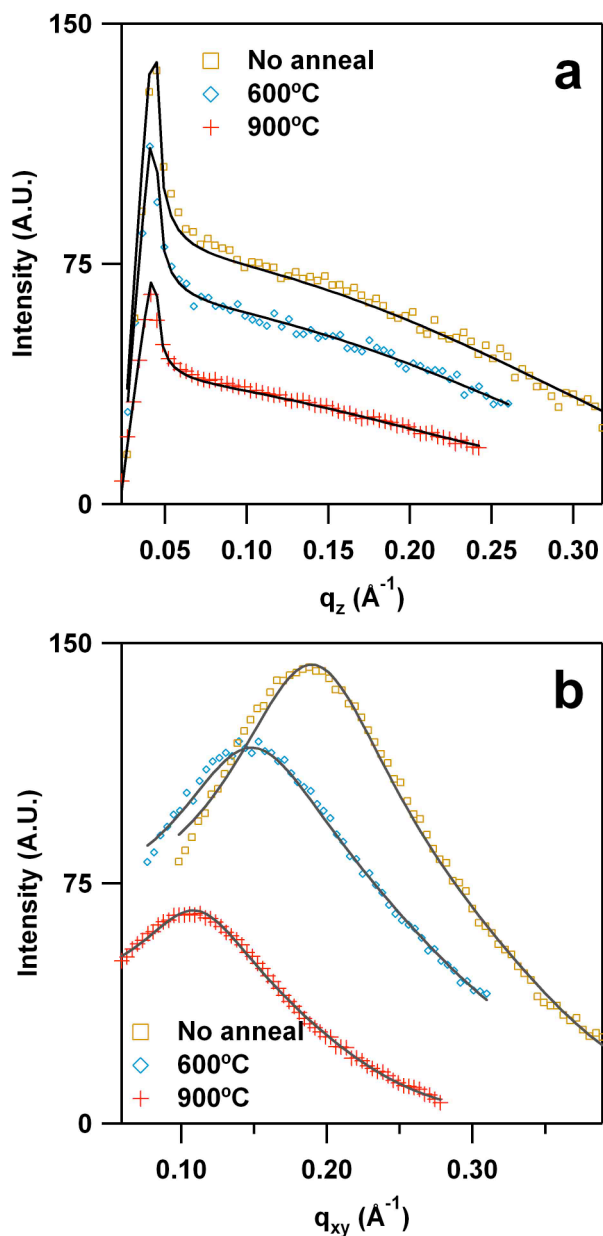


**Figure 4.6** Line cuts through the Figure 4.4 GISAXS data and fits along (a)  $q_z$  and (b)  $q_{xy}$  directions. These data were fit with a distorted-wave Born approximation cylinder form factor and the local monodisperse approximation. The  $q_{xy}$  line cuts were taken at  $q_z \sim 0.04 \text{ \AA}^{-1}$  and the  $q_z$  cuts were taken along  $q_{xy} = 0.11 \text{ \AA}^{-1}$  (1.5 ML),  $0.15 \text{ \AA}^{-1}$  (1.0 ML), and  $0.19 \text{ \AA}^{-1}$  (1.7 ML).

Attempts were made to fit alternative nanoparticle shapes, but the best fitting resulted from a cylinder model. Using this model, the nanoparticle height ( $h_X$ ) was 1.7 – 1.9 nm, the nanoparticle radius ( $R_X$ ) was 0.9 – 1.8 nm, and the interparticle spacing ( $D_X$ ) was 2.8 – 4.2 nm as delineated in Table 4.2. The nanoparticle radius distributions are Gaussian functions of width  $\sigma_R$  centered on  $h_X$  with the height distribution coupled to the radius distribution.

#### 4.4 Platinum nanoparticle aggregation on SrTiO<sub>3</sub>

The formation of nanoparticles shown in the AFM images and Guinier analysis was not all together expected. One may have expected the  $\sim 2$  ML of platinum to uniformly coat the surface and evolve by some well-known growth and coarsening behavior as the post-deposition annealing proceeded. Furthermore, the nanoparticles did not exhibit any observable correlated epitaxy and faceting. The fact that the resolution of GISAXS and AFM do not completely overlap provides a means for understanding what morphology could lead to these results. The key lies in the ability of the AFM to easily image at longer length scales than GISAXS, while GISAXS can support the AFM measurements of nanoparticle size through Guinier analysis and provide information on length scales below the nominal 10 nm AFM tip radius of curvature. Combining the two along with the XRF significantly improves the ability to understand the distribution of platinum on the surface. Summarizing the Guinier analysis and AFM/XRF, the  $R_g$  and the  $R_A$  listed in Table 4.1 and 4.2 are consistent with the order of magnitude of lateral sizes of the nanoparticles shown in the AFM images of Figure 4.1. The AFM, XRF, and the Guinier analysis at small  $q_{xy}$  suggest that the majority of the platinum is contained within nanoparticles observed directly by AFM and that minimal Pt residue exists elsewhere on the surface. Since the XRF fixes the total platinum coverage to  $\sim 2$  ML, it appears that the nanoparticles detected by

AFM are comprised of smaller nanoparticles that have aggregated together. Otherwise, the GISAXS data analyzed at higher  $q_{xy}$  would nearly constitute a film of  $\sim 2$  nm tall nanoparticles covering the surface. A morphology of this nature would have significantly more platinum than the  $\sim 2$  monolayers measured by XRF. AFM lacks the resolution to detect the smaller individual nanoparticles, but the GISAXS intensity lobe at higher  $q_{xy}$  indicates a model-independent and well-defined interaction distance of nanoparticles. As described above, the LMA provides the physical model to describe the interaction distance and particle scattering as it gives the best fitted results with reduced chi squared values of  $\sim 0.1$ . Alternative physical models available include the decoupling approximation<sup>89</sup> and the size-spacing-correlation approximation<sup>97</sup>, but neither of these proved effective. The LMA may be conceptually described as uniformly spaced nanoparticles of a narrow size distribution that blanket the surface. Figure 4.7 shows a representation of the LMA and the model where the nanoparticles are aggregated together. For interpretation purposes, consider the total intensity covering two length-scales as:

$$I(q) = I_{Cluster}(q) + I_{LMA}(q) \quad (4.2)$$

where  $I_{Cluster}(q)$  gives the collective scattering from the aggregated nanoparticles. Because of their size  $I_{Cluster}(q)$  is located near  $q_{xy} = 0$  and is best treated with the model-independent Guinier approximation<sup>89</sup> as described above. The  $I_{LMA}(q)$  gives the intensity from the smaller particles at higher  $q_{xy}$  that constitutes a length regime below the resolution of the AFM. In terms of the lateral dimensions, the Guinier analysis and the AFM images also confirm that annealing does not lead to significant changes in the order of magnitude of the particle size and spacing.

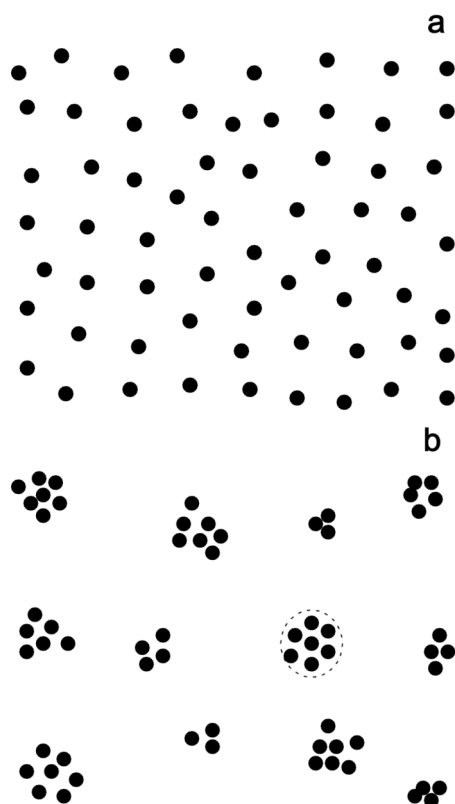


**Figure 4.7** Diagrams of the particle spacing in (a) the local monodisperse approximation and (b) the clustered nanoparticle model. The scattering from structures in (b) would have components representing both the small nanoparticles and the nanoparticle clusters according to eq 4.2.

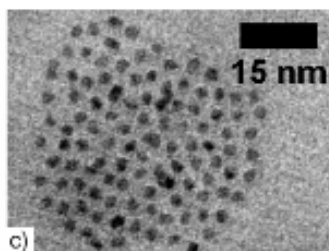


**Figure 4.8** TEM image of a platinum nanoparticle aggregate from Ref. [10]. This image is representative of the model drawn in Figure 4.7 and establishes the interesting morphology platinum nanoparticles may exhibit.



From comparing the height measurements from Tables 4.1 and 4.2, there is good agreement with the two techniques when keeping in mind that the AFM will measure the tallest height feature of a nanoparticle and that GISAXS will measure the average height. The height in both cases increases with increasing temperature in post-deposition annealing treatments. Since lateral dimensions and spacing do not change significantly, the system should not be treated with traditional growth and coarsening theory, and consequently an alternative mechanism can apply such as the model with some form of aggregation without coalescence or sintering.

The physical observation of platinum forming collections of nanoparticle agglomerates without sintering or coalescence was demonstrated in two separate studies<sup>8, 10</sup> using specially designed cluster beam deposition sources<sup>110, 111</sup>. In both cases, TEM images clearly show 1-3 nm Pt nanoparticles aggregating without coalescence and having a well-defined spacing. Figure 4.8 shows an example of a nanocluster taken from Ref. [10]. The total cluster size seems to depend on the coverage, but ranges from 10 nm to over 50 nm and the clusters appear to be somewhat randomly spaced in the range of 50-100 nm. Both studies also show comparisons of the platinum nanoparticles to nanoparticles of indium [8] and gold [10] where both the In and Au nanoparticles undergo coalescence. Even co-depositing In with Pt or Au with Pt does not lead to platinum nanoparticle coalescence, yet the platinum nanoparticles show an extremely high mobility at room temperature. The phenomenon was shown even earlier with alloy FePt nanoparticles which were also prepared with cluster beam deposition.<sup>9</sup> Furthermore, Tainoff *et al.* [10] deposited the pure Pt nanoparticles in UHV with and without size selection, which only added polydispersity to the clusters but did not lead to coalescence. They rule out a contamination effect preventing coalescence and propose that the platinum nanoparticles possess

a repulsive interaction due to electronic effects and substrate deformation.

In comparison between the data here and the results from [8,10], there is a strong resemblance. The size-selected nanoparticles from [8,10] ranged from 1.6 – 2.3 nm in size with center-to-center spacing of 2.5 – 5 nm, which agree very well to the Table 4.2 values. The overall size and spacing of the size-selected nanoparticle aggregates agree on the order of magnitude with these data. Also, Tainoff *et al.* mentions that the nanoparticles are stable over the course of many months, which is also the case for the samples prepared here. The structures shown in the TEM images from [8-10] would give comparable AFM and GISAXS data to what observed during this project. The platinum nanoparticles for the cluster deposited studies are in essence the same as the schematic in Figure 4.7 (b) where the Pt nanoparticles are gathered into small groups. These are compelling reasons to conclude that indeed what is observed here is similar to the phenomena from [8-10] only with a different characterization methodology.

It should be clearly understood that significant differences in deposition conditions between these cases. The formation of the structures observed in this study would presumably come from heterogeneous nucleation on the effusion cell orifice as described by Knauer<sup>112</sup> or through the dynamics of the platinum atoms upon impact with the surface. Such diffusive aggregation mechanisms have been modeled under the diffusion limited aggregation formalism, which was first used to describe the dendritic aggregation of 4 nm gold nanoparticles from evaporation and has since been applied to aggregation for a variety of experimental conditions.<sup>103</sup> Given the mobility of the platinum nanoparticles at room temperature and the resistance they show to coalescence, the morphology observed in [8-10] and what is observed here should be attributed to some physical mechanism that is independent of the manner in which the structure

was prepared. The important issue at hand rests in the fact that this phenomenon seems to be specific to platinum and consequently is manifested in this situation. Moreover, the results from this project suggest the behavior is transferable between substrates and thermally stable. As a consequence it is hopeful that this work motivates additional studies into the processing dynamics of similar platinum nanoparticle clusters.

Late developments in the project have provided additional information regarding the aggregation of the Pt nanoparticles. Figure 4.9 shows high-resolution SEM images of the 900°C annealed sample [NU, EPIC SEM instruments (a) Hitachi S-4800 SEM; (b) FEI Helios FIB-SEM]. The image was taken without any special SEM surface treatment. The images show what appears to be nanoparticle aggregates consistent with the size and spacing determined in AFM and GISAXS.

There is also finely a distributed texture (Fig. 4.9b) that could be interpreted as being composed of smaller Pt nanoparticles. The texture decorates the SrTiO<sub>3</sub> (001) surface in between the 10-50 nm clusters. A careful accounting of the Pt coverage is in order, which, assuming a cylindrical volume ( $V_{Cylinder}$ ) may be estimated by:

$$\Theta = N_b D_X^{-2} V_{Cylinder}. \quad (4.3)$$

The nanoclusters will have a reduced average  $N_b$  where the reduction factor can be calculated by the ratio of  $2 \cdot R_X / D_X$  from Table 4.2, which for the 900°C annealed case is  $2 \cdot R_X / D_X = 0.86$ .

Thus, the coverage from the nanoclusters of the 900°C annealed case using the reduced  $N_b$  and the values in Table 4.1 would be ~1.1 ML Pt. With the XRF being 1.5 ML, the remaining 0.4 ML may be related to the surface texture. The features in the texture have a particulate appearance where the lateral dimension is ~1 nm (diameter) and the spacing,  $D \sim 5$  nm.

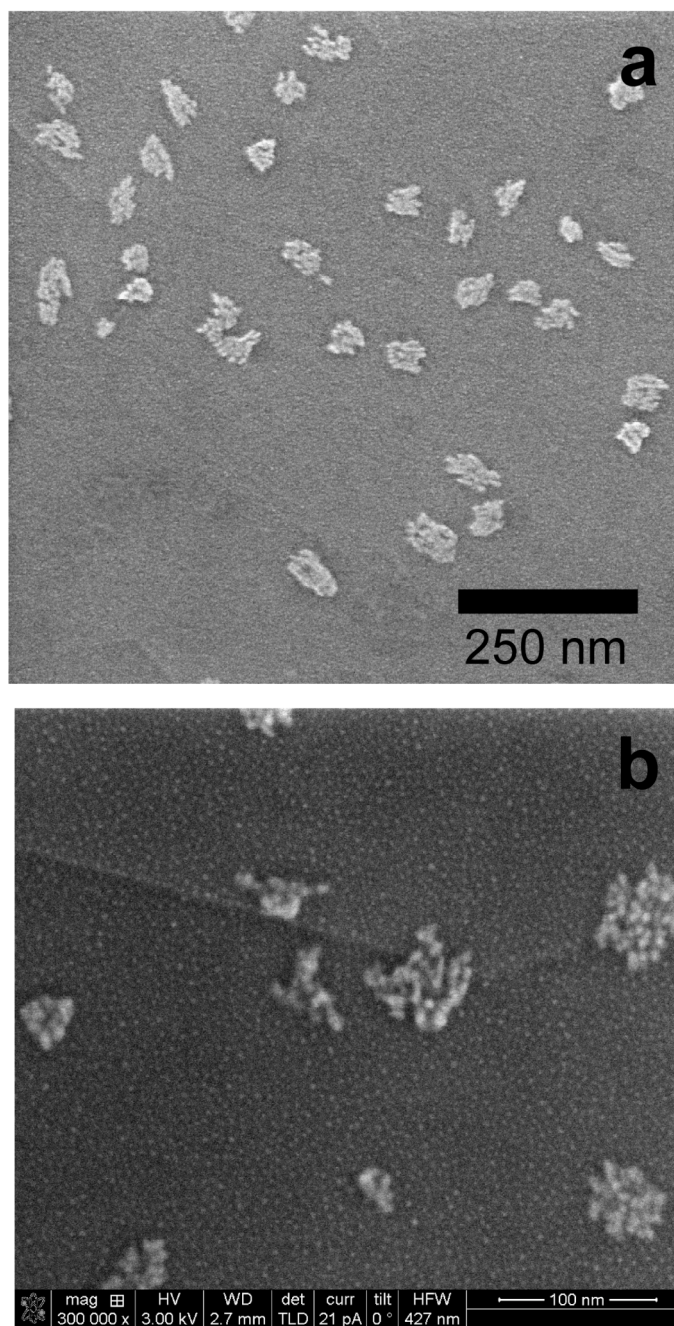


**Figure 4.9** High-resolution SEM images of the 900°C sample taken more than one year after the sample was prepared, annealed, and imaged by AFM. The images show what appears to be nanoparticle aggregates consistent with the size and spacing determined in AFM and GISAXS. XRF primarily rules out the texture of the SrTiO<sub>3</sub> surface in between particles to have a significant amount of platinum. Image (a) was taken with the Hitachi S-4800 SEM and (b) taken using the FEI Helios FIB-SEM at EPIC, NU. No special SEM surface treatment was used (i.e. gold coating).

For the surface texture to account 0.4 ML, the texture would need an effective  $\sim 1.2$  nm height using eq 4.3. Conversely, the nanoparticles from the GISAXS reported in Table 4.2 would have a  $\sim 10$  ML Pt coverage.

The GISAXS analysis yielded single modal size distributions for both the lateral and vertical directions. Any Pt structures in the surface texture could be a small part of the size distribution. The AFM also shows the atomic terraces that indicate any surface texture is smooth and conformal. Any isolated Pt atoms and structures would be detected as nanoparticles and roughness fluctuations. Thus, it seems consistent to take the missing 0.4 ML Pt as an upper bound of the possible Pt that could be incorporated into the surface texture. It is also possible that the surface texture has some amount of low  $Z$  elements such as carbon, since a significant amount of time elapsed between the AFM and SEM measurements.

The images provide compelling support that the Pt nanoparticles form aggregates that have not lost a significant portion of their surface area through sintering or coalescence. The Pt surface appears to be complex and could provide favorable catalytic activity as potentially more reactive Pt surfaces are exposed. Furthermore, the application of AFM, XRF, and GISAXS is justified as they provide new insights into the behavior of Pt/SrTiO<sub>3</sub>.

#### **4.5 Conclusions for PVD Pt nanoparticles**

Platinum nanoparticles supported on SrTiO<sub>3</sub> (001) have been prepared in UHV by physical vapor deposition and studied using AFM and a variety of X-ray techniques including the X-ray standing wave method, X-ray fluorescence, and GISAXS. From XSW measurements the platinum is uncorrelated to (nonepitaxial) the substrate lattice and GISAXS shows no indication of Pt faceting correlated to the substrate. Careful accounting of the platinum coverage

from XRF enables the average lateral dimension to be estimated. The low  $q_{xy}$  GISAXS data are consistent with the AFM 15-30 nm lateral size observed for the Pt clusters. The higher  $q_{xy}$  GISAXS provides information beyond the 10 nm lateral resolution of the AFM to detect small nanoparticles (1 – 2 nm) that are closely spaced (2 – 4 nm). This strongly suggests the platinum nanoparticles are aggregated without coalescence or sintering; a phenomenon which has been observed previously Refs. [8-10] using cluster beam deposition and TEM. High-resolution SEM images provide additional support that the Pt nanoparticles form aggregates.

The peculiar behavior of the platinum nanoparticles to resist complete coalescence is quite interesting and appears to offer a number of exciting opportunities for catalysis. A previous explanation for the lack of coalescence in the nanoparticles is a repulsive interaction based on electronic effects and mechanical distortion of the substrate.<sup>10</sup> Small-angle scattering techniques are well suited for collecting statistically meaningful data, which can in general be employed to model the attractive/repulsive interaction dynamics for hierarchical systems. Furthermore, aggregation is a key issue to address for applications such as catalysis where it often results in the loss of catalytic activity.

## Chapter 5: Nanoscale structure and morphology of platinum atomic layer deposition on SrTiO<sub>3</sub>

### 5.1 Atomic layer deposition

Atomic layer deposition is a thin film deposition technique that utilizes self-limiting surface reactions of precursor gases to deposit material in a layer-by-layer fashion upon completion of a precursor dosing sequence known as an ALD cycle. The technique has been known<sup>113, 114</sup> since the early 1970's, but recently has gained more interest as the number of compounds available for deposition has greatly expanded from semiconductors to nitrides, metals, and oxides. ALD oxide compounds, such as hafnium oxide, are of particular interest to serve as state-of-the-art microelectronic gate materials. The motivation behind this and other ALD applications stems from the extreme precision in which ALD uniformly coats complex support geometries.<sup>11-13</sup>

The precision of ALD is based on the reliance of precursors that react with the surface, but not each other. Precursor molecules typically constitute an organometallic compound and an oxidizing or reducing agent such as oxygen, hydrogen, or steam. The first precursor dose, typically the organometallic, will saturate the reactive sites on the surface through chemisorption. The ALD cycle is completed by a second precursor dose that only reacts with the adsorbed precursor species from the first dose. Usually, the second precursor liberates the remaining organic ligands on the adsorbed precursor to create a surface that is reactive to the next organometallic pulse. The classic ALD example is aluminum oxide using trimethylaluminum and steam.<sup>115</sup> The deposition proceeds with trimethylaluminum reacting with hydroxyl groups on the surface to liberate a methane molecule. The steam dose then

liberates the remaining methyl groups to leave behind the deposited Al atoms attached to hydroxyl groups that are ready for the next trimethylaluminum dose. Steady state growth then proceeds where the ALD occurs on the  $\text{Al}_2\text{O}_3$  film deposited in earlier cycles.

The formation of a film may not always occur in the first few ALD cycles as the process strongly depends on how efficiently a monolayer of precursor will adsorb on the surface. The efficiency of ALD in the early stages will be related to the precursor pressure, dosing time, reactivity of the surface, and the temperature. These factors combine to give a growth regime where an incomplete film forms and eventually coalesces leading to the steady state growth regime as the number of cycles increase. ALD at the early stages has not been widely studied and consequently a number of interesting opportunities arise to extend the capabilities of the technique. The key prospect related to this project is the formation of nanoparticles due to the incomplete coalescence of a film for the case of platinum. Noble metal ALD chemistries are particularly prone to the formation of nanoparticles.<sup>11, 13, 116-119</sup> A detailed understanding of the nucleation, growth and coalescence of the nanoparticles is needed at the nanometer length scale in order to systematically pursue the technological application of such nanoparticles from ALD.

This chapter explores the ALD of platinum on  $\text{SrTiO}_3$  (001) using alternating exposures to (Trimethyl) methylcyclopentadienylplatinum (IV) ( $\text{MeCpPtMe}_3$ ) and oxygen. Previous studies of Pt ALD using these precursors have focused mainly on the thick-film limit (steady state growth) in which Pt is deposited on itself.<sup>116-118, 120</sup> These studies support a Pt ALD mechanism in which adsorbed oxygen on the Pt surface plays a critical role by providing reactive sites for the  $\text{MeCpPtMe}_3$  precursor. On the other hand, Pt ALD on  $\text{SrTiO}_3$  (001) is likely to possess a more complex growth mechanism due to differences in the surface chemistry between



the initial SrTiO<sub>3</sub> (001) substrate and the growing Pt film. Of particular interest is the initial nucleation process on the SrTiO<sub>3</sub> (001) surface since it will likely dictate the morphology of the Pt deposit. Previous work demonstrated that the substrate chemistry can strongly influence the initial nucleation during Pt ALD.<sup>121</sup> The focus hereunder will be on characterizing the early stages of the Pt ALD on SrTiO<sub>3</sub> (001) using a suite of X-ray and imaging techniques.

## 5.2 Platinum atomic layer deposition

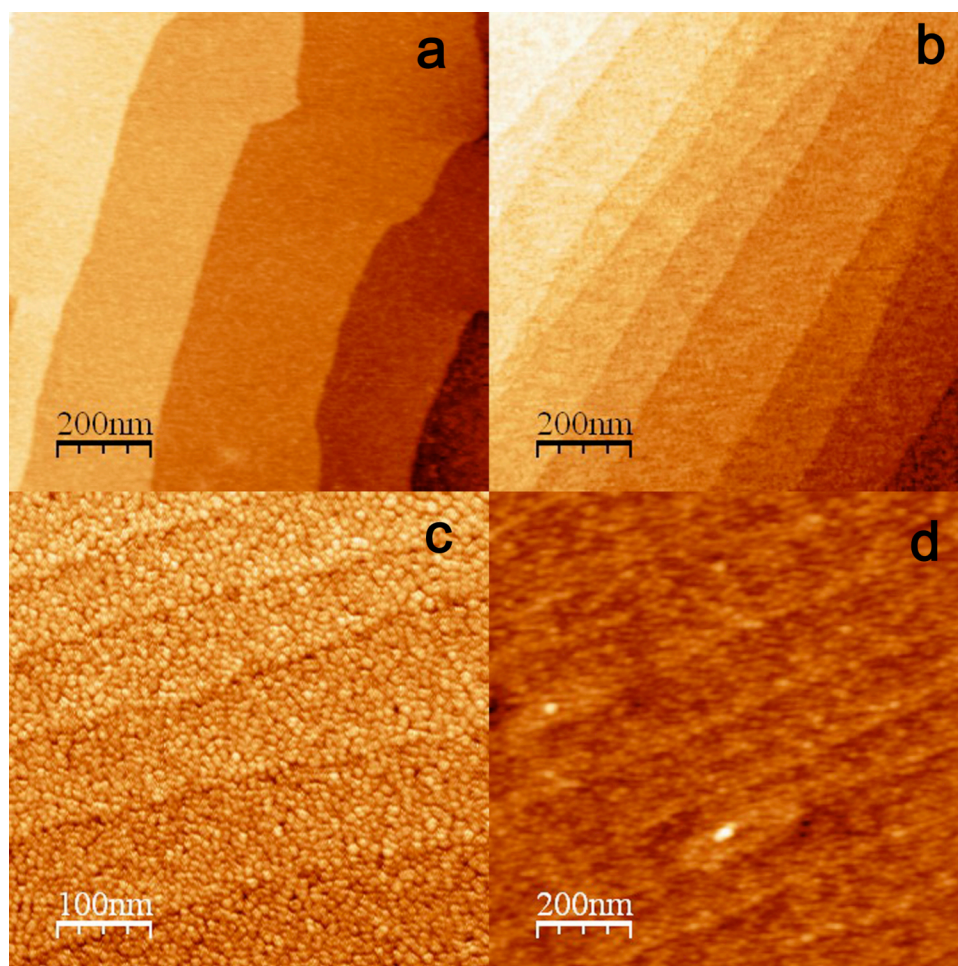
The ALD was performed by J. Elam, Energy Systems Division, Argonne National Laboratory. The SrTiO<sub>3</sub> (001) substrates (MTI Corp) prepared according to the description in Chapter 2 were transferred to a custom ALD reactor consisting of a hot-walled stainless steel tube and a computer controlled gas manifold for precursor dosing.<sup>122</sup> After installing the SrTiO<sub>3</sub> substrates in the ALD reactor, the substrates were allowed to equilibrate and outgas for 10 minutes at 300°C in flowing nitrogen before commencing the Pt ALD. Platinum ALD was accomplished using alternating exposures to MeCpPtMe<sub>3</sub> (Strem Chemicals, 99.5% pure) and 400 sccm of ultra-high purity (99.995% pure) oxygen at 300°C using 360 sccm of ultra-high purity (99.995% pure) nitrogen carrier gas at a steady state pressure of ~1 Torr. During the MeCpPtMe<sub>3</sub> exposures, 300 sccm of N<sub>2</sub> was passed through a stainless steel bubbler containing the MeCpPtMe<sub>3</sub> heated to 40°C, and the N<sub>2</sub> was diverted to bypass the bubbler after the exposures. Each Pt ALD cycle consisted of a 10 s exposure to MeCpPtMe<sub>3</sub>, a 5 s N<sub>2</sub> purge period, a 5 s exposure to O<sub>2</sub>, and a final 5 s N<sub>2</sub> purge period. Companion measurements on Si(100) and glass surfaces as well as using an *in situ* quartz crystal microbalance yielded a growth rate of 0.5 Å/cycle Pt.

### 5.3 Measurements of Pt ALD on SrTiO<sub>3</sub> (001)

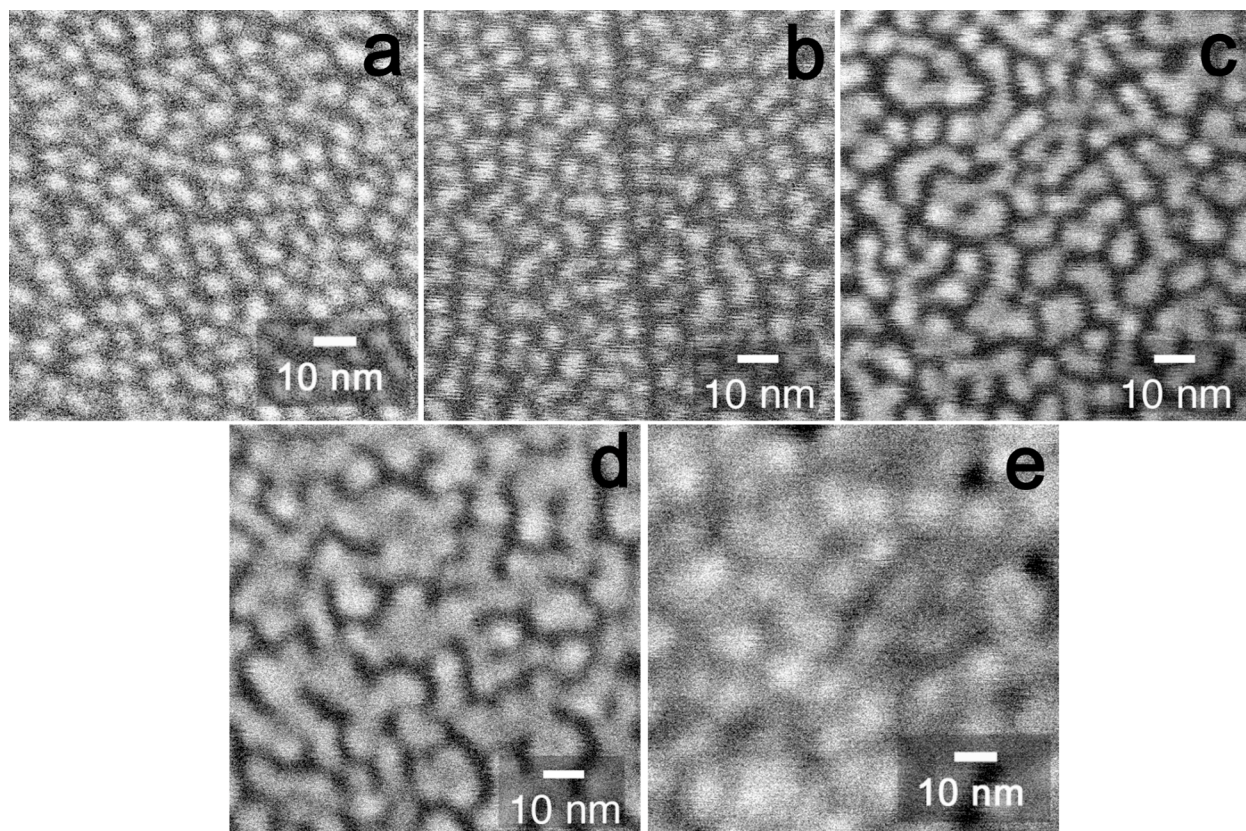
Figure 5.1 illustrates the evolution of Pt film growth with AFM images after 10, 15, 20, and 80 ALD cycles. For Pt/SrTiO<sub>3</sub> samples prepared using 15 or fewer ALD cycles, only subtle changes can be perceived in AFM. After 20 ALD cycles, Pt nanoparticles appear to be decorating the surface, whereas a granular, continuous Pt film is apparent following 80 ALD cycles. In all cases, the measured RMS roughness of the Pt/SrTiO<sub>3</sub> surface does not exceed 0.5 nm, thus indicating the high conformality of the ALD process. It should also be noted that the 0.4 nm atomic steps of the underlying SrTiO<sub>3</sub> (001) substrate are still observable even in the case of 80 ALD cycles.

Figure 5.2 presents SEM images following 15, 20, 30, 40, and 80 Pt ALD cycles. These images clearly show that the Pt nucleates on the SrTiO<sub>3</sub> surface as discrete islands that grow laterally with increasing ALD cycles. The lateral spacing of these nanoparticles is on the order of a few nanometers. The nanoparticles coalesce to form a nearly continuous film at approximately 40 ALD cycles as evident in the morphology and the decreasing number of isolated nanoparticles per area. Evidence for persistent SrTiO<sub>3</sub> (001) step edges are also apparent as indicated by the diagonal line cutting across Figure 5.2 (b).

The GISAXS data were collected with a photon energy of 8.00 keV and a sample to detector distance of ~2.1 m using a MAR 165 CCD detector. Figure 5.3 shows the GISAXS for a blank SrTiO<sub>3</sub> (001) substrate after the BHF etch/annealing treatment. Two-dimensional GISAXS data are presented in Figure 5.4 for 10, 20, 30, and 40 cycles of Pt ALD. The scattering intensity concentrates in the small angle region as the number of ALD cycles increase, thus indicating that the Pt nanoparticles are increasing in size.



**Figure 5.1** AFM images following Pt ALD: a) 10, b) 15, c) 20, d) 80 ALD cycles. At 20 ALD cycles, Pt nanoparticles can be directly observed, whereas the Pt film possesses a fine granular structure after 80 ALD cycles. The 0.4 nm atomic steps of the underlying SrTiO<sub>3</sub> (001) substrate can still be observed after 80 ALD cycles. In all cases, the RMS roughness of the films does not exceed 0.5 nm.



**Figure 5.2** SEM images following Pt ALD: a) 15, b) 20, c) 30, d) 40, e) 80 cycles. At 15 ALD cycles, Pt nanoparticles have nucleated and then grow and coalesce with increasing ALD cycles. In particular, the grains take irregular and elongated shapes at the later stages of Pt ALD growth. Images were collected by Jeff Elam using a Hitachi S-4700 SEM located in the Electron Microscopy Center for Materials Research at ANL.

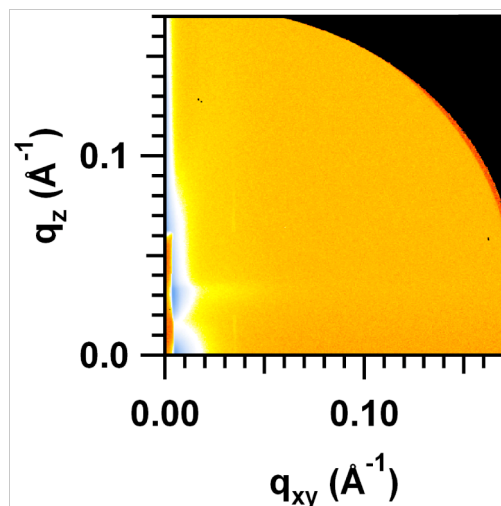


**Figure 5.3** GISAXS data for a blank SrTiO<sub>3</sub> (001) substrate after etching and annealing. Collected at 12ID-C, APS.

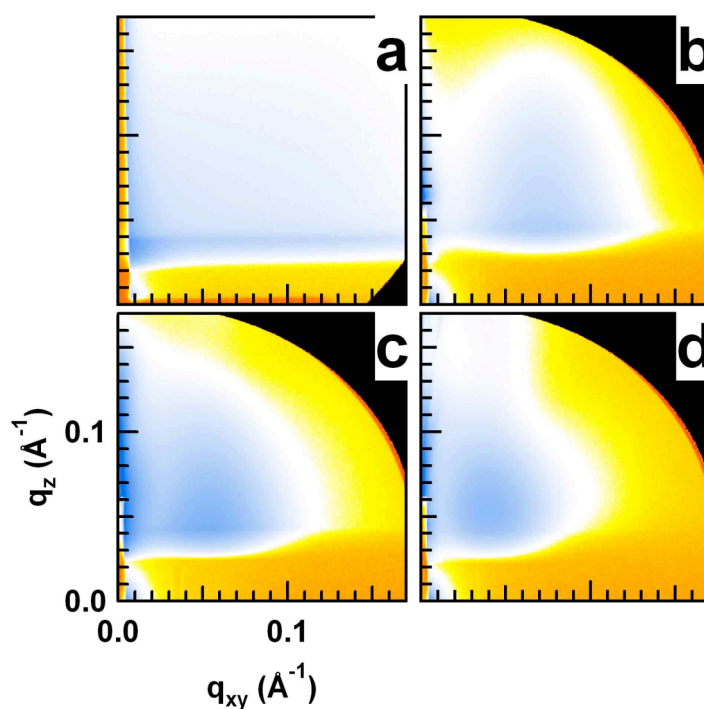


**Figure 5.4** GISAXS data after: a) 10, b) 20, c) 30, d) 40 ALD cycles. The scattered intensity lobe moves inward as the number of ALD cycles increases, thus indicating that the particle size and the interparticle spacing is increasing. Collected at 12ID-C, APS.

Also, the GISAXS peak representative of interparticle spacing becomes more apparent as the number of ALD cycles increase. Line cuts were extracted from the two-dimensional GISAXS data and fit using the distorted wave Born approximation<sup>91, 94</sup> (DWBA) framework with a cylinder form factor and an interference function under local monodisperse approximation.<sup>91, 96</sup> (LMA) In addition, the 1-D paracrystal model<sup>91, 95</sup> was used to represent the interparticle spacing distribution. The vertical data were fit using the IsGISAXS software.<sup>91</sup> The line cut data and fits are plotted in Figure 5.5.

For the in-plane scattering, an additional term was added to the scattered intensity in eq 3.8 in order to account for strong scattering near  $q_{xy} = 0$ . This term is based on the unified model from Beaucage<sup>123, 124</sup> to give the lateral scattering intensity,  $I(q_{xy})$ , as:

$$I(q_{xy}) = I_U(q_{xy}) + \langle |F(q_{xy})|^2 \rangle S(q_{xy}), \quad (5.1)$$

where  $I_U(q_{xy})$  is determined by the unified model, and  $\langle |F(q_{xy})|^2 \rangle S(q_{xy})$  represents the particle scattering for the DWBA with the LMA. The general form of the intensity from the unified model is calculated as:

$$I_U(q) = G \exp\left(-\frac{q^2 R_g^2}{3}\right) + B \left(\frac{1}{q}\right)^P, \quad (5.2)$$

The parameters related to  $I_U(q_{xy})$  include the Guinier prefactor,  $G$ , the Guinier radius,  $R_g$ , the power-law prefactor,  $B$ , and the power-law exponent,  $P$ . The fitting results including the unified model parameters and particle dimension and spacing are summarized in Table 5.1.

The fitting results from Table 5.1 confirm the observations from the microscopy data that the in-plane particle size,  $R$ , increases from 1.1 nm to 3.5 nm with increasing number of Pt ALD cycles.

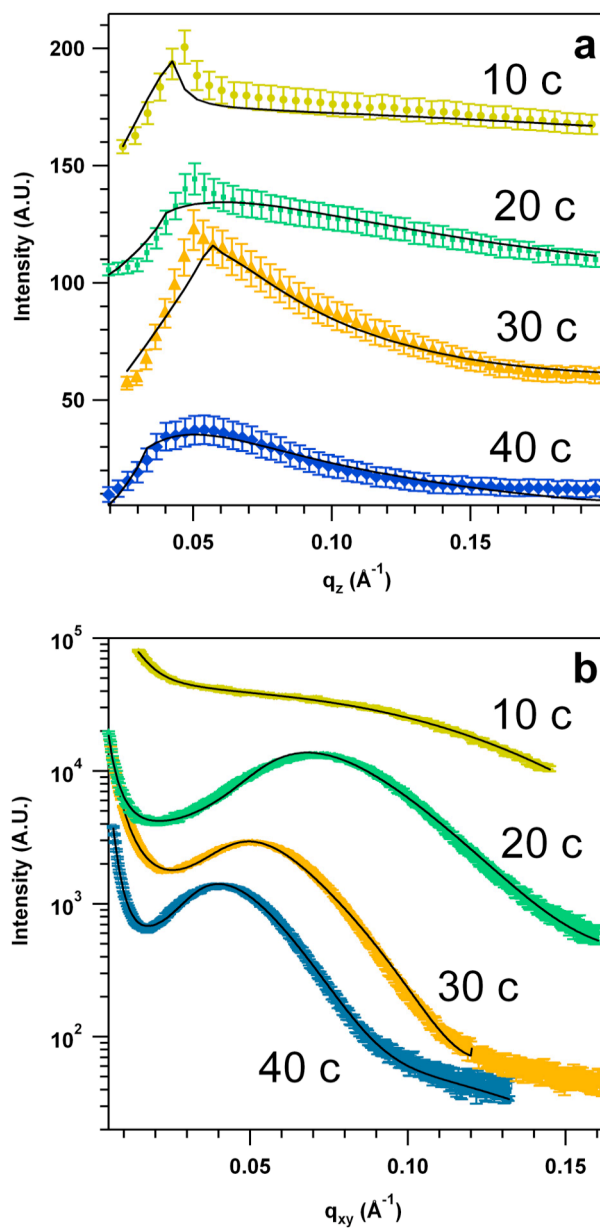


**Figure 5.5** GISAXS line cut data and fits for a) vertical and b) horizontal scattering. The individual curves are offset for clarity. The data were fit with a distorted wave Born approximation cylinder form factor and the local monodisperse approximation. The horizontal fitting also included a term based on the unified small-angle X-ray scattering model that accounts for the data near the origin.

ALD Cycle	$R$ (nm)	$\sigma_R$ (nm)	$H$ (nm)	$\sigma_H$ (nm)	H/R	$D$ (nm)	$\sigma_D$ (nm)	$G$	$R_g$ (nm)	$B$	$P$
10	1.1	0.1	1.2	0.3	1.1	2.2	0.8	$8.7 \times 10^7$	35	$1.4 \times 10^2$	3.8
20	2.1	0.5	2.3	0.6	1.1	6.3	1.3	$3.0 \times 10^1$	54	$2.9 \times 10^3$	2.4
30	3.1	0.7	3.0	0.8	1.0	9.0	2.1	$7.8 \times 10^4$	31	$3.1 \times 10^3$	2.4
40	3.5	0.9	3.8	1.0	1.1	9.0	2.5	$2.0 \times 10^5$	90	$2.9 \times 10^2$	3.6

**Table 5.1** GISAXS fitting and analysis results. The particle model is taken to be a cylinder of radius,  $R$ , and height,  $H$ , with a center-to-center interparticle spacing,  $D$ .  $G$ ,  $R_g$ ,  $B$ , and  $P$  are parameters from the unified fit model for scattering near the beam stop. The  $\sigma$  parameter gives the distribution width of the respective parameters.



The GISAXS data also reveal that the out-of-plane particle size,  $H$ , increases from 1.2 nm to 3.8 nm. The  $H/R$  aspect ratio for all particles is nearly unity, which indicates that the Pt nanoparticles grow isotropically under these conditions. The interparticle spacing,  $D$ , is defined as the center-to-center distance for the Pt nanoparticles. From the GISAXS results, the interparticle spacing is found to increase from 2.4 nm to 9.0 nm, which is consistent with nanoparticle coalescence causing a decrease in the number of particles per unit area.

XRF measurements allow the total Pt surface coverage to be measured as a function of the number of ALD cycles. The XRF data are plotted against the number of ALD cycles in Figure 5.6. This plot suggests a decrease in the growth rate following ~40 ALD cycles. The solid line plotted in Figure 5.6 results from the growth model that is discussed below.

In effort to confirm the chemical state for the platinum deposited via ALD, X-ray photoelectron spectroscopy (XPS) was performed. Figure 5.7 shows XPS spectra of the Pt 4f lines for 40 Pt ALD cycles collected at Keck II, NU (Omicron). The line marks the Pt 4f<sub>7/2</sub> line position at 71.2 eV for metallic platinum.<sup>125</sup> The approximate peak position for the Pt ALD samples is 71.0 eV, which indicates the Pt is in a metallic form. For completely oxidized platinum, the peak position would be shifted higher in energy by 3+ eV.

Nanoparticle clustering, such as described in Chapter 4, was not observed in any of the ALD cases. This is evident in the SEM images of Figure 5.2 and in Figure 5.8, which shows the GISAXS CCD images of the 900°C PVD Pt case (a) and the GISAXS CCD image for 40 ALD cycles. Both images are taken under the same experimental conditions and a comparison of the region between  $2\theta_f = 0 - 0.5^\circ$  for both images shows the effect of nanoparticle clustering.

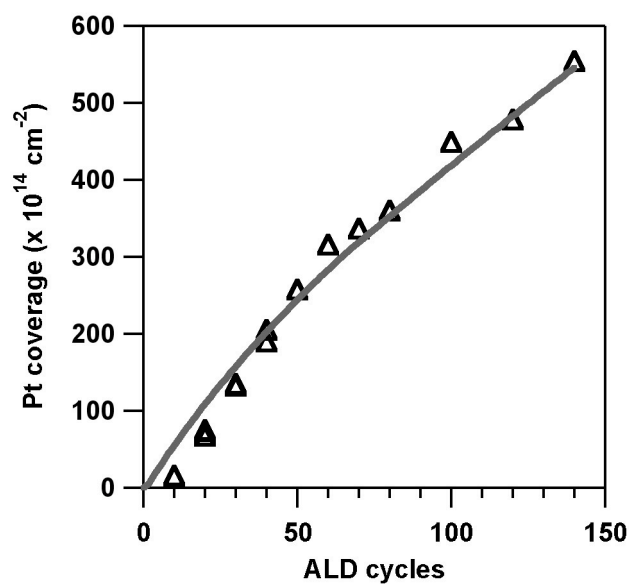


**Figure 5.6** XRF Pt coverage vs. ALD cycle. A change in growth rate is observed at ~40 ALD cycles. The solid line is based on a growth model that includes both deposition directly on the Pt particles and deposition on the surrounding SrTiO<sub>3</sub> surface followed by surface diffusion. XRF data collected at NU X-ray facility (18 kW rotating anode, Zr coated).

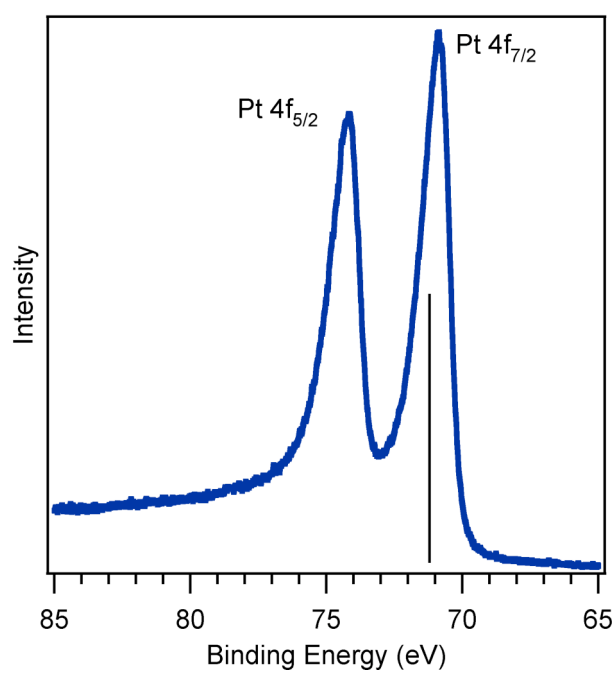


**Figure 5.7** XPS spectra of the Pt 4f lines for 40 ALD cycles. The line marks the Pt 4f<sub>7/2</sub> line position at 71.2 eV for metallic platinum from Ref. [125]. The approximate peak position for the Pt ALD samples is 71.0 eV. For completely oxidized platinum, the peak position would be shifted higher in energy by 3+ eV. XPS collected at Keck II, NU.

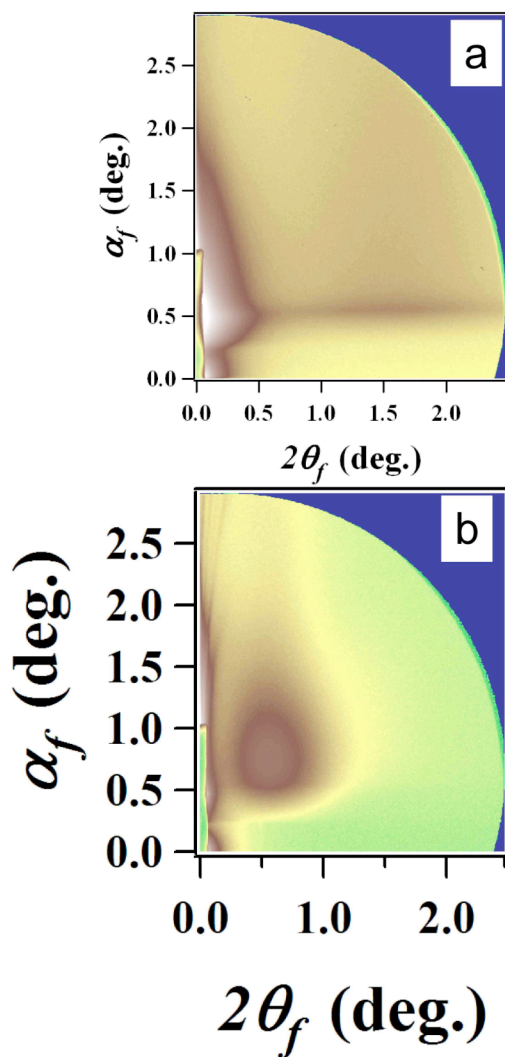


**Figure 5.8** GISAXS CCD images of (a) PVD Pt 900°C and (b) 40 ALD cycles. The ALD Pt nanoparticles do not show the same intensity profile near the origin that is characteristic of nanoparticle clustering. This suggests along with SEM images in Fig 5.2 that the ALD Pt does not aggregate like the PVD Pt. Collected at 12ID-C, APS.

Namely, there is a substantial amount of intensity for the PVD case with nanoparticle aggregation. The ALD example in Fig. 5.8 (b) does not have the intensity near the origin that would be indicative of nanoparticle clustering. All the other ALD cases show similar results as that of Figure 5.8 (b).

#### **5.4 Model of Pt nanoparticle nucleation and growth via ALD**

The model for Pt ALD proposed by Aaltonen *et al.* asserts that oxygen adsorbed on the surface of the Pt film dissociates the MeCpPtMe<sub>3</sub> precursor during the metalorganic exposures.<sup>116</sup> Consequently, any Pt present on the SrTiO<sub>3</sub> from the initial Pt ALD cycles will provide reactive sites for MeCpPtMe<sub>3</sub> dissociation during subsequent Pt ALD cycles, thus leading to nanoparticle growth. However, the Aaltonen model does not address the possible influence of the bare SrTiO<sub>3</sub> surface during the Pt nucleation. Some intriguing issues lie in determining the role bare SrTiO<sub>3</sub> oxide plays in the deposition and how surface diffusion of Pt atoms may affect the growth of Pt nanoparticles on the surface prior to film closure.

Inspection of the SEM images from Figure 5.2 reveals that the nanoparticles for 15 cycles are relatively uniform in shape, but as the number of cycles increase, elongated and non-symmetric particle shapes appear. The nanoparticles, however, possess a narrow enough height distribution and low enough RMS roughness that the influence of the 0.4 nm atomic steps of the underlying SrTiO<sub>3</sub> substrate remains observable in AFM for as many as 80 ALD cycles. These observations provide initial evidence for a growth mechanism that includes adsorption of MeCpPtMe<sub>3</sub> on the SrTiO<sub>3</sub> surface followed by diffusion of the Pt species to the growing nanoparticles.

Additional insight into the growth mechanism can be gained by considering the XRF data

plotted in Figure 5.6. Specifically, Figure 5.6 shows two regions of growth such that the region below  $\sim 40$  ALD cycles shows a growth per cycle that is approximately two-fold higher than the region above  $\sim 40$  ALD cycles. Moreover, the magnitude of the Pt growth beyond 40 ALD cycles is consistent with the previously observed growth rate for Pt ALD indicating that below 40 ALD cycles the Pt growth rate is abnormally large. The 40 ALD cycle transition point between these two growth regions coincides approximately with the point at which the ALD Pt nanoparticles coalesce to form a continuous film as observed by SEM in Figure 5.2 (c).

The region of higher initial growth is uncommon and thus requires further discussion. Existing models for nucleation and growth of ALD films<sup>126, 127</sup> predict three growth regimes: (1) an incubation period of slow, inhibited growth; (2) a transition regime characterized by island growth and coalescence where the increasing surface area produces a *non-linear* thickness change and the growth rate may exceed the steady-state growth rate by as much as 30%; (3) a steady-state regime where the thickness increases linearly. In contrast, Figure 5.6 exhibits an initial regime of *linear* growth that exceeds the steady-state growth rate by 100%, followed by a steady-state regime. To account for the initial regime of higher, linear growth observed here, the existing ALD growth models were modified to one in which the Pt deposits at a higher rate on the bare SrTiO<sub>3</sub> surface, but then diffuses to the growing Pt nanoparticles. The model assumes platinum also grows on the nanoparticles, but at a lower rate. During the model film growth, the relative proportions of bare SrTiO<sub>3</sub> and Pt-coated surface are computed. At the point of nanoparticle coalescence, the platinum ALD will only continue on the platinum film because there is no more bare SrTiO<sub>3</sub> substrate available. In this model, the distance between the nanoparticles, as well as the fraction of reactive sites on both the SrTiO<sub>3</sub> and the Pt were varied

to match the experimental data. It should be noted that this study did consider ALD for fewer than 10 cycles. The results (AFM and XRF) showed minimal deposition and were sporadic. This irregular deposition prevented a systematic study for fewer than 10 Pt ALD cycles.

The resulting fit is shown as the solid line in Figure 5.6. The fit uses an initial nanoparticle spacing of 12 nm, and the fraction of reactive sites on SrTiO<sub>3</sub> and Pt are 0.4 and 0.11, respectively. The interparticle spacing from the model agrees reasonably well with the spacing between the Pt nanoparticles in the SEM images shown in Figure 5.2. The fraction of reactive sites of 0.11 on the Pt reproduces the experimentally determined Pt growth rate in this study as well as from the literature.<sup>116</sup> The fraction of reactive sites on the SrTiO<sub>3</sub> of 0.4 suggests that the SrTiO<sub>3</sub> has a density of reactive sites for Pt ALD that is approximately fourfold higher than Pt.

This model for Pt nucleation and growth requires relatively fast diffusion of the Pt on the SrTiO<sub>3</sub> surface so that the Pt deposited on the bare SrTiO<sub>3</sub> can migrate to the Pt nanoparticles. Platinum diffusion rates on metal surfaces can be estimated by calculating the surface diffusion coefficient,  $D_s$ , using an empirical relationship given by Gjostein<sup>128</sup>:

$$D_s(T) = 0.014 \exp\left(-\frac{13T_m}{R_c T}\right), \quad (5.3)$$

where  $T$  and  $T_m$  are the substrate temperature and melting point, respectively, in K, and  $R_c$  is the gas constant in cal mol<sup>-1</sup> K<sup>-1</sup>. At the deposition temperature, 573K,  $D_s = 1.2 \times 10^{-12}$  cm<sup>2</sup>/s which for the 10 s time interval following the beginning of the oxygen exposure yields a platinum diffusion distance  $x = \sqrt{D_s t} = 30$  nm. Since the SEM and GISAXS data suggest that the interparticle distance is significantly less than 30 nm, it is plausible that Pt surface diffusion will

play an important role in the growth mechanism.

The increased growth rate prior to film closure shown in Figure 5.6 argues that the SrTiO<sub>3</sub> has a catalytic effect in the Pt ALD process. This effect is reflected in the modeling as a higher fraction of reactive sites on SrTiO<sub>3</sub> than on Pt. As a catalyst support, SrTiO<sub>3</sub> can reduce carbonaceous build up during hydrocarbon oxidation as described in Chapter 2. The implication for ALD would presumably be that the SrTiO<sub>3</sub> catalyzes the conversion of the organic ligands on the adsorbed MeCpPtMe<sub>3</sub>, thereby reducing steric hindrance and increasing the Pt growth rate.

The nucleation of most noble metals (including platinum, ruthenium, and palladium) during ALD appears to occur via the coalescence of nanoparticles<sup>12, 13, 116-120</sup> Thus, the role of diffusion is also likely to be important in the growth dynamics of these materials via ALD. For instance, nanoparticle size and number density may vary when noble metal ALD is performed on different substrates depending on the relative surface diffusion rates for these substrate materials.

This hypothesis should motivate future studies directed at the early stages of noble metal growth by ALD.

## 5.5 Summary of Pt ALD

In summary, the early stages of nucleation and growth of ALD Pt on single crystal SrTiO<sub>3</sub> (001) surfaces has been studied. Uniformly sized Pt nanoparticles initially nucleate and then grow and coalesce into a continuous Pt film. Despite the particulate nature of the Pt nucleation, the films remain smooth enough to preserve the 0.4 nm atomic steps of the underlying SrTiO<sub>3</sub> (001) substrate even after 80 ALD cycles. Using AFM, SEM, GISAXS and XRF, a detailed growth model has been developed where Pt nanoparticles nucleate on the



substrate and subsequently grow from a combination of precursor adsorption directly on the Pt nanoparticles as well as precursor adsorption on the surrounding SrTiO<sub>3</sub> followed by surface diffusion to the nanoparticles. This growth mechanism is expected to be applicable to other noble metal ALD chemistries, thus presenting unique opportunities for applications that require either isolated nanoparticles or conformal, continuous thin films.

## **Chapter 6: Structure and morphology of platinum nanoparticles deposited via atomic layer deposition on strontium titanate nanocubes**

### **6.1 ALD platinum growth on SrTiO<sub>3</sub> nanocubes**

The nucleation of platinum nanoparticles via atomic layer deposition (ALD) on SrTiO<sub>3</sub> nanocube extends the work on single crystals discussed earlier to a more industrially relevant support. The SrTiO<sub>3</sub> nanocubes, prepared by sol-precipitation—hydrothermal treatment, have {001} faces and average 60 nm on a side.<sup>22</sup>

The combination of imaging and X-ray techniques provides an optimal approach to investigate the structure, morphology, and chemical state of the nanoparticles. Here the high-resolution imaging capabilities of scanning electron microscopy (SEM) is utilized to confirm the nanoparticle morphology and size. The platinum nanoparticle size and dispersion is further explored with small-angle X-ray scattering (SAXS) and wide-angle X-ray scattering (WAXS). Finally, the chemical state and the local atomic structures of the platinum nanoparticles are studied using X-ray absorption spectroscopy (XAS), the former of which is revealed by the X-ray absorption near-edge structure (XANES) and the latter extended X-ray absorption fine structure (EXAFS).

### **6.2 Synthesis of ALD Pt / SrTiO<sub>3</sub> nanocubes**

#### **6.2.1 Experimental Section**

##### **SrTiO<sub>3</sub> nanocube growth**

SrTiO<sub>3</sub> nanocubes were synthesized following a sol-precipitation—hydrothermal treatment procedure identical to that described in a previous paper<sup>22</sup> except for the fact that the

hydrothermal treatment was conducted for 36 h instead of 24 h.

### 6.2.2 Pt ALD on nanocubes

Platinum nanoparticles were deposited onto the SrTiO<sub>3</sub> nanocubes using atomic layer deposition (ALD). For this procedure, ~0.25 g of the nanocubes were spread inside of a stainless steel tray that was covered by a stainless steel mesh to contain the powder while allowing easy access by the ALD precursors<sup>129 221</sup>. Prior to the ALD, the SrTiO<sub>3</sub> nanocubes were cleaned *in situ* using a 400 sccm flow of 10% ozone in oxygen at a temperature of 300°C. The Pt ALD was accomplished using alternating exposures to (methylcyclopentadienyl) trimethylplatinum (MeCpPtMe<sub>3</sub>) and oxygen at 300°C<sup>116</sup> using a viscous flow ALD reactor<sup>122</sup>. During the deposition, a constant 90 sccm flow of ultrahigh purity (99.995%) carrier gas swept through the reactor at a pressure of 0.90 Torr. The MeCpPtMe<sub>3</sub> was contained in a stainless steel bubbler heated to 50°C to increase the vapor pressure of the precursor. The reactant exposures were 200 s in duration with partial pressures of 0.05 Torr for MeCpPtMe<sub>3</sub> and 0.20 Torr for oxygen. Nitrogen purge periods of 50 s were used between reactant exposures. A series of Pt catalyst samples were prepared using 1, 2, 3, 4, and 5 Pt ALD cycles. The sample mass was measured using an analytical balance before and after the Pt ALD to determine the Pt loading.

The SrTiO<sub>3</sub> nanocubes were examined before and after the Pt ALD by scanning electron microscopy (SEM) using a Hitachi S-4700 with a field emission gun electron beam source.

### 6.3 X-ray measurements of ALD Pt / SrTiO<sub>3</sub> nanocubes

All X-ray data sets were collected at the Advanced Photon Source (APS) (Argonne National Laboratory) in transmission mode with the sample powder mounted on scotch tape. The powder samples and reference materials were uniformly spread onto tape and then folded to

achieve appropriate signal levels for the respective scattering and absorption measurements. A scotch tape background was collected and removed for the X-ray scattering data.

The SAXS data sets were collected at the APS 12ID-C undulator station with a MAR 165 (2048 x 2048 pixels) CCD detector at an incident photon energy of 12.00 keV ( $\lambda = 1.033 \text{ \AA}$ ). A series of slits collimated the beam and the sample was mounted on motorized stage. The momentum transfer was calibrated using a silver behenate standard and the detector to sample to detector was  $\sim 2 \text{ m}$ .

The WAXS data were collected at the APS 5ID-D undulator beam line with a dual chip 100 mm by 200 mm Roper CCD detector. The incident photon energy of 16.005 keV ( $\lambda = 0.77466 \text{ \AA}$ ) was selected using a Si (111) monochromator and the beam was further collimated with three slits to give a size of approximately 0.2 mm by 0.2 mm. The detector position relative to the source was calibrated with a silicon diffraction grating with 3600 lines/mm (LightSmyth Technologies, no. SLG-C36-1212-Si). This allowed the determination of the momentum transfer calibration and sample to detector distance (235 mm).

The XAS measurements were carried out around the Pt-L<sub>3</sub> edge (11.564 keV) at the bending magnet beamline of the DND-CAT (5BM-D). The XAS spectra were collected in fluorescence mode using a Xenon-filled Lytle cell and a Zn filter to minimize the scattering signals. The XAS spectra of the reference materials were collected in transmission mode using gas ionization chambers (Oxford Danfysik). The X-ray photon energy was calibrated using a Pt metal foil. During the XAS measurements, the energy stability was regularly monitored by simultaneously measuring the Pt foil, which was placed in between the second and third ion chambers. The XAS spectra were all measured from -200 eV below to 1000 eV (wave vector  $k$

$\sim 16 \text{ \AA}^{-1}$ ) above the absorption edge. The near edge spectra were collected with energy step of 0.5 eV. Data processing was performed using the Athena program.<sup>130</sup>

## 6.4 Characterization results

### 6.4.1 Mass and Microscopy

The uncoated SrTiO<sub>3</sub> nanoparticles are non-porous, single-crystalline, cube-shaped particles having the {001} faces primarily exposed, with an average edge length of 60 nm, and a Brunauer-Emmet-Teller surface area of 20 m<sup>2</sup> g<sup>-1</sup>.<sup>22</sup> Figure 6.1 shows the dependence of the Pt loading on the number of Pt ALD cycles performed on the SrTiO<sub>3</sub> nanocubes. This graph shows a linear trend with a slope of 4.4 wt% per Pt ALD cycle. Using the SrTiO<sub>3</sub> surface area of 20 m<sup>2</sup>/g and the previously observed Pt ALD growth rate of 0.5 Å per cycle<sup>116</sup>, the expected mass gain is 2.1 wt% per cycle. The measured weight gain is larger by two fold indicating a higher initial growth rate for ALD Pt on the SrTiO<sub>3</sub> surface as compared to the Pt surface. Growth rates in ALD are typically dictated by the number of ligands, which remain on the surface following adsorption of the metal precursor because these ligands will prevent the adsorption of additional precursor molecules. It is possible that fewer MeCp and methyl ligands remain following adsorption of MeCpPtMe<sub>3</sub> on the SrTiO<sub>3</sub> surface because these ligands react with surface hydroxyls on the SrTiO<sub>3</sub> to liberate gaseous methylcyclopentadiene and methane.

Figure 6.2 shows SEM images of the SrTiO<sub>3</sub> nanocubes recorded before (a) and after (b) 5 Pt ALD cycles. Comparison of these images clearly reveals the presence of Pt nanoparticles resulting from the ALD treatment. Although the details in these images are nearly at the resolution limit of the SEM, the Pt nanoparticles have a diameter of  $\sim 3$  nm and are uniformly dispersed on all exposed surfaces of the SrTiO<sub>3</sub> nanocubes.

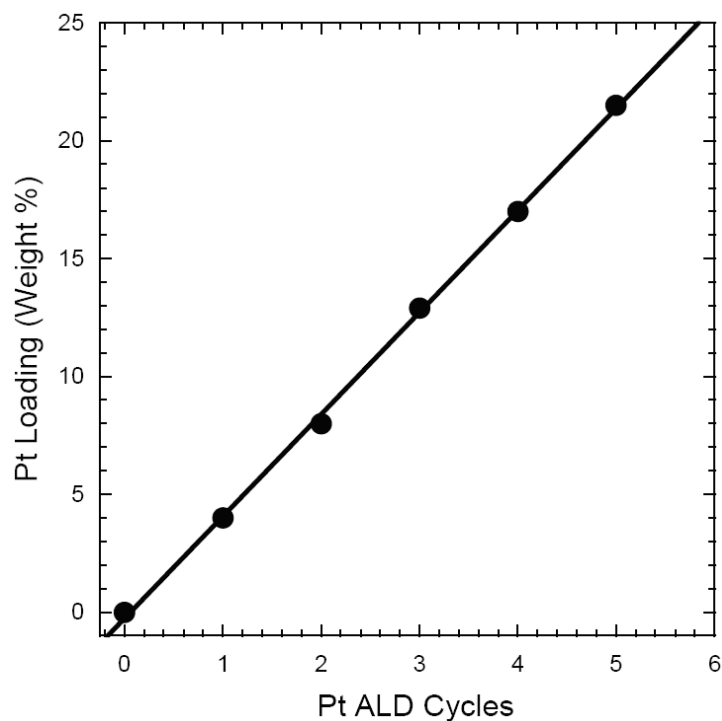


**Figure 6.1** Platinum loading versus number of Pt ALD cycles measured by mass gain. The solid line shows a linear least-squares fit to the data. Data collected by Jeff Elam, ANL.

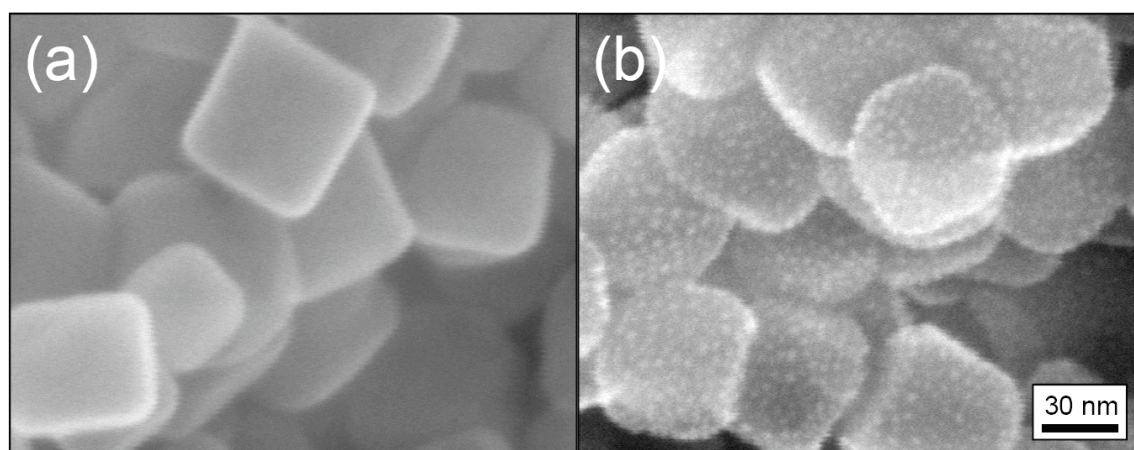


**Figure 6.2** SEM images of STO nanocubes before (a) and after (b) coating with Pt nanoparticles using 5 ALD Pt cycles. Images taken at the Electron Microscopy Center for Materials Research, ANL by Jeff Elam using a Hitachi S-4700 SEM.

### 6.4.2 X-ray Scattering

The SAXS data are plotted in Figure 6.3 for the five Pt ALD cases and the blank SrTiO<sub>3</sub>. The data show a peak around  $q = 0.15 \text{ \AA}^{-1}$ , which is related to the constructive interference from the platinum nanoparticles. The peak position,  $q = q_p$ , depends on the ALD cycle and relates the average nanoparticle spacing center-to-center,  $D$ , where:

$$D = \frac{2\pi}{q_p}. \quad (6.1)$$

Fitting a pseudo-Voigt function with a power-law background enables the determination of the peak position; the solid lines in Figure 6.3 represent the peak fits. The fitting results are plotted against the ALD cycle in Figure 6.4. The interparticle spacing increases in a linear fashion from 3.5 to 6.3 nm as the number of ALD cycles increases and follows linear growth law.

The wide-angle X-ray scattering is equivalent to the powder diffraction from the nanocubes and platinum nanoparticles. An example of the diffraction pattern is shown in Figure 6.5 for the uncoated SrTiO<sub>3</sub> nanocubes where the Bragg peaks have been indexed. The room temperature lattice constants of 3.924Å for cubic-F Pt and 3.905Å for cubic-P SrTiO<sub>3</sub> are such that the broadened Pt Bragg peaks overlap those of SrTiO<sub>3</sub>. Using the Scherrer equation<sup>131</sup> the mean crystallite size ( $t_H$ ) in the  $H=hkl$  direction can be determined from the *fwhm* of the peak,  $\Delta q$ , as:

$$t_H = 0.9 * \frac{2\pi}{\Delta q}, \quad (6.2)$$

The uncoated SrTiO<sub>3</sub> nanocubes were inspected for line broadening and showed a ~40 nm domain size from the (110), (111), (200) and (211) peaks.

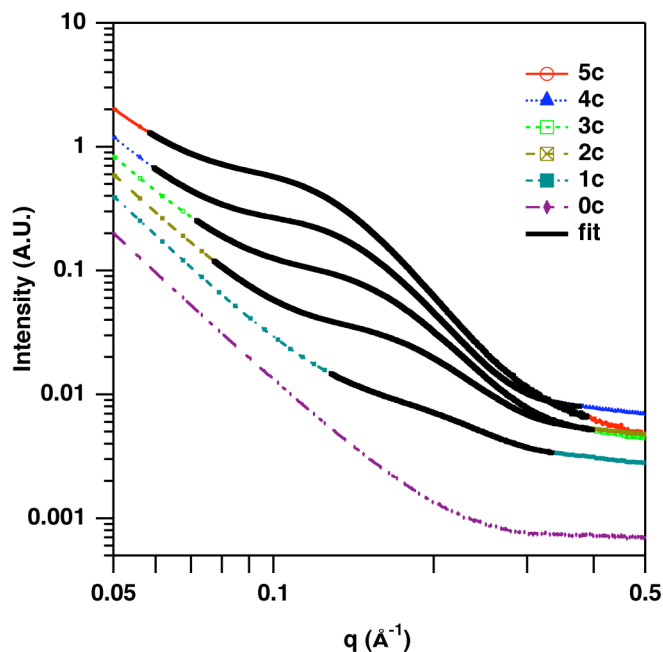


**Figure 6.3** SAXS data showing the interparticle scattering interference for the Pt nanoparticles. This leads to a peak from which the interparticle spacing can be derived by use of eq 6.1. The data show a dependence on the number of ALD cycles for the position of the peak, which has been fitted with a pseudo-Voigt function on a power-law background (black line). Data collected at 12ID-C, APS by Byeongdu Lee.

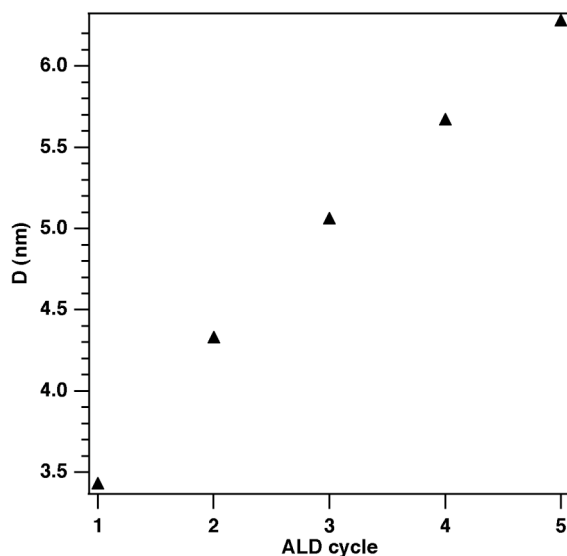


**Figure 6.4** The SAXS derived platinum interparticle spacing as a function of ALD cycles. The data points are derived from eq 6.1 and the peak fits shown in Fig. 6.3.



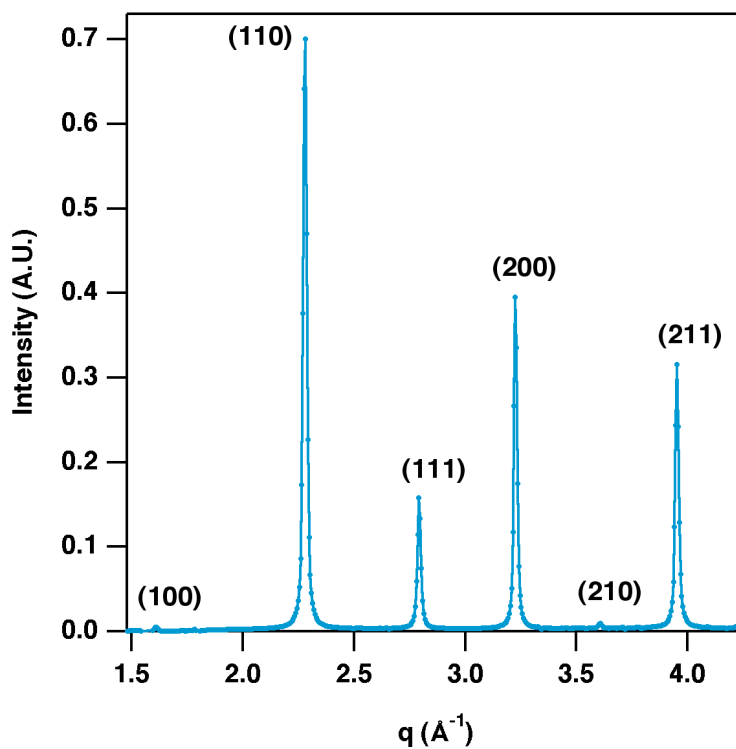


**Figure 6.5** WAXS data for uncoated SrTiO<sub>3</sub> nanocubes. The Bragg peaks have been indexed. The positions and relative intensities of the peaks are consistent with polycrystalline cubic-P SrTiO<sub>3</sub> with  $a = 3.90 \text{ \AA}$ . Data collected at 5ID-D, APS.

This compares to the ~60 nm nanoparticle size from microscopy and would indicate that the SrTiO<sub>3</sub> nanocubes are single crystals. Figure 6.6 shows the (111) WAXS peak for the 5 ALD cycle and blank SrTiO<sub>3</sub> cases where broadening due to the platinum nanoparticles can be observed. The peak shape was fit using a double Lorentzian function given by:

$$f(q) = A * \left[ \frac{(1-\phi)}{1 + \frac{q-q_1}{b_1^2}} + \frac{\phi}{1 + \frac{q-q_0}{b_0^2}} \right], \quad (6.3)$$

where  $A$  is a scaling parameter,  $\phi$  is a mixing parameter between the two Lorentzians, and  $q$  and  $b$  terms give the peak positions and widths, respectively. The domain size could then be determined using eq 6.2 and the  $2*b_0$  term for the *fwhm* of a Lorentzian. The broadening for the Pt (200) peaks was not as marked and consequently did not yield useful information. Figure 6.7 plots the crystallite size for the (111) peak for the 2 to 5 ALD cycles, which shows  $t_{111}$  increases from 1.0 to 2.7 nm and again shows a linear growth trend. The line width for the 1c case was too large to determine the particle size, but based on the linear regression for the other cases, the particles size would be ~0.7 nm.

### 6.4.3 X-ray absorption spectroscopy

X-ray absorption near-edge structure (XANES) in the set of X-ray absorption spectra (XAS) of Figure 6.8 indicate a change in the chemical state of the platinum as the number of ALD cycles changes. The normalized absorption cross sections of Fig. 6.8 include the five ALD cases, a platinum metal foil, and two platinum oxides: PtO and PtO<sub>2</sub>. The measured Pt L<sub>3</sub> absorption edges (relative to  $E_0 = 11564$  eV) are given in Table 6.1.

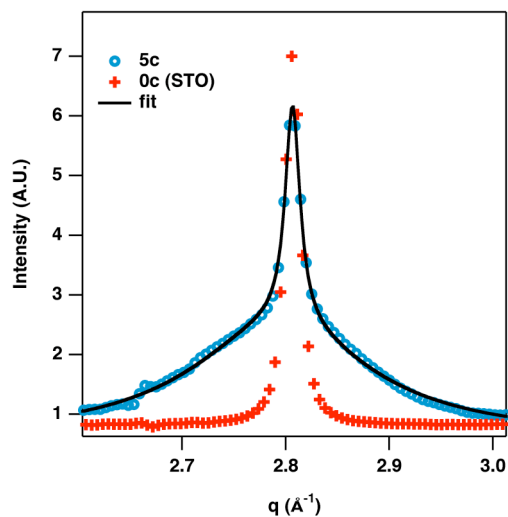


**Figure 6.6** Line broadening effects of the (111) diffraction peak due to the Pt nanoparticle size. An uncoated SrTiO<sub>3</sub> pattern has been overlaid to illustrate the effect. The broadening was fit with eq 6.3 to determine the crystallite size from the *fwhm* using eq 6.2. Data collected at 5ID-D, APS.

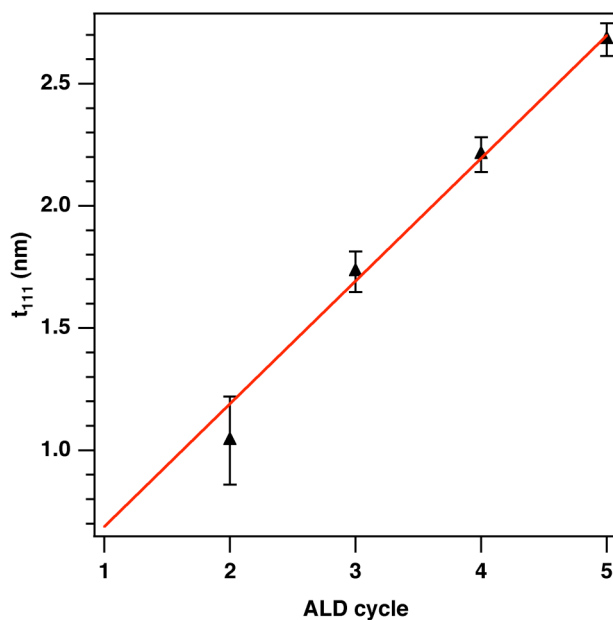


**Figure 6.7** The platinum crystallite size determined from line shape analysis of the WAXS data. (The 1 cycle case did not yield a Pt 111 measurable diffraction peak.) The linear growth trend is consistent with nanoparticle growth for ALD.

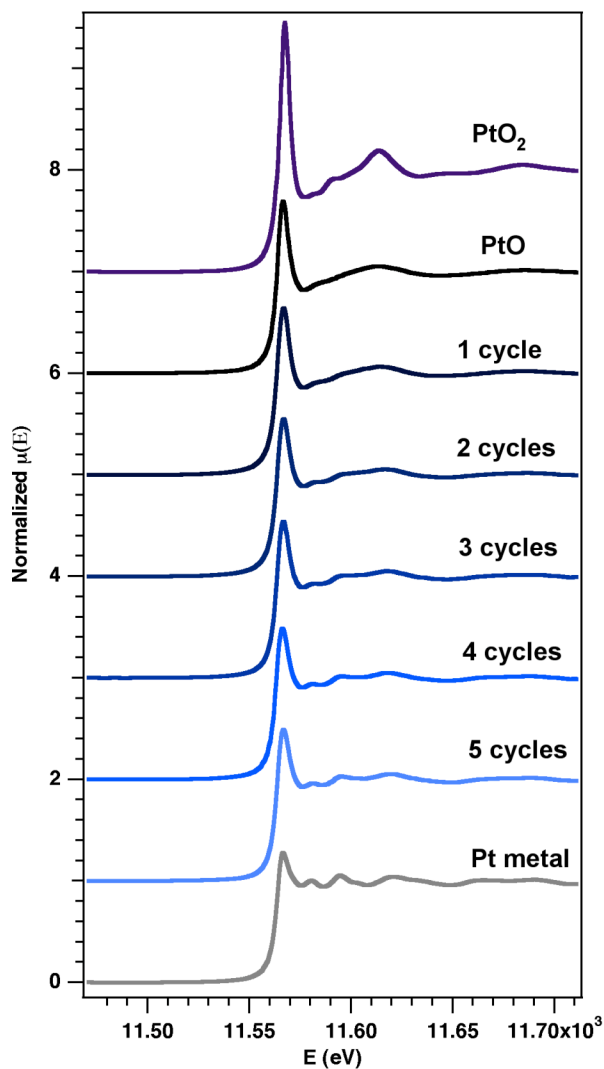


**Figure 6.8** The measured normalized X-ray absorption cross sections near the Pt L<sub>3</sub> edge for the ALD samples, a Pt foil reference, a platinum (II) oxide reference, and a platinum (IV) oxide reference. At one ALD cycle the platinum is in a similar state as platinum in PtO and as the number ALD cycles increases, the platinum chemical state becomes more bulk like. Data collected at the APS DND-CAT 5BM-D station.

Table 6.1: Pt L <sub>3</sub> edge shift ( $E_0 = 11564$ eV)	
Sample	$\Delta E$ (eV)
PtO <sub>2</sub>	+ 2
PtO	+ 1
1c	+ 1
2c	+ 1
3c	0
4c	0
5c	0
Pt foil	0

**Table 6.1** Pt L<sub>3</sub> edge shift,  $\Delta E$ . The shift in the absorption edge,  $E_0$ , is related to chemical state of the platinum.  $E_0$  is most often determined by the zero crossing of the second derivative for the peak in the absorption spectra. A positive shift in  $\Delta E$  for  $E_0$  to higher energies is indicative of the platinum being oxidized.

The 3c, 4c and 5c cases show no significant  $\Delta E$  shift in energy, whereas the 1c and 2c cases show a +1 eV shift, which is consistent with oxidized platinum. In addition to the edge position, the XANES region ( $-100 \text{ eV} < \Delta E < 40 \text{ eV}$ ) provides additional information regarding the chemical state of the Pt. The line shape of the 1c platinum XANES-sample compares favorably to that of PtO standard shown in Figure 6.8. The XANES then transitions to that of bulk metallic platinum as the number of cycles increase. In addition to the  $\Delta E$  shift from  $E_0$  mentioned above, the white line intensity increases as the number of ALD cycles decreases. The white line intensity in this case is proportional the  $d$ -electron density of states. An increase in the white line intensity indicates a decrease in the number of electrons in the  $d$ -orbital. A reduction of the  $d$ -electron density of states would be consistent with the oxidation of platinum. A linear combination fit of the XANES of the samples using the Pt and PtO XANES leads to the results given in Table 6.2. As the number of ALD cycles increases, the Pt – Pt bond increases from 10% to 57% at the expense of the Pt – O bond.

The Fourier transforms of the EXAFS region ( $40 \text{ eV} < \Delta E < 1000 \text{ eV}$ ) are plotted in Figure 6.9 for the various cases. Here the Pt – O bond is evident at 1c and steadily diminishes as the Pt – Pt bond becomes more prevalent. The Pt – Pt bond was fitted using the ARTEMIS program<sup>126130</sup> in  $R$ -space over a  $k$  range of  $8 - 13.95 \text{ \AA}^{-1}$  and a  $k$ -weight factor of  $k^2$ . The fitting results given in Table 6.3 show the effect of the platinum coverage, where the coordination ( $N_{Pt}$ ) and the Pt – Pt bond length ( $r_{Pt-Pt}$ ) increase with ALD cycle. The Pt coordination increases effectively from zero to 4.4 as the ALD cycles increase.

Table 6.2: XANES Linear Combination Fitting Results		
Sample	% Pt	% PtO
1c	10	90
2c	23	77
3c	35	65
4c	48	52
5c	57	43

**Table 6.2.** XANES linear combination fitting. The line shape of XANES spectra may be fit as a linear combination of reference spectra to give an estimate of the amount of a material with a given chemical state. The ALD data were fit with the spectra from a Pt foil and platinum (II) oxide.

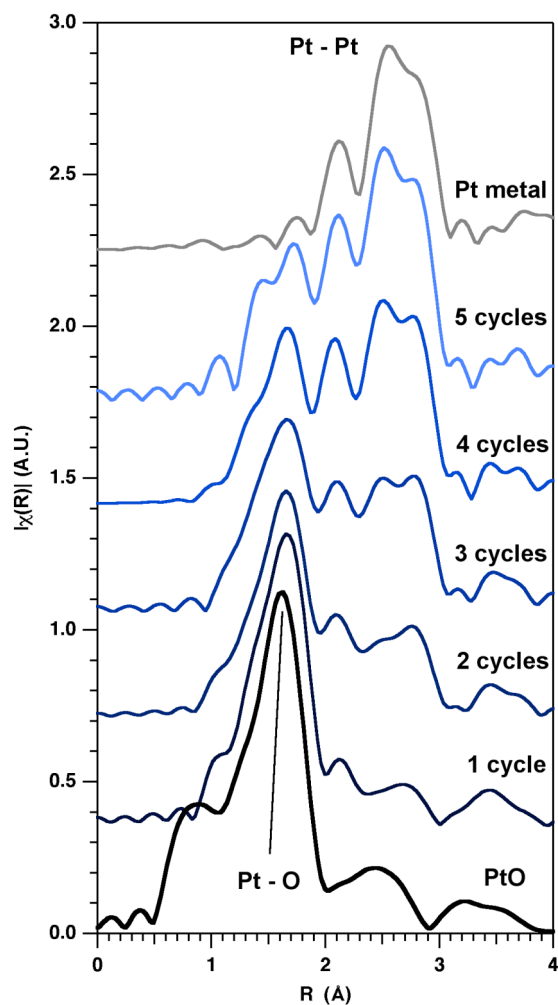


**Figure 6.9** Magnitude of the Fourier transform of the EXAFS for determining the Pt-Pt bonding and Pt-O bonding. As the number of ALD cycles increases, the Pt-O bond diminishes as the Pt-Pt bond increases.



Table 6.3: EXAFS fitting results of the Pt coordination and Pt – Pt bond length		
Sample	$N_{Pt}$	$r_{Pt-Pt}$ (Å)
1c	0.2	$2.70 \pm 0.05$
2c	1	$2.72 \pm 0.02$
3c	2.6	$2.74 \pm 0.01$
4c	3.7	$2.74 \pm 0.01$
5c	4.4	$2.75 \pm 0.01$
Pt foil	12	$2.76 \pm 0.01$

**Table 6.3** EXAFS fitting results giving the Pt-Pt bond length and approximated Pt coordination.

For the Pt – O bond, the best results were obtained with a slightly different fitting approach. Using the XANES linear combination results from Table 6.2, the fraction of the Pt foil spectrum was subtracted off the ALD spectra to yield a partial absorption cross section. The partial absorption cross section was then fitted using ARTEMIS to extract the Pt – O bond length for the various cases. The fitting for the Pt – O occurred over a  $k$  range of 3 – 7.8 Å<sup>-1</sup> and a  $k$  weight factor of  $k^1$ . For all cases, the Pt – O bond length was determined to be  $r_{\text{Pt-O}} = 1.98 \pm 0.03$  Å. The Pt – O bond length for a tetragonal PtO crystal structure<sup>28, 132</sup> is 2.04 Å with a coordination ( $N_{\text{PtO}}$ ) of 4. The Pt – O coordination from the data could not be obtained reliably.

### 6.5 Discussion of the Pt / nanocube results

The Pt clearly deposits as discrete nanoparticles (Fig. 6.2) rather than as a continuous layer. The nanoparticle size after 5 ALD cycles from both the SEM image and WAXS analysis is on the order of 3 nm. In concordance with this, the interparticle spacing from SAXS is also consistent with SEM. Taking the size and spacing into account, the platinum mass per area ( $\Theta$ ) can be calculated using the following relationship:

$$\Theta = \frac{V_p \rho}{D^2}, \quad (6.4)$$

where  $V_p$  is the particle volume and  $\rho$  is the buoyant density. For the case of 5 ALD cycles where the mean nanoparticle size,  $t_{111} = 3$  nm and mean center-to-center distance  $D = 6$  nm, a cube shaped particle at the bulk density of platinum (21.45 g cm<sup>-3</sup>) would give  $\Theta \sim 2 \times 10^{-3}$  mg cm<sup>-2</sup>. Recent reports indicated methanol based fuel cells need a Pt loading much less than 1 mg cm<sup>-2</sup> for economic justification.<sup>11, 14</sup> Furthermore, the nanoparticles of this size range are likely to show a size-property relationship related to their chemical activity.<sup>133, 134</sup>

The X-ray scattering data show that the Pt nanoparticle size and spacing correlates with ALD cycle. Consequently, the coordination, bond properties, and chemical state may be related to the size of the nanoparticle. The general trend would be then as the size decreases, the Pt – Pt bond length and coordination decreases. These phenomena have been observed for platinum<sup>3, 5</sup> and could be related to the particle size effect to catalytic activity as has been demonstrated with gold nanoparticles.<sup>4</sup> However, changes in platinum activity could be expected through a different mechanism as the Au study concluded an electron enrichment of the *d*-orbitals. For the ALD Pt, the white line intensity increases indicating that the *d*-orbitals are losing electrons. The XAS data for the ALD Pt does indeed suggest that the Pt is oxidized for at least one and two ALD cycles. The extent of the Pt oxidation may be understood by considering that the nanoparticle sizes are on the order of a nanometer or less. For such small particles, the lattice oxygen from the SrTiO<sub>3</sub> could be contributing significantly to the Pt - O bond detected by XAS.

To investigate the role of the lattice oxygen, consider the density functional theory (DFT) calculations for the Pt/SrTiO<sub>3</sub> (001) system.<sup>61</sup> The DFT modeling indicates that the Pt will prefer to bind to the lattice oxygen. The stability of the Pt/SrTiO<sub>3</sub> DFT structure improved as the Pt – O bond length approached ~ 2 Å. Furthermore, the DFT calculations expected a contraction of the Pt – O bond length as the Pt loading decreased. The EXAFS analysis indicated the Pt – O bond length to be 1.98±0.03 Å. The Pt – O bond length for crystalline platinum (II) oxide is also ~ 2 Å. Since there appears to be no systematic change in the ALD Pt – O bond that may link it directly to SrTiO<sub>3</sub> lattice oxygen, it is likely that the nanoparticles are oxidized through interaction with the environment. Along with the nanoparticle size, the platinum coordination decreases with ALD cycles. The nanoparticles are presumably more susceptible to oxidation

from the environment as their size decreases. The nanoparticles would then experience some oxidation when exposed to air upon removal from the reactor, which could be verified by some *in situ* spectroscopic measurement of the platinum chemical state during deposition and a systematic comparison to ALD platinum on non-oxide supports.

Oxidized platinum nanoparticles have not been widely reported on and consequently their structure-property relationships have not been explored. The implications of oxidizing the platinum may be interesting when considering specific oxidation/reduction catalysts for fuel cell architectures. However, the window to platinum oxidation in terms of process parameters is relatively narrow since at 5 ALD cycles, the nanoparticle chemical state is ~60% bulk platinum and generally follows a linear conversion trend. This is not surprising as the original work<sup>116, 117, 120</sup> on the MeCpPtMe<sub>3</sub> precursor found little to no platinum oxidation for steady-state growth regimes (> 200 ALD cycles). Thus, by simply changing the number of cycles in early growth regimes leads to appreciable changes in the chemical state, size, and dispersion of nanoparticles. Additional control of these properties could possibly be expanded by adjusting ALD process parameters such as the precursor pulse time or pressure.

## **6.6 Summary of ALD Pt / SrTiO<sub>3</sub> nanocubes**

The atomic layer deposition of platinum nanoparticles on cube-shaped strontium titanate nanoparticles has been investigated. Nanostructured materials of this nature offer some significant advantages for application in the fuel cell and catalyst fields. These advantages are tied to the nanoscale structure and morphology of the system. In accordance with this, the deposition at this length scale was characterized using electron microscopy, small-angle X-ray scattering, and X-ray absorption spectroscopy. Depending on the number of ALD cycles, the

platinum nanoparticles range in sizes from  $\sim 0.7 - 2.7$  nm and are well dispersed on the support. The loading of the platinum is extremely efficient,  $\sim 10^{-3}$  mg cm $^{-2}$ . The nanoparticles also show a Pt – Pt bond contraction and a tendency to become oxidized as the number of ALD cycles decreases. The oxidation most likely occurs through the environment as the material is removed from the reactor. These results are expected to be applicable to the nucleation of nanoparticles for other noble metals using ALD.

## Chapter 7: Concluding remarks

### 7.1 Conclusion

Catalysis continues to be an area where processes occurring at the nanometer length scale have a defining technological impact for society in the modern era. This dissertation examines an integral aspect of heterogeneous catalysis, namely the nucleation and growth of supported nanoparticles primarily in terms of the nanoscale morphology. Investigating catalytic materials at this length scale is essential to developing the next generation of catalysts using novel synthesis techniques. Key issues related to the nucleation and growth of catalytic nanoparticles includes the size, dispersion, and chemical state. From a materials science perspective, these issues will impact the catalytic properties the nanoparticles exhibit and the performance they yield as a function of their morphology. This dissertation may now be evaluated under these terms.

Chapter 4 gives an example where the size and dispersion of the nanoparticles are investigated in an extreme case. To summarize, the AFM data showed nanoparticles on the order of few tens of nanometers being separated by ten times that amount. The GISAXS confirmed this through Guinier analysis, but also showed a nanostructure of a finer nature. This conclusion was supported by the XRF coverage indicating that the amount of platinum was insufficient to interpret the GISAXS fitting directly. The most reasonable model consisted of the morphology observed previously using TEM where platinum nanoparticles have aggregated without coalescence. This behavior of platinum nanoparticles offers insight into achieving extremely high surface areas since extremely small particles ( $\sim 2$  nm) appear to be stable. By applying the results of the XAS data presented in Chapter 6, the platinum nanoparticles from PVD are likely

to be similar to bulk platinum in terms of oxidation state as they do not approach  $\sim 1$  nm in size. The Pt loading for this case is on the order of a monolayer, which is approaching the levels for economic viability of fuel cells.<sup>14</sup> The major issue preventing PVD for application in technological aspects would be the lack of ability to uniformly coat complex surfaces.

The nanoparticles deposited by atomic layer deposition from Chapters 5 and 6 may also be assessed in terms of their morphology. To summarize these chapters, the nanoparticles nucleate on both single crystal substrates and nanocube in a uniform manner where the size, dispersion and chemical nature depends on the number of ALD cycles. The growth rate for platinum on SrTiO<sub>3</sub> was higher than expected until the film coalesced and steady state ALD growth could occur. The growth mechanism for Pt nanoparticles involved both atomic diffusion and vapor deposition on the growing nanoparticle. The platinum was shown to take on a bulk metallic state in the range of 3 – 5 ALD cycles. For 1 – 2 ALD cycles, the  $\sim 1$  nm platinum nanoparticles were oxidized by the environment. The platinum loading was exceptionally clean and economic. As described previously, ALD offers significant opportunities for scale up as it can coat complex geometries common to industrial applications.

The results provided from this project are intended to provide a pathway for those in the catalyst community to develop the next generation of catalysts. This work offers a detailed understanding of the morphology such as size and dispersion as well as the chemical state that can be obtained for the desired application. Consequently, the catalytic activity may be evaluated in terms beyond the surface concentration of the catalyst to include variables such as the nanoparticle size or dispersion. Furthermore, this work provides valuable information on the emerging field of catalyst synthesis via atomic layer deposition. Indeed, ALD has demonstrated

the ability to nucleate nanoparticles in a clean, efficient, and precise manner.

Finally, another major goal attempted in this work is to motivate the combination of imaging and X-ray techniques, particularly AFM and GISAXS. This work clearly demonstrates that without both imaging and structural probes, an incomplete characterization of the system may result. Consequently, this would have limited the ability to realize new opportunities in catalyst development. Such opportunities are also better served by these nondestructive characterization methods, which can operate in a variety of environments. Furthermore, the ease of and availability of AFM can greatly facilitate the productivity of synchrotron experiments, not to mention the aid AFM provides in the data interpretation. At the synchrotron, GISAXS can extend the AFM results by providing the ability to perform catalytic experiments *in situ* and to integrate with other X-ray techniques such as absorption spectroscopy. Thus, it is hopeful that the principles demonstrated in this work may lead to similar efforts for future catalysis research opportunities.

## 7.2 Outlook

The primary focus of moving this work forward involves testing the catalytic performance of the various Pt/SrTiO<sub>3</sub> morphologies studied herein. As noted by some of the original researchers on Pt/SrTiO<sub>3</sub>, the photocatalytic activity improved as the platinum film decreased in thickness.<sup>72</sup> This observation in part motivated this work because at the time it was published, many of the principal techniques used in the study were not available. Catalytic measurements open the door to optimization and improvement of PVD and ALD as tools for catalyst synthesis through the identification of key structure-property relationships.

Ref. [72] offers a starting point for photocatalytic measurements as hydrogen production



was studied from platinum films on single-crystal SrTiO<sub>3</sub> substrates. Both the PVD and ALD SrTiO<sub>3</sub> (001) samples could be compared against the results of Ref. [72]. Reaction studies on the single crystal samples prepared during this project would elucidate the relationship between the catalytic performance and the morphology. Catalytic performance can thus be understood through direct knowledge of nanoparticle size, spacing, and chemical state. Furthermore, the impact of the photocatalysis on the morphology could also be gauged to determine morphological stability under photocatalytic reaction conditions.

Researchers at Argonne National laboratory performed catalytic measurements on Pt/SrTiO<sub>3</sub> nanocubes that yielded some interesting results regarding propane combustion. The system appears to show an improvement in reducing the activation temperature for complete propane combustion. In general, this translates into better energy efficiency and interesting opportunities for pollution control. However, the major issue remaining is to determine the novelty of the support versus the ALD catalyst. This would provide the opportunity to understand how the SrTiO<sub>3</sub> nanocube may affect the catalyst performance when compared to other forms of SrTiO<sub>3</sub> and other support materials altogether. In addition to catalysis testing, the experiments would need to include microscopy, SAXS, and XAS measurements for the new support materials. These experiments would not be difficult to conduct and would provide a path to develop a new generation of pollution control catalysts for application in the automotive and industrial sectors.

To make the catalytic measurements more meaningful, specific parameters may be tested regarding the PVD and ALD techniques. In the case of the PVD study, a broader exploration of the platinum coverage may be considered. TEM images from Ref. [8] indicate that the Pt

aggregation was in part a function of the platinum coverage and they showed situations where the small Pt nanoparticles completely cover the substrate without coalescence. Often increasing the catalyst coverage leads to catalytic poisoning due to nanoparticle coalescence. However, the resistance of the platinum nanoparticles to coalescence may allow for increased platinum loading without a loss in activity. Small-angle scattering experiments could be conducted to model the attractive/repulsive potential described in Ref. [10] as the mechanism for the resistance of Pt nanoparticles to coalescence. In addition, more structural/morphological studies are warranted to investigate the behavior in similar materials such as palladium, nickel, etc. A good figure of merit to consider in investigating other materials for similar behavior is the melting point. Platinum has a relatively high melting point while materials with lower melting points, such as gold and indium, showed coalescence.

As for atomic layer deposition, many opportunities lie untested. One major prospect would be to perform systematic studies on parameters such as the pulse time in the ALD cycle and precursor pressure. These two parameters will significantly impact the catalyst loading and consequently the size, dispersion, and chemical state of the nanoparticles. ALD also affords significant opportunities in catalyst architecture such as core-shell structures, alloy catalysts, and schemes to structurally inhibit nanoparticle sintering and catalytic poisoning. Since ALD could be a viable technique for scale up, additional cost-benefit analyses are required. The major obstacles to bringing ALD out of the laboratory and into industry include the cost and availability of ALD precursors on an industrial scale as well as the cost of building and maintaining large ALD reactors. ALD catalysts must then offer significant improvements to catalytic performance to outweigh the costs. This is an extremely interesting question to answer

from a research perspective and will likely motivate more work in this area.

In closing, the significant attention energy related issues currently receive offers considerable opportunity to the research community to provide more solutions to energy production, security, and efficiency. In a small way, this dissertation serves as a prelude to the prospects ALD and PVD catalysts may offer to such energy solutions.

## 8. REFERENCES

- [1] Dresselhaus, M. S. and Thomas, I. L., Alternative energy technologies. *Nature* 2001, 414, (6861), 332-337.
- [2] Bell, A. T., The impact of nanoscience on heterogeneous catalysis. *Science* 2003, 299, (5613), 1688-1691.
- [3] Klimenkov, M., Nepijko, S., Kuhlbeck, H., Baumer, M., Schlogl, R. and Freund, H. J., The structure of Pt-aggregates on a supported thin aluminum oxide film in comparison with unsupported alumina: a transmission electron microscopy study. *Surface Science* 1997, 391, (1-3), 27-36.
- [4] Miller, J. T., Kropf, A. J., Zha, Y., Regalbuto, J. R., Delannoy, L., Louis, C., Bus, E. and van Bokhoven, J. A., The effect of gold particle size on Au-Au bond length and reactivity toward oxygen in supported catalysts. *Journal of Catalysis* 2006, 240, (2), 222-234.
- [5] Oudenhuijzen, M. K., Bitter, J. H. and Koningsberger, D. C., The nature of the Pt-H bonding for strongly and weakly bonded hydrogen on platinum. A XAFS spectroscopy study of the Pt-H antibonding shape resonance and Pt-H EXAFS. *Journal of Physical Chemistry B* 2001, 105, (20), 4616-4622.
- [6] Alayoglu, S., Nilekar, A. U., Mavrikakis, M. and Eichhorn, B., Ru-Pt core-shell nanoparticles for preferential oxidation of carbon monoxide in hydrogen. *Nature Materials* 2008, 7, (4), 333-338.
- [7] Habas, S. E., Lee, H., Radmilovic, V., Somorjai, G. A. and Yang, P., Shaping binary metal nanocrystals through epitaxial seeded growth. *Nature Materials* 2007, 6, (9), 692-697.
- [8] Alayan, R., Arnaud, L., Broyer, M., Cottancin, E., Lerme, J., Marhaba, S., Vialle, J. L. and Pellarin, M., Organization of size-selected platinum and indium clusters soft-landed on surfaces. *Physical Review B* 2007, 76, (7), 075424.
- [9] Stappert, S., Rellinghaus, B., Acet, M. and Wassermann, E. F., Gas-phase preparation of L1(0) ordered FePt nanoparticles. *Journal of Crystal Growth* 2003, 252, (1-3), 440-450.

- [10] Tainoff, D., Bardotti, L., Tournus, F., Guiraud, G., Boisson, O. and Melinon, P., Self-organization of size-selected bare platinum nanoclusters: Toward ultra-dense catalytic systems. *Journal of Physical Chemistry C* 2008, 112, (17), 6842-6849.
- [11] King, J. S., Wittstock, A., Biener, J., Kucheyev, S. O., Wang, Y. M., Baumann, T. F., Giri, S. K., Hamza, A. V., Baeumer, M. and Bent, S. F., Ultralow loading Pt nanocatalysts prepared by atomic layer deposition on carbon aerogels. *Nano Letters* 2008, 8, (8), 2405-2409.
- [12] Elam, J. W., Libera, J. A., Pellin, M. J., Zinovev, A. V., Greene, J. P. and Nolen, J. A., Atomic layer deposition of W on nanoporous carbon aerogels. *Applied Physics Letters* 2006, 89, (5), 053124.
- [13] Johansson, A., Lu, J., Carlsson, J. O. and Boman, M., Deposition of palladium nanoparticles on the pore walls of anodic alumina using sequential electroless deposition. *Journal of Applied Physics* 2004, 96, (9), 5189-5194.
- [14] Liu, H. S., Song, C. J., Zhang, L., Zhang, J. J., Wang, H. J. and Wilkinson, D. P., A review of anode catalysis in the direct methanol fuel cell. *Journal of Power Sources* 2006, 155, (2), 95-110.
- [15] Greeley, J. and Mavrikakis, M., Alloy catalysts designed from first principles. *Nature Materials* 2004, 3, (11), 810-815.
- [16] Binnig, G., Quate, C. F. and Gerber, C., Atomic force microscope. *Physical Review Letters* 1986, 56, (9), 930-933.
- [17] Levine, J. R., Cohen, L. B., Chung, Y. W. and Georgopoulos, P., Grazing-Incidence Small-Angle X-Ray-Scattering - New Tool for Studying Thin-Film Growth. *Journal of Applied Crystallography* 1989, 22, 528-532.
- [18] Vanrheenen, P. R., Mckelvy, M. J. and Glaunsinger, W. S., Synthesis and Characterization of Small Platinum Particles Formed by the Chemical-Reduction of Chloroplatinic Acid. *Journal of Solid State Chemistry* 1987, 67, (1), 151-169.
- [19] Henry, C. R., Surface studies of supported model catalysts. *Surface Science Reports* 1998, 31, (7-8), 235-325.

- [20] Henry, C. R., Morphology of supported nanoparticles. *Progress in Surface Science* 2005, 80, 92-116.
- [21] Mao, Y. B., Banerjee, S. and Wong, S. S., Large-scale synthesis of single-crystal line perovskite nanostructures. *Journal of the American Chemical Society* 2003, 125, (51), 15718-15719.
- [22] Rabuffetti, F. A., Kim, H.-S., Enterkin, J. A., Wang, Y., Lanier, C. H., Marks, L. D., Poeppelmeier, K. R. and Stair, P. C., Synthesis-Dependent First-Order Raman Scattering in SrTiO<sub>3</sub> Nanocubes at Room Temperature. *Chemistry of Materials* 2008, 20, (17), 5628 - 5635.
- [23] Dunn, P. J., Chao, G. Y., Fleischer, M., Ferraiolo, J. A., Langley, R. H., Pabst, A. and Zilczer, J. A., New mineral names. *American Mineralogist* 1985, 70, 214-221.
- [24] Merker, L. and Lynd, L. E. U.S. Patent Office, U. S. P.2626156 1953.
- [25] Erdman, N. and Marks, L. D., SrTiO<sub>3</sub>(001) surface structures under oxidizing conditions. *Surface Science* 2003, 526, (1-2), 107-114.
- [26] Erdman, N., Poeppelmeier, K. R., Asta, M., Warschkow, O., Ellis, D. E. and Marks, L. D., The structure and chemistry of the TiO<sub>2</sub>-rich surface of SrTiO<sub>3</sub>(001). *Nature* 2002, 419, (6902), 55-58.
- [27] Jiang, Q. D. and Zegenhagen, J., SrTiO<sub>3</sub> (001) Surfaces and Growth of Ultra-Thin GdBa<sub>2</sub>Cu<sub>3</sub>O<sub>7-x</sub> Films Studied by LEED/AES and UHV-STM. *Surface Science* 1995, 338, (1-3), L882-L888.
- [28] Jiang, Q. D. and Zegenhagen, J., SrTiO<sub>3</sub>(001)-c(6x2): A long-range, atomically ordered surface stable in oxygen and ambient air. *Surface Science* 1996, 367, (2), L42-L46.
- [29] Jiang, Q. D. and Zegenhagen, J., c(6x2)and c(4x2)reconstruction of SrTiO<sub>3</sub> (001). *Surface Science* 1999, 425, (2-3), 343-354.
- [30] Kubo, T. and Nozoye, H., Surface structure of SrTiO<sub>3</sub>(100). *Surface Science* 2003, 542, (3), 177-191.

- [31] Naito, M. and Sato, H., Reflection High-Energy Electron-Diffraction Study on the SrTiO<sub>3</sub> Surface-Structure. *Physica C* 1994, 229, (1-2), 1-11.
- [32] Kawasaki, M., Takahashi, K., Maeda, T., Tsuchiya, R., Shinohara, M., Ishiyama, O., Yonezawa, T., Yoshimoto, M. and Koinuma, H., Atomic Control of the SrTiO<sub>3</sub> Crystal-Surface. *Science* 1994, 266, (5190), 1540-1542.
- [33] Ishiyama, O., Nishihara, T., Hayashi, S., Shinohara, M., Yoshimoto, M., Ohnishi, T., Koinuma, H., Nishino, S. and Saraie, J., Atomic scale identification of the terminating structure of compound materials by CAICISS (coaxial impact collision ion scattering spectroscopy). *Applied Surface Science* 1997, 121, 163-166.
- [34] Nakamura, T., Inada, H. and Iiyama, M., In situ surface characterization of SrTiO<sub>3</sub>(100) substrates for well-defined SrTiO<sub>3</sub> and YBa<sub>2</sub>Cu<sub>3</sub>O<sub>7-x</sub> thin film growth. *Japanese Journal of Applied Physics Part 1-Regular Papers Short Notes & Review Papers* 1997, 36, (1A), 90-93.
- [35] Nishimura, T., Ikeda, A., Namba, H., Morishita, T. and Kido, Y., Structure change of TiO<sub>2</sub>-terminated SrTiO<sub>3</sub>(001) surfaces by annealing in O<sub>2</sub> atmosphere and ultrahigh vacuum. *Surface Science* 1999, 421, (3), 273-278.
- [36] Yoshimoto, M., Maeda, T., Shimozone, K., Koinuma, H., Shinohara, M., Ishiyama, O. and Ohtani, F., Topmost surface analysis of SrTiO<sub>3</sub>(001) by coaxial impact-collision ion-scattering spectroscopy. *Applied Physics Letters* 1994, 65, (25), 3197-3199.
- [37] Castell, M. R., Scanning tunneling microscopy of reconstructions on the SrTiO<sub>3</sub>(001) surface. *Surface Science* 2002, 505, (1-3), 1-13.
- [38] Castell, M. R., Nanostructures on the SrTiO<sub>3</sub> (001) Surface studied by STM. *Surface Science* 2002, 516, 33-42.
- [39] Erdman, N., Warschkow, O., Asta, M., Poepelmeier, K. R., Ellis, D. E. and Marks, L. D., Surface structures of SrTiO<sub>3</sub> (001): A TiO<sub>2</sub>-rich reconstruction with a c(4 x 2) unit cell. *Journal of the American Chemical Society* 2003, 125, (33), 10050-10056.
- [40] Hikita, T., Hanada, T., Kudo, M. and Kawai, M., Structure and Electronic State of the TiO<sub>2</sub> and SrO Terminated SrTiO<sub>3</sub>(100) Surfaces. *Surface Science* 1993, 287, 377-381.

- [41] Liang, Y. and Bonnell, D. a., Atomic Structures of Reduced SrTiO<sub>3</sub>(001) Surfaces. *Surface Science* 1993, 285, (3), L510-L516.
- [42] van der Heide, P. A. W., Jiang, Q. D., Kim, Y. S. and Rabalais, J. W., X-ray photoelectron spectroscopic and ion scattering study of the SrTiO<sub>3</sub>(001) surface. *Surface Science* 2001, 473, (1-2), 59-70.
- [43] Szot, K. and Speier, W., Surfaces of reduced and oxidized SrTiO<sub>3</sub> from atomic force microscopy. *Physical Review B* 1999, 60, (8), 5909-5926.
- [44] Ruddlesden, S. N. and Popper, P., The Compound Sr<sub>3</sub>Ti<sub>2</sub>O<sub>7</sub> and Its Structure. *Acta Crystallographica* 1958, 11, (1), 54-55.
- [45] Fompeyrine, J., Berger, R., Lang, H. P., Perret, J., Machler, E., Gerber, C. and Locquet, J. P., Local determination of the stacking sequence of layered materials. *Applied Physics Letters* 1998, 72, (14), 1697-1699.
- [46] Koster, G., Rijnders, G., Blank, D. H. A. and Rogalla, H., Surface morphology determined by (001) single-crystal SrTiO<sub>3</sub> termination. *Physica C-Superconductivity and Its Applications* 2000, 339, (4), 215-230.
- [47] Greene, M. E., Chiamonti, A. N., Christensen, S. T., Cao, L. X., Bedzyk, M. J. and Hersam, M. C., Controlled nanoscale morphology of hematite (0001) surfaces grown by chemical vapor transport. *Advanced Materials* 2005, 17, (14), 1765.
- [48] Marchenko, V. I., Possible Structures and Phase-Transitions on the Surface of Crystals. *Jetp Letters* 1981, 33, (8), 381-383.
- [49] Ng, K. O. and Vanderbilt, D., Stability of Periodic Domain-Structures in a 2-Dimensional Dipolar Model. *Physical Review B* 1995, 52, (3), 2177-2183.
- [50] Hannon, J. B., Heringdorf, F. J. M. Z., Tersoff, J. and Tromp, R. M., Phase coexistence during surface phase transitions. *Physical Review Letters* 2001, 86, (21), 4871-4874.
- [51] Hannon, J. B., Tersoff, J. and Tromp, R. M., Surface stress and thermodynamic nanoscale size selection. *Science* 2002, 295, (5553), 299-301.



- [52] Plass, R., Last, J. A., Bartelt, N. C. and Kellogg, G. L., Nanostructures - Self-assembled domain patterns. *Nature* 2001, 412, (6850), 875-875.
- [53] Cord, B. and Courths, R., Electronic study of SrTiO<sub>3</sub>(001) surfaces by photoemission. *Surface Science* 1985, 162, (1-3), 34-38.
- [54] Tanaka, H., Matsumoto, T., Kawai, T. and Kawai, S., Surface structure and Electronic Property of Reduced SrTiO<sub>3</sub>(100) Surface Observed by Scanning Tunneling Microscopy Spectroscopy. *Japanese Journal of Applied Physics Part 1-Regular Papers Short Notes & Review Papers* 1993, 32, (3B), 1405-1409.
- [55] Azad, S., Engelhard, M. H. and Wang, L. Q., Adsorption and reaction of CO and CO<sub>2</sub> on oxidized and reduced SrTiO<sub>3</sub>(100) surfaces. *Journal Of Physical Chemistry B* 2005, 109, (20), 10327-10331.
- [56] Azad, S., Szanyi, J., Peden, C. H. F. and Wang, L. Q., Adsorption and reaction of NO on oxidized and reduced SrTiO<sub>3</sub>(100) surfaces. *Journal Of Vacuum Science & Technology A* 2003, 21, (4), 1307-1311.
- [57] Giocondi, J. L. and Rohrer, G. S., Structure sensitivity of photochemical oxidation and reduction reactions on SrTiO<sub>3</sub> surfaces. *Journal Of The American Ceramic Society* 2003, 86, (7), 1182-1189.
- [58] Matsumoto, Y., Ohsawa, T., Takahashi, R. and Koinuma, H., Surface termination effect on the photocatalysis on atomically controlled SrTiO<sub>3</sub>(001) surface. *Thin Solid Films* 2005, 486, (1-2), 11-14.
- [59] Ohsawa, T., Matsumoto, Y. and Koinuma, H., Photochemical identification of a possible adsorbed pentacene molecule on the SrTiO<sub>3</sub>(001). *Japanese Journal Of Applied Physics Part 1-Regular Papers Short Notes & Review Papers* 2005, 44, (6A), 4142-4144.
- [60] Linsebigler, A. L., Lu, G. Q. and Yates, J. T., Photocatalysis on TiO<sub>2</sub> Surfaces - Principles, Mechanisms, and Selected Results. *Chemical Reviews* 1995, 95, (3), 735-758.
- [61] Asthagiri, A. and Sholl, D. S., First principles study of Pt adhesion and growth on SrO- and TiO<sub>2</sub>-terminated SrTiO<sub>3</sub>(100). *Journal of Chemical Physics* 2002, 116, (22), 9914-9925.

- [62] Asthagiri, A. and Sholl, D. S., DFT study of Pt adsorption on low index SrTiO<sub>3</sub> surfaces: SrTiO<sub>3</sub>(100), SrTiO<sub>3</sub>(111) and SrTiO<sub>3</sub>(110). *Surface Science* 2005, 581, (1), 66-87.
- [63] Polli, A. D., Wagner, T., Gemming, T. and Ruhle, M., Growth of platinum on TiO<sub>2</sub>- and SrO-terminated SrTiO<sub>3</sub>(100). *Surface Science* 2000, 448, (2-3), 279-289.
- [64] Francis, A. J. and Salvador, P. A., Crystal orientation and surface morphology of face-centered-cubic metal thin films deposited upon single-crystal ceramic substrates using pulsed laser deposition. *Journal of Materials Research* 2007, 22, (1), 89-102.
- [65] Wagner, T., Polli, A. D., Richter, G. and Stanzick, H., Epitaxial growth of metals on (100) SrTiO<sub>3</sub>: The influence of lattice mismatch and reactivity. *Zeitschrift Fur Metallkunde* 2001, 92, (7), 701-706.
- [66] Iddir, H., Komanicky, V., Ogut, S., You, H. and Zapol, P., Shape of platinum nanoparticles supported on SrTiO<sub>3</sub>: Experiment and theory. *Journal of Physical Chemistry C* 2007, 111, (40), 14782-14789.
- [67] Wrighton, M. S., Ellis, a. B., Wolczanski, P. T., Morse, D. L., Abrahamson, H. B. and Ginley, D. S., Strontium titanate photoelectrodes - efficient photoassisted electrolysis of water at zero applied potential. *Journal of The American Chemical Society* 1976, 98, (10), 2774-2779.
- [68] Wrighton, M. S., Wolczanski, P. T. and Ellis, A. B., Photoelectrolysis of water by irradiation of platinized n-type semiconducting metal oxides. *Journal of Solid State Chemistry* 1977, 22, (1), 17-29.
- [69] Wagner, F. T., Ferrer, S. and Somorjai, G. A., Photocatalytic hydrogen production from water over SrTiO<sub>3</sub> crystal surfaces, electron-spectroscopy studies of adsorbed H<sub>2</sub>, O<sub>2</sub> And H<sub>2</sub>O. *Surface Science* 1980, 101, (1-3), 462-474.
- [70] Wagner, F. T. and Somorjai, G. A., Photocatalytic and photoelectrochemical hydrogen production on strontium titanate single crystals. *Journal Of The American Chemical Society* 1980, 102, (17), 5494-5502.
- [71] Wagner, F. T. and Somorjai, G. A., Photocatalytic hydrogen production from water on Pt-free SrTiO<sub>3</sub> in alkali hydroxide solutions. *Nature* 1980, 285, (5766), 559-560.

- [72] Carr, R. G. and Somorjai, G. A., Hydrogen production from photolysis of steam adsorbed onto platinized SrTiO<sub>3</sub>. *Nature* 1981, 290, (5807), 576-577.
- [73] Domen, K., Kudo, A., Onishi, T., Kosugi, N. and Kuroda, H., Photocatalytic decomposition of water into H<sub>2</sub> and O<sub>2</sub> over NiO-SrTiO<sub>3</sub> powder. 1. Structure of the catalyst. *Journal Of Physical Chemistry* 1986, 90, (2), 292-295.
- [74] Domen, K., Naito, S., Onishi, T. and Tamaru, K., Photocatalytic decomposition of liquid water on a NiO SrTiO<sub>3</sub> catalyst. *Chemical Physics Letters* 1982, 92, (4), 433-434.
- [75] Domen, K., Naito, S., Onishi, T. and Tamaru, K., Study of the photocatalytic decomposition of water-vapor over a NiO-SrTiO<sub>3</sub> catalyst. *Journal Of Physical Chemistry* 1982, 86, (18), 3657-3661.
- [76] Domen, K., Naito, S., Soma, M., Onishi, T. and Tamaru, K., Photocatalytic decomposition of water vapor on an NiO-SrTiO<sub>3</sub> catalyst. *Journal Of The Chemical Society-Chemical Communications* 1980, (12), 543-544.
- [77] Maeda, K., Teramura, K., Lu, D. L., Takata, T., Saito, N., Inoue, Y. and Domen, K., Photocatalyst releasing hydrogen from water - Enhancing catalytic performance holds promise for hydrogen production by water splitting in sunlight. *Nature* 2006, 440, (7082), 295-295.
- [78] Aurian-Blajeni, B., Halmann, M. and Manassen, J., Photoreduction of carbon dioxide and water into formaldehyde and methanol on semiconductor materials. *Solar Energy* 1980, 25, (2), 165-170.
- [79] Tinnemans, A. H. A., Koster, T. P. M., Thewissen, D. H. M. W. and Mackor, A., Formation of Methanol and Other C-1-C-3 Compounds in the Photoassisted Reaction of Formaldehyde and Water over Strontium-Titanate Suspensions Containing Transition-Metal Oxide Deposits. *Nouveau Journal De Chimie-New Journal of Chemistry* 1982, 6, (7-8), 373-379.
- [80] Jia, J. F., Tanabe, E., Wang, P., Ito, K., Morioka, H., Wang, Y., Shishido, T. and Takehira, K., Study on the anti-coking nature of Ni/SrTiO<sub>3</sub> catalysts by the CH<sub>4</sub> pyrolysis. *Catalysis Letters* 2001, 76, (3-4), 183-192.

- [81] Takehira, K., Shishido, T. and Kondo, M., Partial oxidation of CH<sub>4</sub> over Ni/SrTiO<sub>3</sub> catalysts prepared by a solid-phase crystallization method. *Journal Of Catalysis* 2002, 207, (2), 307-316.
- [82] Urasaki, K., Sekine, Y., Kawabe, S., Kikuchi, E. and Matsukata, M., Catalytic activities and coking resistance of Ni/perovskites in steam reforming of methane. *Applied Catalysis A-General* 2005, 286, (1), 23-29.
- [83] Urasaki, K., Tokunaga, K., Sekine, Y., Kikuchi, E. and Matsukata, M., Hydrogen production by steam reforming of ethanol using cobalt and nickel catalysts supported on strontium titanate. *Chemistry Letters* 2005, 34, (5), 668-669.
- [84] Basu, R., Lin, J. C., Kim, C. Y., Schmitz, M. J., Yoder, N. L., Kellar, J. A., Bedzyk, M. J. and Hersam, M. C., Structural characterization of 4-bromostyrene self-assembled monolayers on Si(111). *Langmuir* 2007, 23, (4), 1905-1911.
- [85] Jin, H., Kinser, C. R., Bertin, P. A., Kramer, D. E., Libera, J. A., Hersam, M. C., Nguyen, S. T. and Bedzyk, M. J., X-ray studies of self-assembled organic monolayers grown on hydrogen-terminated Si(III). *Langmuir* 2004, 20, (15), 6252-6258.
- [86] Schmidbauer, M., Wiebach, T., Raidt, H., Hanke, M., Kohler, R. and Wawra, H., Ordering of self-assembled Si<sub>1-x</sub>Ge<sub>x</sub> islands studied by grazing incidence small-angle x-ray scattering and atomic force microscopy. *Physical Review B* 1998, 58, (16), 10523-10531.
- [87] Kazimirov, A., Goodner, D. M., Bedzyk, M. J., Bai, J. and Hubbard, C. R., X-ray surface diffraction analysis of structural transformations on the (001) surface of oxidized SrTiO<sub>3</sub>. *Surface Science* 2001, 492, (1-2), L711-L716.
- [88] Kim, C. Y., Elam, J. W., Pellin, M. J., Goswami, D. K., Christensen, S. T., Hersam, M. C., Stair, P. C. and Bedzyk, M. J., Imaging of atomic layer deposited (ALD) tungsten monolayers on alpha-TiO<sub>2</sub>(110) by X-ray standing wave Fourier inversion. *Journal of Physical Chemistry B* 2006, 110, (25), 12616-12620.
- [89] Guinier, A., Fournet, G., *Small-Angle Scattering of X-rays*. John Wiley & Sons: New York, 1955.
- [90] Glatter, O. and Kratky, O., *Small Angle X-ray Scattering*. Academic Press: London, 1982.

- [91] Lazzari, R., IsGISAXS: a program for grazing-incidence small-angle X-ray scattering analysis of supported islands. *Journal of Applied Crystallography* 2002, 35, 406-421.
- [92] Roe, R. J., *Methods of X-ray and neutron scattering in polymer science*. Oxford University Press: New York, 2000.
- [93] Lazzari, R., Leroy, F. and Renaud, G., Grazing-incidence small-angle x-ray scattering from dense packing of islands on surfaces: Development of distorted wave Born approximation and correlation between particle sizes and spacing. *Physical Review B* 2007, 76, (12), 125411.
- [94] Rauscher, M., Salditt, T. and Spohn, H., Small-angle x-ray scattering under grazing incidence: The cross section in the distorted-wave Born approximation. *Physical Review B* 1995, 52, (23), 16855-16863.
- [95] Hosemann, R. and Bagchi, S. N., *Direct analysis of diffraction by matter*. North-Holland: Amsterdam, 1962.
- [96] Pedersen, J. S., Determination of Size Distributions from Small-Angle Scattering Data for Systems with Effective Hard-Sphere Interactions. *Journal of Applied Crystallography* 1994, 27, 595-608.
- [97] Leroy, F., Lazzari, R. and Renaud, G., Effects of near-neighbor correlations on the diffuse scattering from a one-dimensional paracrystal. *Acta Crystallographica Section A* 2004, 60, 565-581.
- [98] Als-Nielsen, J. and McMorrow, D., *Elements of modern X-ray physics*. John Wiley & Sons Ltd. : West Sussex, England, 2001.
- [99] Bedzyk, M. J., *X-ray Standing Wave Techniques*. In *The Encyclopedic Dictionary of Condensed Matter Physics* Bassani, G. F., Liedl G. L., Wyder, P., Ed. Academic Press (Elsevier): 2005.
- [100] Bedzyk, M. J. and Cheng, L. W., X-ray standing wave studies of minerals and mineral surfaces: Principles and applications. *Applications of Synchrotron Radiation in Low-Temperature Geochemistry and Environmental Sciences* 2002, 49, 221-266.

[101] Alayan, R., Arnaud, L., Broyer, M., Cottancin, E., Lerme, J., Vialle, J. L. and Pellarin, M., Morphology and growth of metal clusters in the gas phase: A transition from spherical to ramified structures. *Physical Review B* 2006, 73, (12), 125444.

[102] Kasberger, U. and Jakob, P., Growth and thermal evolution of submonolayer Pt films on Ru(0001) studied by STM. *Surface Science* 2003, 540, (1), 76-88.

[103] Witten, T. A. and Sander, L. M., Diffusion-Limited Aggregation, a Kinetic Critical Phenomenon. *Physical Review Letters* 1981, 47, (19), 1400-1403.

[104] Ohring, M., *Materials science of thin films, deposition and structure*. 2 ed.; Academic Press: San Diego, California, 2002.

[105] Walko, D. A., Sakata, O., Lyman, P. F., Lee, T.-L., Tinkham, B. P., Okasinski, J. S., Zhang, Z. and Bedzyk, M. J., *Surface and interface studies at APS endstation 5ID-C*. In AIP Conference Proceedings 705, Warwick, T., Arthur, J., Padmore, H. A. and Stohr, J., Eds. American Institute of Physics: San Francisco, 2004; Vol. 705, pp 1166-1169.

[106] Revenant, C., Leroy, F., Lazzari, R., Renaud, G. and Henry, C. R., Quantitative analysis of grazing incidence small-angle x-ray scattering: Pd/MgO(001) growth. *Physical Review B* 2004, 69, (3), 035411.

[107] Lee, B., Park, I., Yoon, J., Park, S., Kim, J., Kim, K. W., Chang, T. and Ree, M., Structural analysis of block copolymer thin films with grazing incidence small-angle X-ray scattering. *Macromolecules* 2005, 38, (10), 4311-4323.

[108] Renaud, G., Lazzari, R., Revenant, C., Barbier, A., Noblet, M., Ulrich, O., Leroy, F., Jupille, J., Borensztein, Y., Henry, C. R., Deville, J. P., Scheurer, F., Mane-Mane, J. and Fruchart, O., Real-time monitoring of growing nanoparticles. *Science* 2003, 300, (5624), 1416-1419.

[109] Lee, B., Seifert, S., Riley, S. J., Tikhonov, G., Tomczyk, N. A., Vajda, S. and Winans, R. E., Anomalous grazing incidence small-angle x-ray scattering studies of platinum nanoparticles formed by cluster deposition. *Journal of Chemical Physics* 2005, 123, (7), 047701.

[110] Alayan, R., Arnaud, L., Bourgey, A., Broyer, M., Cottancin, E., Huntzinger, J. R., Lerme, J., Vialle, J. L., Pellarin, M. and Guiraud, G., Application of a static quadrupole deviator to the

deposition of size-selected cluster ions from a laser vaporization source. *Review of Scientific Instruments* 2004, 75, (7), 2461-2470.

[111] Melinon, P., Paillard, V., Dupuis, V., Perez, A., Jensen, P., Hoareau, A., Broyer, M., Vialle, J. L., Pellarin, M., Baguenard, B. and Lerme, J., From Free Clusters to Cluster-Assembled Materials. *International Journal of Modern Physics B* 1995, 9, (4-5), 339-397.

[112] Knauer, W., Formation of large metal clusters by surface nucleation. *Journal of Applied Physics* 1987, 62, (3), 841-851.

[113] Ritala, M., Advanced ALE processes of amorphous and polycrystalline films. *Applied Surface Science* 1997, 112, 223-230.

[114] Suntola, T., Atomic Layer Epitaxy. *Thin Solid Films* 1992, 216, (1), 84-89.

[115] Ott, A. W., Klaus, J. W., Johnson, J. M. and George, S. M., Al<sub>2</sub>O<sub>3</sub> thin film growth on Si(100) using binary reaction sequence chemistry. *Thin Solid Films* 1997, 292, (1-2), 135-144.

[116] Aaltonen, T., Ritala, M., Sajavaara, T., Keinonen, J. and Leskela, M., Atomic layer deposition of platinum thin films. *Chemistry of Materials* 2003, 15, (9), 1924-1928.

[117] Aaltonen, T., Ritala, M., Tung, Y. L., Chi, Y., Arstila, K., Meinander, K. and Leskela, M., Atomic layer deposition of noble metals: Exploration of the low limit of the deposition temperature. *Journal of Materials Research* 2004, 19, (11), 3353-3358.

[118] Zhu, Y., Dunn, K. A. and Kaloyeros, A. E., Properties of ultrathin platinum deposited by atomic layer deposition for nanoscale copper-metallization schemes. *Journal of Materials Research* 2007, 22, (5), 1292-1298.

[119] Elam, J. W., Zinovev, A., Han, C. Y., Wang, H. H., Welp, U., Hryn, J. N. and Pellin, M. J., Atomic layer deposition of palladium films on Al<sub>2</sub>O<sub>3</sub> surfaces. *Thin Solid Films* 2006, 515, (4), 1664-1673.

[120] Aaltonen, T., Rahtu, A., Ritala, M. and Leskela, M., Reaction mechanism studies on atomic layer deposition of ruthenium and platinum. *Electrochemical and Solid State Letters* 2003, 6, (9), C130-C133.

- [121] Elam, J. W., Zinovev, A. V., Pellin, M. J., Comstock, D. J. and Hersam, M. C., Nucleation and growth of noble metals on oxide surfaces using atomic layer deposition. *ECS Transactions* 2006, 3, (15), 271-278.
- [122] Elam, J. W., Groner, M. D. and George, S. M., Viscous flow reactor with quartz crystal microbalance for thin film growth by atomic layer deposition. *Review of Scientific Instruments* 2002, 73, (8), 2981-2987.
- [123] Beaucage, G., Approximations leading to a unified exponential power-law approach to small-angle scattering. *Journal of Applied Crystallography* 1995, 28, 717-728.
- [124] Beaucage, G., Small-angle scattering from polymeric mass fractals of arbitrary mass-fractal dimension. *Journal of Applied Crystallography* 1996, 29, 134-146.
- [125] Moulder, J. F., Stickle, W. F., Sobol, P. E. and Bomben, K. D., *Handbook of X-ray photoelectron spectroscopy*. Perkin-Elmer Corporation: Eden Prairie, Minnesota, 1992.
- [126] Nilsen, O., Karlsen, O. B., Kjekshus, A. and Fjellvag, H., Simulation of growth dynamics in atomic layer deposition. Part I. Amorphous films. *Thin Solid Films* 2007, 515, (11), 4527-4537.
- [127] Puurunen, R. L. and Vandervorst, W., Island growth as a growth mode in atomic layer deposition: A phenomenological model. *Journal of Applied Physics* 2004, 96, (12), 7686-7695.
- [128] Gjostein, N. A., *Surfaces and Interfaces*. In Burke, J. J., Reed, N. L. and Weiss, V., Eds. Syracuse University Press: Syracuse, New York, 1967.
- [129] Libera, J. A., Elam, J. W. and Pellin, M. J., Conformal ZnO coatings on high surface area silica gel using atomic layer deposition. *Thin Solid Films* 2008, 516, (18), 6158-6166.
- [130] Ravel, B. and Newville, M., Athena, Artemis, Hephaestus: data analysis for X-Ray absorption spectroscopy using Ifeffit. *Journal of Synchrotron Radiation* 2005, 12, 537-541.
- [131] Warren, B. E., *X-ray Diffraction*. Dover: New York, 1990.



[132] Moore, W. J. and Pauling, L., The crystal structures of the tetragonal monoxides of lead, tin, palladium, and platinum. *Journal of the American Chemical Society* 1941, 63, 1392 - 1394.

[133] Frelink, T., Visscher, W. and Vanveen, J. A. R., Particle-Size Effect of Carbon-Supported Platinum Catalysts for the Electrooxidation of Methanol. *Journal of Electroanalytical Chemistry* 1995, 382, (1-2), 65-72.

[134] Park, S., Xie, Y. and Weaver, M. J., Electrocatalytic pathways on carbon-supported platinum nanoparticles: Comparison of particle-size-dependent rates of methanol, formic acid, and formaldehyde electrooxidation. *Langmuir* 2002, 18, (15), 5792-5798.

[135] Parratt, L. G., Surface Studies of Solids by Total Reflection of X-rays. *Physical Review* 1954, 95, (2), 359-369.

[136] Nelson, A., Co-refinement of multiple-contrast neutron/X-ray reflectivity data using MOTOFIT. *Journal of Applied Crystallography* 2006, 39, 273-276.

## 9. Appendix A: Surface structures of SrTiO<sub>3</sub> (001) prepared during this project

**(1x1)** The (1x1) designates the bulk terminated surface for either the strontium-oxygen or titanium-oxygen chemical terminations. The (1x1) is the unreconstructed surface and was observed after etching with BHF and directly loading into a vacuum chamber equipped with LEED system. Figure A.1 is an example of the (1x1) LEED pattern and AFM image for a BHF treated SrTiO<sub>3</sub> sample. The faint atomic steps are visible after the etch in the image. The (1x1) has also been observed by first using the BHF solution and then annealing to 950°C in a tube furnace for 1 hour with flowing O<sub>2</sub>, Ar, or a H<sub>2</sub>(5%):N<sub>2</sub>(95%) mixture; the results of which are shown in Figure A.2. The morphology exhibited in Fig. A.2 maybe related to the annealing atmosphere but a systematic study of atmosphere, time, and temperature did not produce routine methods to achieve a particular morphology. The exception to this was oxygen annealing in that it consistently produced the cleanest and most defect-free atomic steps.

**(2x1)** The 2-domain (2x1) reconstruction, hereafter (2x1), is one of the most studied SrTiO<sub>3</sub> surface structures and was first observed by the Zegenhagen group using STM and LEED.<sup>27</sup> This paper showed a phase transition between the (1x1), (2x1), and (2x2) by heating in vacuum. A solution using transmission electron microscopy (TEM) to the (2x1) structure has been presented by Erdman *et al.*<sup>26</sup> The result is a structure where the last two layers of the surface consist of two titanium ion sites surrounded by oxygen ions. The preparation of this surface involved first the BHF treatment followed by Ar<sup>+</sup> bombardment as part of the TEM sample thinning preparation. The thin sample was then annealed in oxygen at 1000°C for several hours to ‘heal’ the ion bombardment damage.

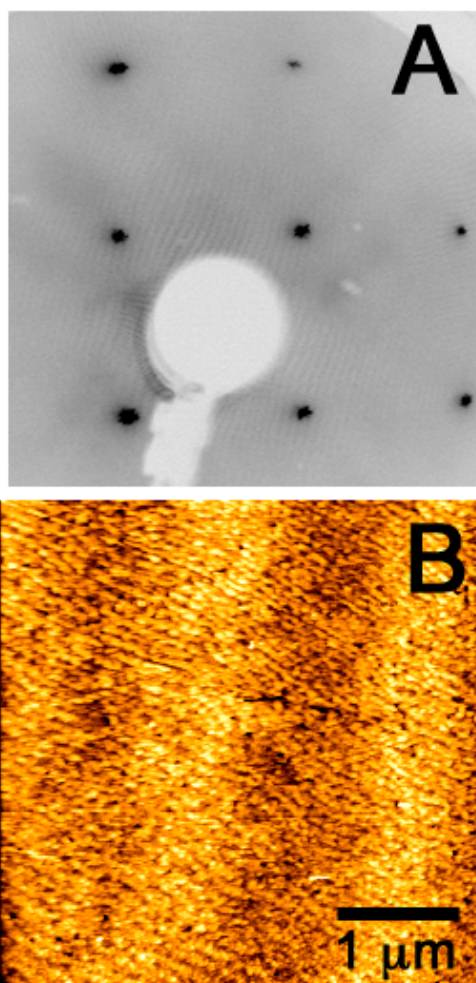


**Figure A.1** A) LEED pattern and B) AFM for BHF etched SrTiO<sub>3</sub>. The LEED pattern is the (1x1) bulk-terminated SrTiO<sub>3</sub> and the AFM shows faint atomic steps. LEED collected at NU using the Bedzyk UHV system.

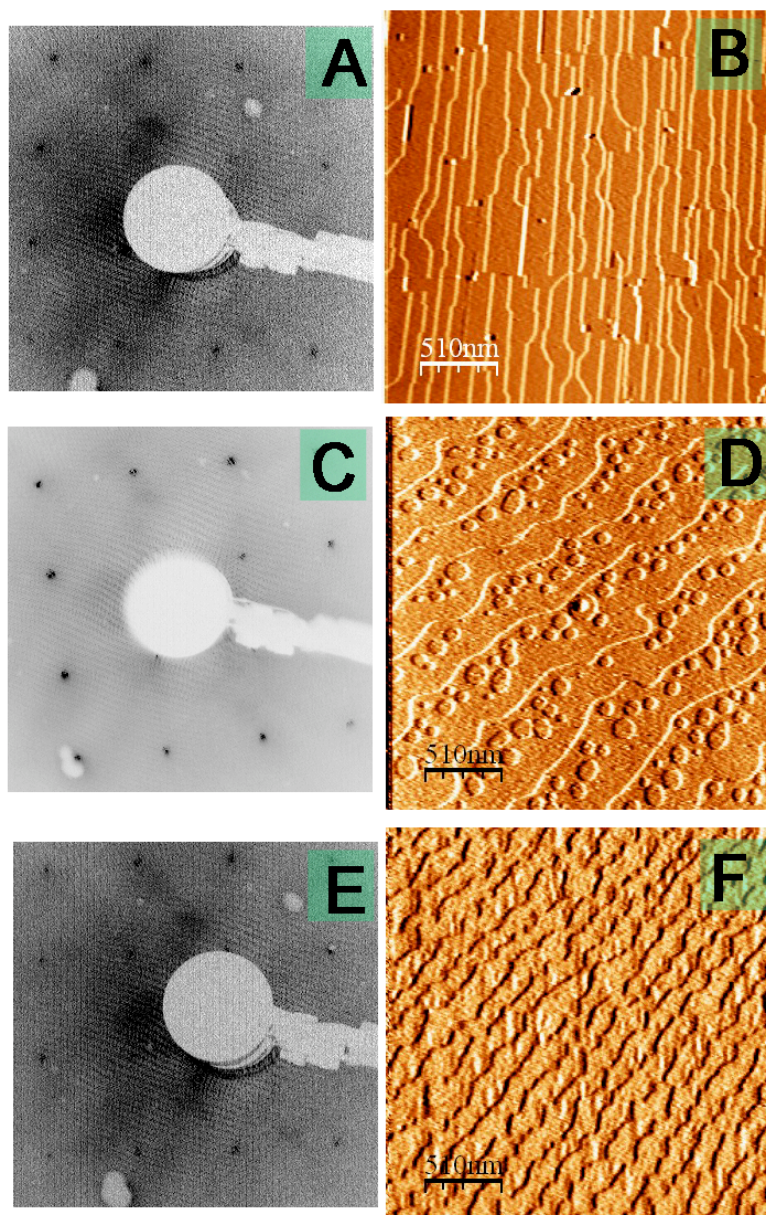


**Figure A.2** LEED and AFM images of SrTiO<sub>3</sub> (001) after various surface preparations. All the samples show the (1x1) bulk LEED pattern and atomic steps and were first etched with buffered hydrofluoric acid. The one hour annealing treatment included: A) and B) flowing oxygen at 950 - 1050°C; C and D) flowing H<sub>2</sub>/N<sub>2</sub> (5%:95%) at 900°C; E and F: argon at 900°C. The surface morphology of these structures was systematically studied as a function of the annealing gas and temperature. There was no success at reproducing the observed morphology consistently. In general, oxygen annealing produced the cleanest atomic step structure with minimal defects. LEED pattern beam energies A) 154 eV; C) 163 eV; E) 165 eV.

The preparation approach conducted within this project was more consistent with the literature.<sup>27-29, 31</sup> This is due to numerous attempts to employ an oxygen anneal in the preparation based on results from Erdman *et al.* and a former Bedzyk group member, Alexander Kazimirov, who incidentally worked in the Zegenhagen group. The Kazimriov method was able to get brilliant (2x1) LEED patterns after the BHF etch, oxygen anneal, and then ultra-high vacuum (UHV) annealing to > 900°C. After several attempts to reproduce this result, a successful (2x1) LEED pattern was produced after etching with BHF and then annealing to 930°C for 1 h in UHV. This is very similar to the method used by the Zegenhagen group<sup>27</sup> and does not require any oxygen annealing. This (2x1) reconstruction was produced routinely during the course of this project and an example of the LEED pattern is given in Figure A.3 (a). Since diffraction patterns do not necessarily constitute a unique structure the differences between recipes for the (2x1) may be due to two different structures. Another possibility lies in differences between the vacuum chamber, temperature calibration, and other experimental parameters that may have been overlooked.

**( $\sqrt{13}\times\sqrt{13}$ )R33.7°** The most common surface reconstruction observed during this project is the ( $\sqrt{13}\times\sqrt{13}$ )R33.7°. This was a byproduct of the efforts to prepare the (2x1) using an oxygen annealing step. The reconstruction is prepared by first etching with the BHF solution followed by annealing in flowing oxygen at 900-1050°C for five to twelve hours. For example, Figure A.3 (b) shows the LEED pattern after annealing at 900°C for 11 h, but similar results were obtained by annealing for 5 h at 1050°C. This is compared to that reported in the literature where the ( $\sqrt{13}\times\sqrt{13}$ )R33.7° was observed using reflection high energy electron diffraction (RHEED) after annealing in oxygen for 2 hours at 800°C.<sup>31</sup>

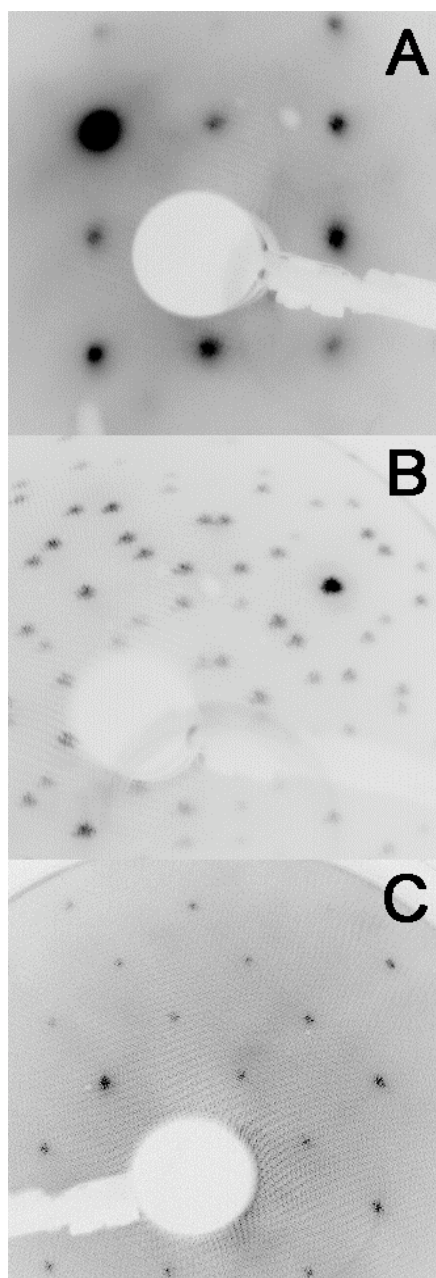
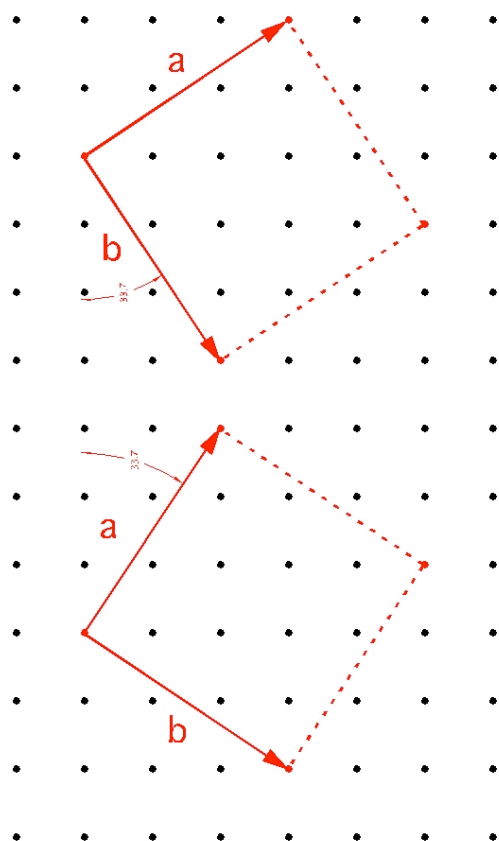


**Figure A.3** LEED patterns for different SrTiO<sub>3</sub> reconstructions: A) (2x1) – two domain; B)  $(\sqrt{13}\times\sqrt{13})R33.7^\circ$ ; C)  $(\sqrt{2}\times\sqrt{2})R45^\circ$ . The (2x1) was obtained using the BHF etch and annealing in UHV for 1 h at 930°. The  $(\sqrt{13}\times\sqrt{13})R33.7^\circ$  was produced after first etching and then annealing in flowing oxygen for 5-12 h with a temperature range of 900-1050°C. This pattern was also produced on a pre-thinned TEM sample. The  $(\sqrt{2}\times\sqrt{2})R45^\circ$  was observed after first producing the  $(\sqrt{13}\times\sqrt{13})R33.7^\circ$  and then annealing to 1000°C for 1 h in UHV. LEED pattern beam energies: A) 51.2 eV; B) 46.7eV; C) 134 eV.

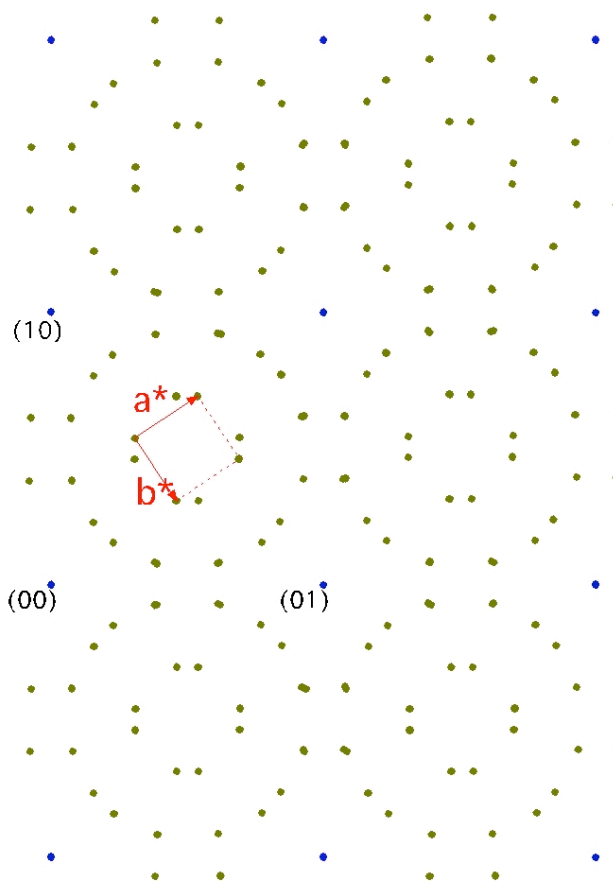
The structure was tested for stability during this project by iteratively collecting the LEED pattern after exposing to air. The LEED pattern persisted for a little over an hour of total exposure time. This pattern was also obtained and observed with TEM in collaboration with the Marks group. Pre-thinned TEM samples were etched and annealed in the same manner as above and then subsequently transferred to the TEM for imaging. No reports have been published with a solution to this particular structure. This reconstruction was selected for platinum nanoparticle studies because of the clean terraces and the relative ease to produce it with etching and annealing in a tube furnace. A diagram of the real space and k-space  $(\sqrt{13}\times\sqrt{13})R33.7^\circ$  structure is given in Figure A.4.

$(\sqrt{2}\times\sqrt{2})R45^\circ$  This project produced one other distinct LEED pattern indicating a different reconstruction. By annealing in a UHV environment a sample that first showed the  $(\sqrt{13}\times\sqrt{13})R33.7^\circ$  (after oxygen annealing) the LEED pattern was observed to change to a  $(\sqrt{2}\times\sqrt{2})R45^\circ$  as shown in Figure A.3 (c). The UHV annealing was measured with an optical pyrometer to be  $1000^\circ\text{C}$  and lasted for an hour.

Real - space  $(\sqrt{13}\times\sqrt{13})R33.7^\circ$



$k$  - space



$$\mathbf{a}^* = \frac{\mathbf{b} \times \mathbf{n}}{\mathbf{a} \cdot (\mathbf{b} \times \mathbf{n})}, \quad \mathbf{b}^* = \frac{\mathbf{n} \times \mathbf{a}}{\mathbf{b} \cdot (\mathbf{n} \times \mathbf{a})}$$

**Figure A.4** Diagram of the real space and  $k$ -space  $(\sqrt{13}\times\sqrt{13})R33.7^\circ$  structure with the definition of the reciprocal lattice vectors  $\mathbf{a}^*$  and  $\mathbf{b}^*$  in terms of the lattice vectors  $(\mathbf{a}, \mathbf{b})$  and surface normal,  $\mathbf{n}$ .



## 10. Appendix B: X-ray standing wave atomic density maps

This section describes origin of the platinum atomic density maps shown in Figure 2.5. The data stems from the work of A. Kazimirov, a former Bedzyk group member who started Pt / SrTiO<sub>3</sub> (001) project. The following will highlight key issues regarding the sample preparation, measurement and the atomic density maps.

The substrates were procured from OKEN, a Japanese firm, who grew them with the float zone method as opposed to the Verneuil method discussed in Chapter 2. It was later learned that OKEN is the only manufacturer to use the float zone method which is known in the industry to produce the highest quality SrTiO<sub>3</sub> substrates. OKEN discontinued supply of float zone SrTiO<sub>3</sub> to other vendors for cutting and resale.

The sample preparation occurred at 12ID-D of the APS with the Bedzyk group UHV chamber interfaced with the beam line. Based on the logbooks and reports, the sample preparation involved a BHF etch and 5 hour anneal in an oxygen furnace at 1050°C. Following this, the samples were annealed in UHV for 30 minute installments at 950°C until the two-domain (2x1) reconstruction appeared. Usually, one 30 minute installment was sufficient. Platinum deposition followed via *e*-beam evaporation (Omicron) while the sample was held at 400°C. The samples were then annealed for 30 minutes at ~500°C prior to XSW measurements. This process was repeated until a coherent fraction was measured. The samples were annealed further in between XSW measurements. Of 25 – 30 samples prepared only four seemed to have a coherent fraction and only two of these showed a stable coherent fraction when brought out into air. The stability in air was exceptional as the XSW measurements in air were collected several months after they were prepared. No mention of where the samples were stored between

the XSW measurements.

Details of XSW analysis are reviewed elsewhere.<sup>99, 100</sup> The atomic density maps are generated by summing the measured Fourier components extracted from the XSW fitting. These components are termed the coherent fraction ( $f_H$ ) and coherent position ( $P_H$ ) for the Bragg reflection  $H$ . The  $f_H$  and  $P_H$  give are respectively the Fourier amplitude and phase. The atomic density is given by<sup>99</sup>:

$$\rho(\mathbf{r}) = \sum_H f_H \exp[i(2\pi P_H - \mathbf{H} \cdot \mathbf{r})]. \quad (\text{B.1})$$

The atomic density maps shown in Figure 2.5 were plotted using the Matlab routines. Examples of the Matlab code has been given in dissertation work of Bedzyk group members (Zhang, Escudro, Okasinski). Tables B.1 and B.2 give the coherent positions and coherent fractions used to make the Figure 2.5 images.

<b>Table B.1: STO 012, 0.60 ML Pt / SrTiO<sub>3</sub> (001)</b>		
<i>hkl</i>	$f_H$	$P_H$
001	0.07	0.07
002	0.39	-0.18
011	0.07	0.07
022	0.22	0.84
111	0.35	-0.13
222	0.15	-0.08

<b>Table B.2: STO 013, 0.17 ML Pt / SrTiO<sub>3</sub> (001)</b>		
<i>hkl</i>	$f_H$	$P_H$
001	0.21	0.68
002	0.26	0.93
022	0.11	0.15
111	0.26	0.61

**Tables B.1 and B.2** Coherent fraction and positions for the XSW results of Alexander Kazimirov.

## 11. Appendix C: X-ray reflectivity at low angles

This project included several X-ray reflectivity (XRR) studies that were ultimately not included in main body of the dissertation. Explanation of X-ray reflectivity for various structures is given in detail elsewhere.<sup>92, 98, 135</sup> The discussion for the reflectivity of a platinum film on a SrTiO<sub>3</sub> substrate herein is restricted to the kinematical approximation. The XRR is related to the Fourier transform of the electron density of the film and substrate and is given by<sup>98</sup>:

$$R(q) = R_F(q) \left| \int_0^{\infty} \frac{d\rho_e}{dz} \exp(iqz) dz \right|^2 \quad (\text{C.1})$$

where  $\rho_e(z)$  gives the electron density profile of the material along the  $z$ -direction, which is normal to the surface and  $R_F(q)$  is the Fresnel reflectivity of the substrate. The Fresnel reflectivity is also discussed in Ref. [98]. To a first approximation, the electron density profile and its derivative with respect to  $z$  for a Pt film of thickness  $t$  on a SrTiO<sub>3</sub> slab are given by the following equations:

$$\rho_e(z) = \begin{cases} 0, & z < 0 \\ b, & 0 < z \leq t \\ 1, & z > t \end{cases} \quad (\text{C.2})$$

$$\rho'_e(z) = b\delta(z) + (b-1)\delta(z-t) \quad (\text{C.3})$$

where  $b$  is the average electron density of the film normalized to the substrate electron density and  $\delta(z)$  is a delta function. For real samples interface roughness creates a diffuse interface, which can be approximated by a Gaussian function:

$$g(z) = \frac{1}{\sigma\sqrt{2\pi}} \exp\left[-\frac{(z-z_0)^2}{\sigma^2}\right] \quad (\text{C.4})$$

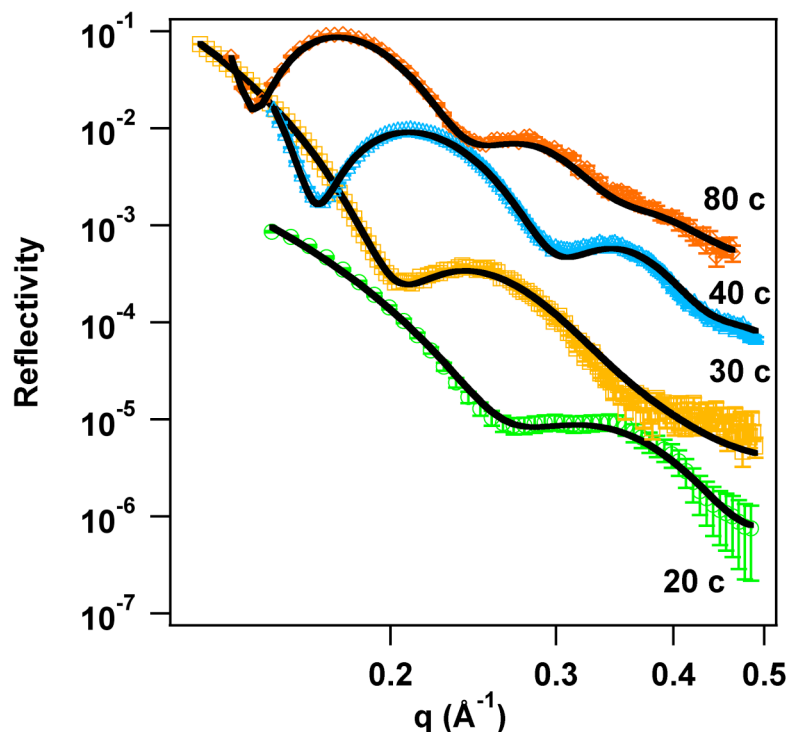
where  $\sigma$  gives the interface roughness. Replacing the delta functions in eq C.3 with eq C.4 and taking into account the possibility of two different interface roughness values, the derivative of the electron density profile becomes:

$$\rho'_e(z) = \frac{b}{\sigma_a \sqrt{2\pi}} \exp\left[-\frac{z^2}{\sigma_a^2}\right] + \frac{(b-1)}{\sigma_b \sqrt{2\pi}} \exp\left[-\frac{(z-t)^2}{\sigma_b^2}\right] \quad (\text{C.5})$$

The reflectivity may then be calculated by inserting eq C.5 into eq C.1 and simplifying with Euler's formula to give:

$$R(q) = R_F(q) \left[ b^2 e^{-(q\sigma_a)^2} + (b-1)^2 e^{-(q\sigma_b)^2} - 2b(b-1) \cos(qt) e^{-\frac{1}{2}q^2(\sigma_a + \sigma_b)^2} \right] \quad (\text{C.6})$$

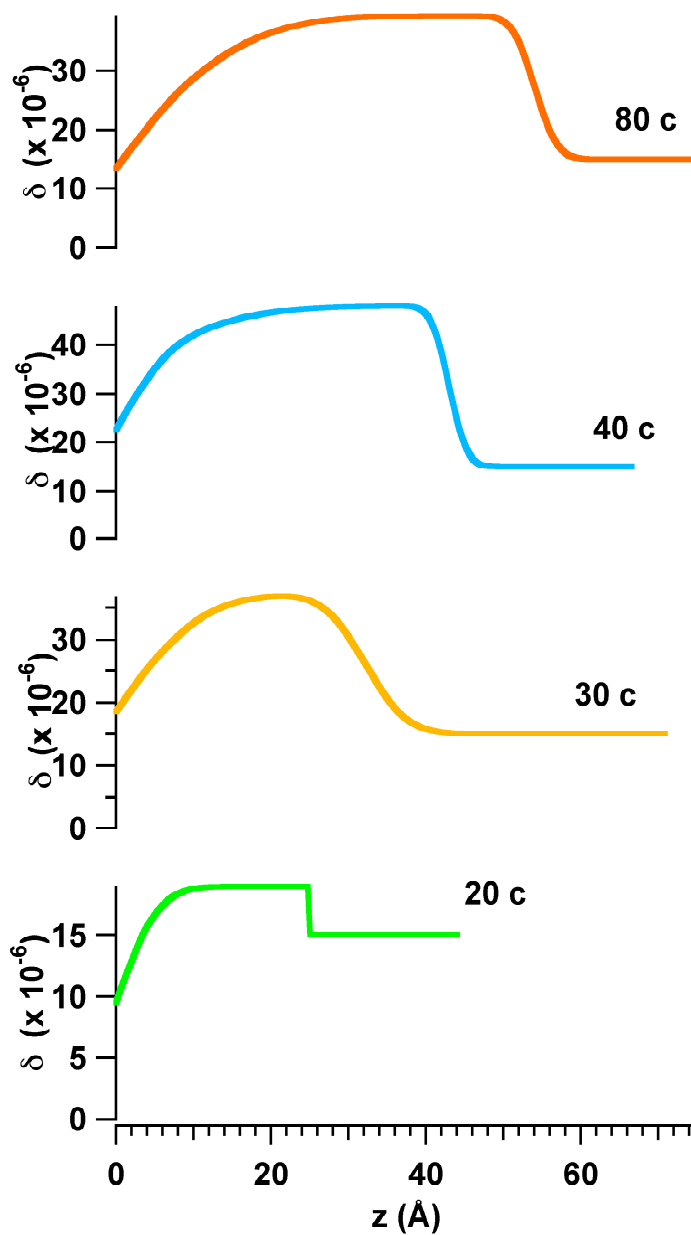
Figure C.1 shows the measured XRR and fits based on eq C.6 using the MOTOFIT Igor plugin<sup>136</sup> for a series of ALD Pt/SrTiO<sub>3</sub> (001) cases. The electron density profiles are given in Figure C.2 with the fitting results given in Table C.1. Table C.1 includes the following fitted parameters: film thickness ( $t$ ), the interface roughness ( $\sigma$ ), and the electron density of the Pt film ( $b$ ), which has been converted to the percent ideal platinum density ( $\rho = 66.3$  Pt atoms /nm<sup>3</sup>). The platinum coverage ( $\Theta$ ) is calculated from the XRR fitting results by:  $\Theta_{\text{XRR}} = f t * \rho$  where  $f$  is the fraction density related to the %  $\rho$  from the table. The platinum coverage measured directly by X-ray fluorescence is given by  $\Theta_{\text{XRF}}$ . The calculated coverage data show good agreement with the XRF measurements and indicate that the growth rate slows at 80 cycles. The change in growth rate is the focus of Chapter 5.



**Figure C.1** X-ray reflectivity for ALD Pt films following deposition. Offset for clarity: 20 cycles, no offset; 30 cycles, offset = 0.013; 40 cycles, offset = 0.015; 80 cycles, offset = 0.0315. Data collected at NU X-ray facility (Rigaku ATXG).

ALD cycles	20	30	40	80
$t$ (nm)	$2.3 \pm 0.2$	$3.2 \pm 0.1$	$4.3 \pm 0.1$	$5.4 \pm 0.2$
$\sigma_{\text{Pt}}$ (nm)	0.7	1	0.8	1
$\sigma_{\text{Pt/STO}}$ (nm)	$\sim 0$	0.4	0.3	0.3
% $\rho$	$56 \pm 19$	$79 \pm 11$	$85 \pm 4$	$79 \pm 9$
$\Theta_{\text{XRR}}$ ( $\times 10^{14} \text{ cm}^{-2}$ )	$87 \pm 36$	$170 \pm 25$	$240 \pm 12$	$279 \pm 35$
$\Theta_{\text{XRF}}$ ( $\times 10^{14} \text{ cm}^{-2}$ )	$74 \pm 1$	$165 \pm 3$	$234 \pm 5$	$262 \pm 5$

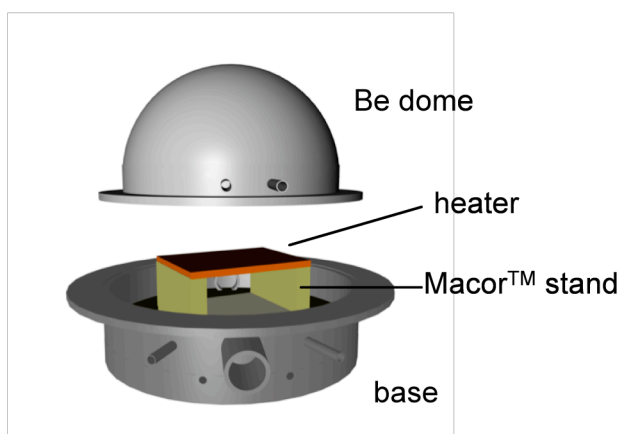
**Table C.1** XRR fitting results for data from Fig. C.1. Fitted parameters include the film thickness( $t$ ), interface roughness ( $\sigma$ ), and film density compared to ideal platinum density, %  $\rho$ . Also included is measured (XRF) and calculated (XRR) platinum coverage.



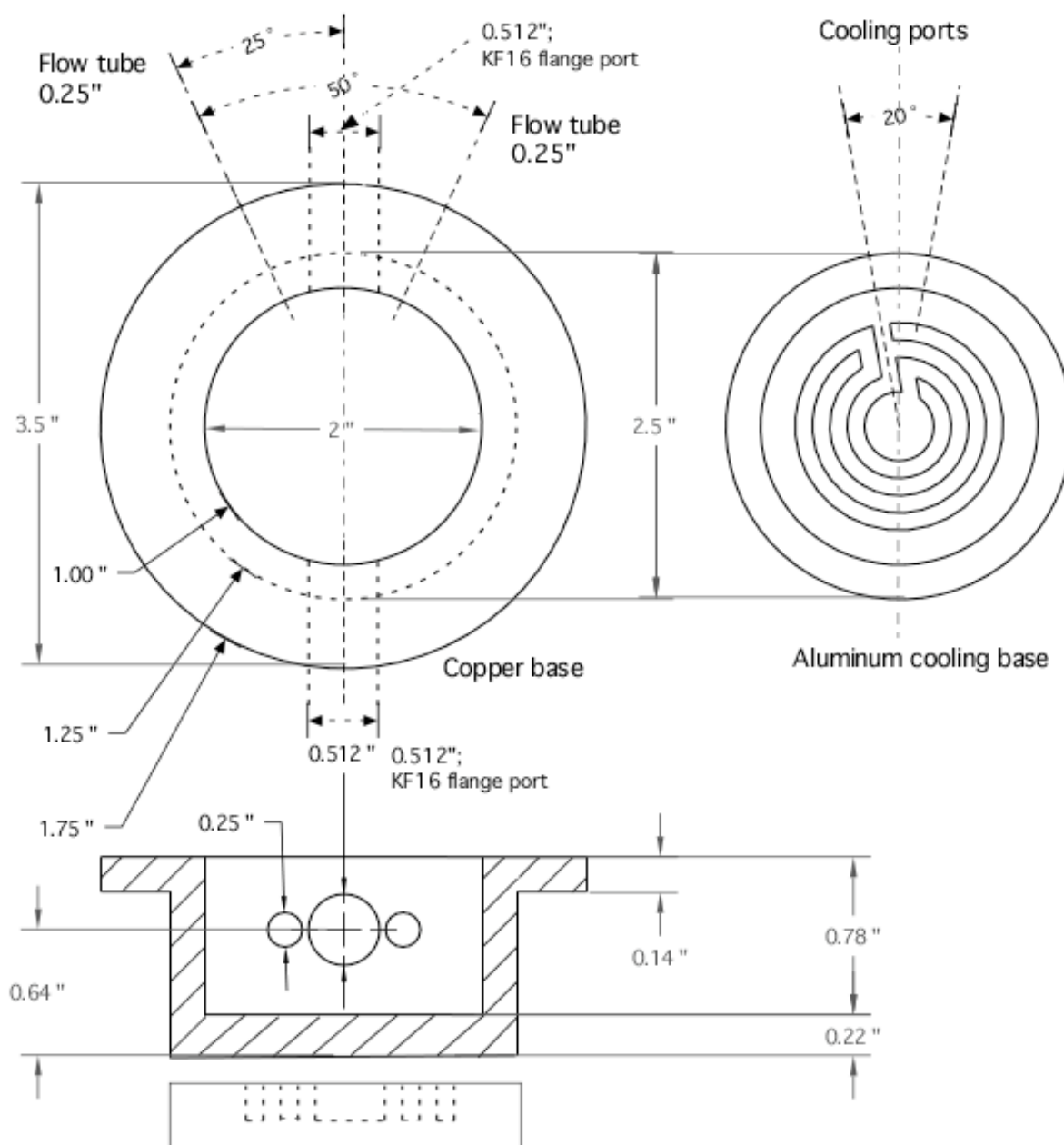
**Figure C.2** ALD Pt/SrTiO<sub>3</sub> density profiles from the fits in Fig. C.1. The profiles are in terms of the index of refraction component  $\delta$  and include the film thickness and interface roughness.

## 12. Appendix D: Plans of the X-ray reaction cell base

This appendix describes the construction of a reaction cell designed to facilitate *in situ* X-ray measurements. The construction consists of building a base for an already existing beryllium dome. Figure D.1 is a conceptual drawing of the device. The base incorporates a sample holder that can heat the sample under gas flow or vacuum. The sample heater is a pyrolytic boron nitride heater (Momentive Performance Materials Quartz, Strongsville, Ohio, part no HTR1001). The design features two KF16 vacuum ports to provide electrical and thermocouple access. Two 0.25" tubes provide flow access using compression fittings. The heater sits on a machinable ceramic stand (Macor, Corning Inc.), which is thermally insulating. The base can also accommodate water cooling. Figures D.2 and D.3 are schematic drawings of the base and Macor stand. The base can also accommodate sample cooling with some modifications. The base is stable enough to enable XSW measurements to be conducted simultaneously with sample heating and gas flow.



**Figure D.1** Conceptual drawing of the Be dome and reaction cell base.

Be Dome Base

**Figure D.2** Schematic drawing of the Be dome base.



### MACOR Heater Stand

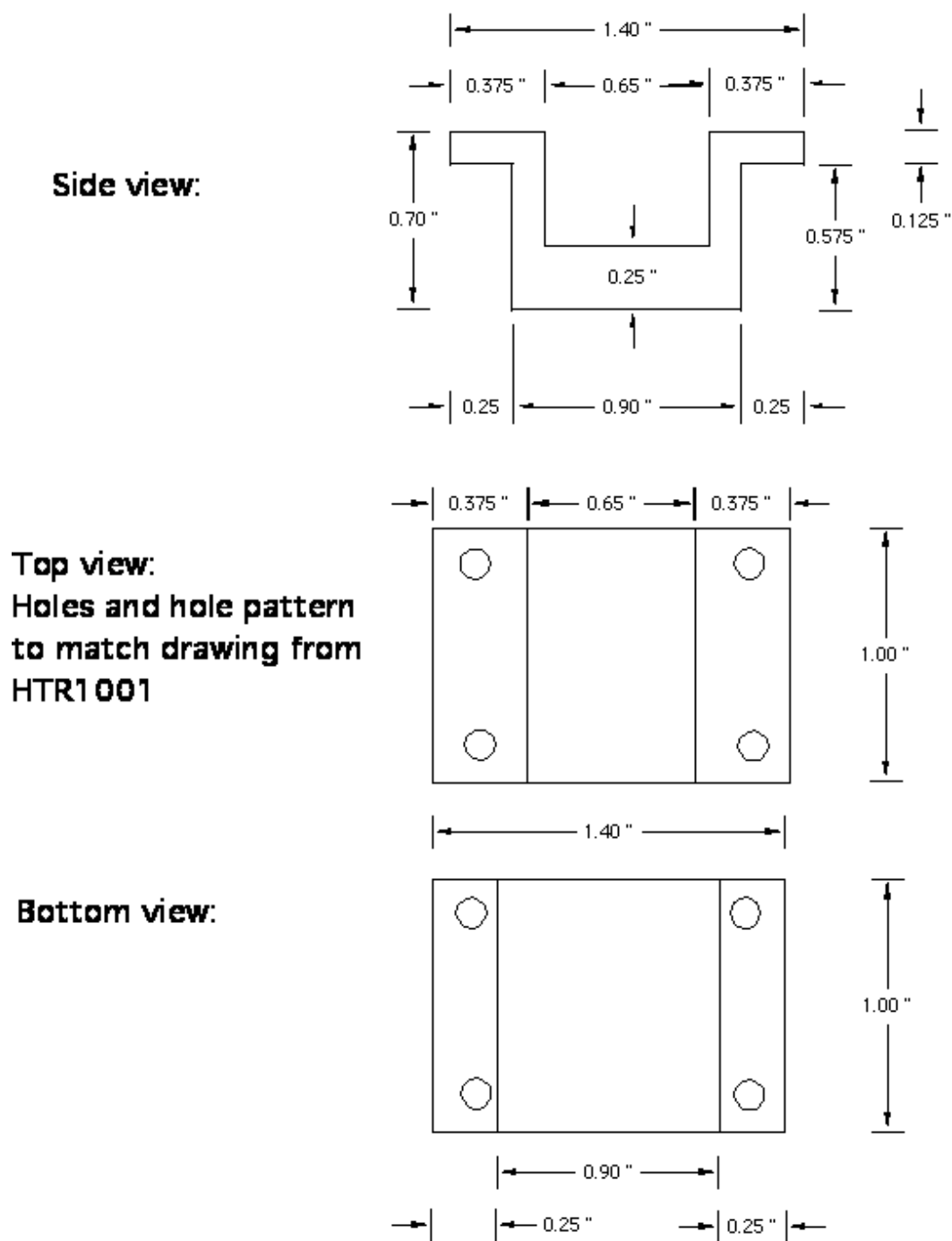


**Figure D.3** Schematic drawing of the machinable ceramic base.

### 13. Appendix E: Experimental Facilities

Herein are listed additional information on the experimental facilities that were used for preparing and characterizing the Pt/SrTiO<sub>3</sub> (001) samples studied within this dissertation.

In the Bedzyk Research Lab at NU the Lindberg/Blue tube furnace was used for oxygen annealing the substrates. The tube furnace entailed a fused quartz tube with fused quartz end caps (Quartz Scientific). The samples were held in fused quartz boats made by the NU glass shop (Wilmad Lab Glass). Gas flow originated from gas cylinders with a standard regulators and a custom flow meter (Matheson Trigas). Gas flow was set to a nominal flow of ~100 sccm for air. The Bedzyk UHV MBE surface science chamber [W.P. Rodrigues PhD Dissertation NU 2000] was used to prepare the reconstructed SrTiO<sub>3</sub>(001) surfaces, deposit Pt on the surface with a Omicron triple *e*-beam evaporator, and characterize the surfaces with an Omicron Spectra-LEED system and Physical Electronics Auger single-pass cylindrical mirror analyzer.

The work conducted in the Hersam group facilities primarily involved the use of the CP Research AFM (Thermomicroscopes – now Veeco). There were two of these instruments with the bulk of the work being done with the instrument in Cook Hall 1119a serial No. CP0565. The other AFM in Cook Hall 1117 serial No. is CP0508. Samples were mounted on bare steel tabs with no tape.

Several instruments were used in the X-ray Diffraction facility at NU. However, for the data presented in this dissertation the primary instruments include the Blake Industries 5-bounce high-resolution diffractometer (Fig. 2.2); the Bedzyk group Rigaku 2-circle 18 kW that was outfitted with a Zr coated rotating anode for fluorescence measurements (Fig. 5.6); the Rigaku

ATXG produced the reflectivity data in Appendix C.

Wet chemical treatment of the single crystal substrates was performed in both the Bedzyk and Hersam groups. Glassware was standard for deionized water and organic solvent sonication with samples being held in a custom-made Teflon dip basket (NU machine shop). For BHF etching, custom Teflon beakers (NU machine shop) were used to hold the HF solution and the custom made dip basket was also used. Ultra-sonic instruments included a Cole-Palmer 8891 (Bedzyk group) and a Brinson 3150 (Hersam group). Deionized water was obtained from a Millipore Synergy 185 (Bedzyk group) and a Barnstead NANOpure Diamond (Hersam group), which both produced water with 18 M $\Omega$ -cm resistivity.

A total of five personal laboratory notebooks and two group notebooks were used to record the work performed during this dissertation. The notebooks include two for general use as well as most of the work done in the Hersam group. All AFM data and tube furnace annealing data are recorded in these two notebooks. The other three notebooks contain the work related to X-ray studies both at the APS and NU. These notebooks also contain all the XSW work on Pt/SrTiO<sub>3</sub>. The preparation of the samples in Chapter 4 with the Bedzyk group UHV chamber was recorded in two Bedzyk group logbooks that accompany the vacuum chamber.

## 14. VITA

Steven Thomas Christensen

Place of Birth: Ogden, Utah, USA

### Education

B.S., Materials Science and Engineering, University of Utah, Salt Lake City, Utah, 2003

Ph.D., Materials Science and Engineering, Northwestern University, Evanston, Illinois, 2008

### Experience

(09/2003 – present) Department of Materials Science and Engineering, Northwestern University, Evanston, Illinois, *Graduate Research Assistant*

(06/2003 – 01/2001) Department of Materials Science and Engineering, University of Utah, Salt Lake City, Utah, *Lab Technician*

(12/2000 – 10/2000) EDO Corporation, Ceramics Division, Salt Lake City, Utah, *Quality Control Technician*

### Publications

“Structure and morphology of platinum nanoparticles deposited via atomic layer deposition on strontium titanate nanocubes”, Steven T. Christensen, Jeffrey W. Elam, Federico A. Rabuffetti, Qing Ma, Steven Weigand, Peter C. Stair, Kenneth R. Poeppelmeier, Byeongdu Lee, Soenke Seifert, Mark C. Hersam, Michael J. Bedzyk, in preparation.

“Nanoscale structure and morphology of atomic layer deposition platinum on SrTiO<sub>3</sub> (001)”, S.T. Christensen, J.W. Elam, B. Lee, Z. Feng, M.J. Bedzyk, M. C. Hersam, *Chemistry of Materials*, accepted December 2008.

“Platinum nanoparticle clustering on SrTiO<sub>3</sub> (001): A combined atomic force microscopy and grazing-incidence small-angle X-ray scattering study”, Steven T. Christensen, Byeongdu Lee, Zhenxing Feng, Mark C. Hersam, Michael J. Bedzyk, Submitted.

“Imaging of atomic layer deposited (ALD) tungsten monolayers on  $\alpha$ -TiO<sub>2</sub> (110) by X-ray standing wave Fourier inversion”, Kim, C.-Y., Elam, J. W., Pellin, M. J.; Goswami, D. K., Christensen, S. T., et al., *Journal of Physical Chemistry B* **110** (2006) 12616.

“Controlled nanoscale morphology of hematite (0001) surfaces grown by chemical vapor transport”, M. E. Greene, A. N. Chiamonti, S. T. Christensen, et al., *Advanced Materials* **17**,1765 (2005).

“Production of fine Nd-Fe-B powder by pulsed plasma atomization”, J. E. Shield, S. Christensen, R. W. Kincaid, et al., *Journal of Materials Science* **38**, 445 (2003).